MONASH University

Elastohydrodynamic Origins of Flagellar Beat Transitions in Sperm

Shibani Veeraragavan

A thesis submitted for the degree of Doctor of Philosophy
at Monash University

2023

Department of Mechanical and Aerospace Engineering

Copyright Notice

Abstract

Sperm propel themselves by beating their flagella, exhibiting complex beating patterns that are driven internally by the axoneme. These beating patterns are also affected by environmental factors, such as external fluid viscosity and the presence of walls. The current view is that such changes in the beating patterns would involve internal regulation of the axoneme. This study explores the alternative possibility that beat pattern changes emerge as a result of the fluid-structure interaction between the elastic flagellum and the external fluid flow driven by the motion of the flagellum. Sperm are modelled as Internally-driven Kirchhoff Rods (IDKRs), with the internal driving consisting of a predetermined travelling wave of active bending moments. Simulations are used to track the emergent three-dimensional motion of the IDKR in fluids of different viscosities as well as near a wall, while the internal driving is kept unchanged. Comparisons of the simulation results with experimental data obtained from literature as well as in-house experiments[1] suggest, for the first time, that the beat pattern changes exhibited by sperm in different hydrodynamic environments may have elastohydrodynamic origins, and can be achieved without any regulation of the internal driving. The results presented in this study also suggest the first elastohydrodynamic mechanism behind the emergence of planar as well as experimentally-relevant three-dimensional beat patterns from the same internal driving, without any imposed asymmetry in the structure of the filament or the internal driving. Using a linear stability analysis, it is shown that the the emergence of planar and three-dimensional beating in the simulations is governed by an elastohydrodynamic instability. This work also demonstrates that long-range hydrodynamic interactions can create qualitative differences in flagellar beat patterns, especially near a wall. Since many studies in the field currently use local drag theories that neglect long-range hydrodynamic interactions, this finding is expected to inform future studies that probe emergent flagellar waveforms. In the final part of this work, a new model for shearable flagella is suggested which will enable future studies to explore the beat transitions exhibited by flagella with mechanically-regulated axonemes.

[1] Experimental data was provided by F. Yazdan Parast and R. Nosrati (Dept. of Mechanical and Aerospace Engineering, Monash University).

Declaration

This thesis is an original work of my research and contains no material which has been accepted for the award of any other degree or diploma at any university or equivalent institution and that, to the best of my knowledge and belief, this thesis contains no material previously published or written by another person, except where due reference is made in the text of the thesis.

Signature:

Print Name: Shibani Veeraragavan

Date: 12 February 2023

Publications from this Work

Veeraragavan, S. and Prabhakar, R. (2020). Is Hydrodynamic Interaction Important in Beating Patterns in Internally-driven Microfilaments?. In *Proceedings of the 22nd Australasian Fluid Mechanics Conference AFMC2020*, Brisbane, Australia. The University of Queensland. https://doi.org/10.14264/441d6b9.

Acknowledgements

The effort and support of many people helped bring this thesis to life. First and foremost, I thank my supervisor Dr Prabhakar Ranganthan for being my *guru* for the past three and a half years – he guided my learning and helped me grow as a researcher while also supporting my overall wellbeing throughout my time here. This project went on under very unusual circumstances – in the midst of a pandemic and the associated lock-downs which kept me working in isolation for the majority of the project duration. Dr Prabhakar and my co-supervisor Dr Reza Nosrati made every effort to support me during this time, and I'm extremely grateful for their guidance and encouragement. Dr Reza played a major role in pulling me out of the isolation and helping me re-connect with my peers. I was fortunate to have had the chance to work closely with another of his students, Farin Yazdan Parast, to gain some much-needed experimental insight. Conversations with Farin and trips to the lab added perspective to this work and gave me new ideas. I thank my PhD milestone panel members Prof. Greg Sheard and Dr Douglas Brumley for their timely feedback. I also thank Dr Ashwin Nandagiri, a previous member of Dr Prabhakar's group, for his initial guidance on the experimental image analysis program.

This project was funded partially by the Australian Government via the Australian Research Council's Discovery Projects funding scheme (project DP190100343), and partially by the Monash University Faculty of Engineering International Postgraduate Research Scholarship (FEIPRS). I'm grateful for the resources, training and support provided by Monash University; this includes the computational infrastructure MonARCH which was crucial for the simulations in this study. The Monash High-Performance Computing (HPC) team provided valuable assistance and training. I would also like to thank Dr Lilian Khaw from the Graduate Research Academic Support (GRAS) team for her invaluable assistance with proofreading parts of the thesis.

I'm incredibly grateful to my friends and family for their wishes and support. My family played a major role in shaping my decision to pursue a PhD in STEM – my parents and my aunt Sudha were the first academics I knew. Through my parents, the love for science and engineering seeped into me at a very young age, and served to motivate me throughout this journey. I would also like to thank my lecturer during undergraduate studies, Dr Ho Yong Kuen (Joseph) at Monash University Malaysia, for encouraging me to aim higher. He believed in me more than I believed in myself, and his words shaped my decision to undertake this project. My friends at Monash University – Gargi, Sneha, Somnath and Joe – helped me 'settle in' during my first year. I'm thankful for our casual conversations over coffee, which helped me understand the ups and downs of a PhD. I am indebted to Divyansh for being present by my side even at times when no one else could be – his constant support helped me complete this work in a timely manner.

Finally, I wish to acknowledge the people of the Kulin Nation, the Traditional Owners of the land on which I've lived and worked for the past few years. I pay my respects to their Elders, past, present and emerging, and thank them for caring for this land and its ecosystems since time immemorial.

Contents

Abstract 5

1 Introduction 25

2 Background and Literature Survey 31

2.1 Swimming at low Reynolds number 32

2.2 Modelling Flagellar Hydrodynamics 34

2.3 Modelling Internal Stresses 37

2.4 Modelling Active Stresses 39

2.5 The Importance of Beat Transitions 41

2.6 Aims 42

3 Methods 45

3.1 Modelling the Flagellum as an Internally-driven Kirchhoff Rod 45

3.2 Dimensionless Quantities and Boundary Conditions 55

3.3 Numerical Method 56

3.4 Analysing Flagellar Waveforms 60

4 Effect of Fluid Viscosity on Beat Patterns in Bulk Fluid 65

4.1 Introduction 65

4.2 Emergent Planar Waveforms 66

4.3 Emergent Three-dimensional Waveforms 69

4.4 The Parameter Map explains Viscosity-related Beat Transitions 73

4.5 Chapter Summary 75

5 Exploring the Origins of Non-planar Beating Patterns 77

5.1 Introduction 77

5.2 Role of Long-range Hydrodynamic Interactions 78

5.3 Linear Stability of Planar Beating 80

5.4 Chapter Summary 85

6 Experimental Observations of Bull Sperm in Media of Different Viscosities 87

6.1 Introduction 87

6.2 Sperm Sample Preparation, Imaging and Waveform Extraction 88

6.3 Analyses of Beat Patterns at Different Viscosities 90

6.4 An Explanation for Differences between Species and within Species 92

6.5 Chapter Summary 94

7 Effect of a Plane Wall on Beat Patterns 97

7.1 Introduction 97

7.2 Effect of a Wall on Planar Beat Patterns 99

7.3 Effect of a Wall on Three-dimensional Beat Patterns 103

7.4 Limitations of the Hydrodynamic Model 105

7.5 Chapter Summary 106

8 Modelling Flagella with Mechanically-regulated Axonemes 109

8.1 Introduction 109

8.2 Governing Equations 111

8.3 Numerical Method 115

8.4 Chapter Summary 117

9 Conclusions 121

10 Appendices 125

10.1 The Stokesian Dynamics Method 125

10.2 Quaternions and Lie Algebra 133

10.3 Form of the Approximate Jacobian Matrix 136

11 Bibliography 139

List of Figures

1.1 Cross-sectional view of a sperm's flagellum, and a closer look at the structure of the axoneme. The axoneme runs along the length of the flagellum and provides the active force that drives it. 27

2.1 (a) Common swimming styles of microorganisms in Stokes flow; reproduced from Purcell (1977), with the permission of the American Association of Physics Teachers. (b) The 'stiff oar' movement, which is time-reversible because the velocities at every point of the 'oar' during the first half of the movement cycle (green arrows) are exactly *opposite* to the velocities at those points during the second half of the cycle (red arrows). 33

2.2 The velocity $\mathbf{u}$ at a point on the flagellum can be resolved into components normal and tangential to it. The force opposing normal velocity is *larger* than the force opposing tangential velocity, resulting in a net propulsive force, $\mathbf{f_{prop}}$. Reproduced from Lauga and Powers (2009) with permission. 34

2.3 The structure of the axoneme. Reproduced from Lindemann and Lesich (2010) with permission. 39

2.4 Schematic depicting the sliding of microtubules in the axoneme against each other. Reproduced from Lindemann (1994) with permission. 39

2.5 Left: Sea urchin sperm at (top) low water-like viscosity, exhibiting planar beating; (middle) high viscosity exhibiting helical beating; (bottom) very high viscosity exhibiting planar beating. Figure reproduced from Woolley and Vernon (2001) with permission. Right: Pigeon sperm at (top) low water-like viscosity exhibiting complex beating; (bottom) high viscosity exhibiting helical beating. Figure reproduced from Vernon and Woolley (1999) with permission. 42

3.1 Sperm will be modelled as an *Internally-driven Kirchhoff rod (IDKR)*. The control volume is a cross-sectional segment of infinitesimal thickness which *does not* include protein motors that provide the active driving force; the protein motors are assumed to occupy nine thin cylindrical volumes running along the length of the filament (outlined in red). 46

3.2 The control volume experiences external hydrodynamic forces and moments, internal active moments from protein motors and passive internal forces and moments that resist bending/twisting. 48

3.3 Pattern of protein motor activity (outer dynein arms) at three different points along the active flagellum of sea urchin sperm. The colour legend indicates the conformational state of the dynein motor: blue represents pre-power-stroke, red, orange and yellow represent intermediate states, and green represents the cross-link between microtubules 5 and 6. Figure reproduced from Lin and Nicastro (2018) with permission. 54

3.4 Overall algorithm based on bad Broyden's method to solve the system of equations to obtain positions and orientations of all filament segments at each time step. 61

4.1 Representative beat cycle of a planar beat at $S = 7, A = 5, k = 2\pi$. 66

4.2 Maximum curvatures of the emergent waveforms along the centerline over a beat period for $S = 7, 8, 9$ and 18, for $A = 15$ to 20, $k = 4\pi$. Arclength of $s = 0$ represents the 'head' of the swimmer. 67

4.3 Timelapse of the centerline over one beat cycle τ, at $S = 7$, $A = 15$ (top) and $A = 20$ (bottom), $k = 4\pi$. Centerlines have been translated such that the 'head' of the swimmer is located at (0,0) at each time point. 67

4.4 Cumulative sum of eigenvalues plotted against number of modes for $S = 18$, $A = 15 - 20$, $k = 4\pi$. Dot indicates sum of eigenvalues of first two modes. 68

4.5 (a) First (top panel) and second (bottom panel) spatially-dependent curvature modes for $A = 15$ to 20, $S = 7$ (left) and $S = 18$ (right), $k = 4\pi$. (b) First and second time-dependent coefficients plotted against each other over > 80 cycles for $A = 15$ to 20, $S = 7$ (left) and $S = 18$ (right), $k = 4\pi$. 68

4.6 Comparison of the normalised power spectral density of the first time-dependent coefficient of curvature at $A = 15$ for $S = 7, 8, 9$ and 18. 69

4.7 (a)-(d) Representative beat cycles of the four qualitative beating types obtained in simulations: (a) planar beat at $S = 7, A = 5, k = 2\pi$; (b) rolling-planar beat at $S = 5, A = 5, k = 2\pi$; (c) helical beat at $S = 12, A = 20, k = 4\pi$; (d) complex beat at $S = 15, A = 20, k = 4\pi$. Note that complex beats may look visually different at different parameters. (e)-(h) Microscope image of (e) bull sperm exhibiting planar beating; (f) human sperm exhibiting rolling-planar beating; (g) sea urchin sperm exhibiting helical swimming, reproduced from (Vernon and Woolley, 1999) with permission; (h) pigeon sperm exhibiting complex beating, reproduced from (Woolley and Vernon, 2001) with permission. Images (e) and (f) were provided by F. Yazdan Parast (Monash University). 70

4.8 Snapshot of 'looping' in a rolling-planar beat. 70

4.9 Depiction of pulsing in helical filaments. Top panel shows trajectory of the 'head' (black dot) in red over 4 beat cycles. Bottom panel shows the normalised power spectral density (PSD) of the z-coordinate of the head position (orange line) and the z-coordinate of the binormal material vector $\mathbf{d}_3$ at the head (black line), plotted against frequency normalised with respect to the driving frequency. 71

4.10 Top panel: Kymographs of centerline curvature magnitude for representative planar ($S = 9, A = 10, k = 4\pi$), rolling-planar ($S = 5, A = 5, k = 2\pi$), helical ($S = 12, A = 15, k = 4\pi$) and complex ($S = 15, A = 20, k = 4\pi$) beats as labelled, shown for six beat cycles. Bottom panel: Kymographs of centerline torsion magnitude for the same planar, rolling-planar, helical and complex beats respectively, shown for six beat cycles. 72

4.11 Top panel: Comparison of the normalised power spectral densities of the time-dependent components of centerline curvature magnitude for representative planar ($S = 9, A = 10, k = 4\pi$), rolling-planar ($S = 5, A = 5, k = 2\pi$), helical ($S = 12, A = 15, k = 4\pi$) and complex ($S = 15, A = 20, k = 4\pi$) beats as labelled, plotted against frequencies normalised using the driving frequency. Bottom panel: First (top) and second (bottom) curvature modes of the same planar, rolling-planar, helical and complex beats respectively. 72

4.12 Phase map showing the four types of beating for a dimensionless wavenumber of 2π (left) and 4π (right); colours of the dots represent the beating pattern type: planar (yellow), rolling-planar (purple), helical (blue) and complex (red). Dashed boxes highlight one possible set of parameters that correspond to the beat patterns of sea urchin sperm at 1 cP (planar), 1500 cP (helical) and 4000 cP (planar) in the order of increasing dimensionless frequency. Solid boxes highlight a set of parameters that may correspond to the beat patterns of bull sperm at 1 cP (rolling-planar) and above 20 cP (planar). 74

5.1 Parameter space showing the emergence of three types of beating at a dimensionless wavenumber of 4π, when considering only local anisotropic hydrodynamic drag (left) and when long-range hydrodynamic interactions are included (right). The plot on the right was presented earlier in Chapter 4 Figure 4.12. 79

5.2 Comparison of planar beat patterns obtained using local drag theory (yellow lines) and using the Stokesian Dynamics model (black lines). (a),(c) First (top panel) and second (bottom panel) spatially-dependent curvature modes for a planar swimmer at (a) $S = 7$, $A = 15$, $k = 4\pi$, and at (c) $S = 9$, $A = 15$, $k = 4\pi$. (b),(d) Plots of the first time-dependent coefficient of curvature against the second for the planar swimmers in (a) and (c) respectively. 80

5.3 Definition of the tangent angle θ for a planar swimmer. The depiction of a head in this figure is for illustrative purposes only. 81

5.4 Planar beat patterns obtained in 2D simulations. (a),(c) First (top panel) and second (bottom panel) spatially-dependent curvature modes for a planar swimmer at (a) $S = 9$, $A = 20$, $k = 4\pi$, and at (c) $S = 15$, $A = 20$, $k = 4\pi$ where the 3D simulations had predicted a complex non-planar beat. Yellow lines represent the 2D simulations, and black lines represent 3D simulations. (b),(d) Plots of the first time-dependent coefficient of curvature against the second for the swimmers in (a) and (c) respectively. 82

5.5 (a) Parameter map showing points where the planar base states are linearly stable (yellow) and unstable (red) to curvature perturbations. (b)-(c) Log_{10} of the L^2 norm of $\Omega_1^1(s)$ (black) and $\Omega_2^1(s)$ (magenta) as a function of time (shown in terms of beat cycles) for the points indicated in (a). Values are normalised with respect to the initial magnitude. 84

6.1 Top: Four equally-spaced time points in the individual beat cycles of a representative (a) rolling planar, (b) complex and (c) planar beat observed in bull sperm swimming in external medium viscosity of 1 cP, 5 cP and 75 cP respectively. Bottom: Kymographs of the 2D centerline curvature along the flagellum, up to the minimum extracted arclength. 90

6.2 Top panel: Mean light intensity over the head region of a rolling-planar (purple line) and planar (yellow line) bull sperm over 3 beat periods, obtained from microscope videos. Middle panel: Variation in the 2D projected length of the rolling-planar bull sperm, based on the plane of view shown in Figure 6.1. Bottom panel: Variation in the 2D projected length of a simulated rolling-planar sperm at $S = 2, A = 5, k = 2\pi$, based on the plane perpendicular to its direction of motion. 91

6.3 Parameter space presented in Chapter 4 showing the occurrence of the four types of beating for a dimensionless wavenumber of 2π; boxes indicate parameter estimates corresponding to the three beat pattern types of bull sperm at 1 cP, 5 cP and 75 cP. 91

6.4 Comparison of the normalised power spectral densities of the time-dependent components of centerline curvature for the representative planar (yellow), rolling-planar (purple) and complex (red) beats, for (top panel) the three representative sperm cells shown in Figure 6.1 and (bottom panel) the three points enclosed in solid squares in Figure 6.3. 92

7.1 Head trajectory of an originally planar swimmer ($S = 9, A = 12, k = 4\pi$) as it swims towards the wall, plotted against time shown in terms of beat cycles; insets show the beat waveform over one beat cycle when the filament is above $0.2L$ (top) and below $0.2L$ (bottom). The yellow highlight corresponds to a height of $0.02-0.22L$. 99

7.2 (a)-(b) First (top panel) and second (bottom panel) spatially-dependent curvature modes for (a) a planar swimmer at $S = 7$, $A = 12$, $k = 4\pi$, and (b) a quasi-planar swimmer at $S = 9$, $A = 12$, $k = 4\pi$. (b)-(c) Plots of the first time-dependent coefficient of curvature against the second for the same (c) planar swimmer and (d) quasi-planar swimmer. (e)-(f) Normalised power spectral density of the first time-dependent coefficient of curvature plotted against frequencies normalised using the driving frequency, for the same (e) planar swimmer and (f) quasi-planar swimmer. 100

7.3 Torsion of the centerline over 6 beat cycles in a rolling-planar swimmer at $S = 7$, $A = 18$, $k = 2\pi$ (top) and quasi-planar swimmer at $S = 9$, $A = 12$, $k = 4\pi$ (bottom). 101

7.4 Near-wall behaviour of a planar swimmer simulated using local drag theory, at a parameter set where a beat transition is observed in simulations considering long-range HI. Left: Head trajectory of the planar filament ($S = 9, A = 12, k = 4\pi$) as it swims above the wall, plotted against time shown in terms of beat cycles. Right: Plot over 200 beat cycles of the first time-dependent coefficient of curvature against the second. 101

7.5 Head trajectory of filament at $S = 7$, $A = 18$, $k = 4\pi$ as it swims towards the wall, plotted against time shown in terms of beat cycles; inset shows the beat waveform over one beat cycle. The filament at these parameters is planar in free space but exhibits rolling-planar motion near the wall for all points shown here. 102

7.6 (a) Curvature and (b) torsion of the centerline over 6 beat cycles for a rolling swimmer at $S = 7$, $A = 18$, $k = 4\pi$ initially at $1.5L$ above the wall. (c) Normalised power spectral density of the first time-dependent coefficient of curvature for the same swimmer, plotted against frequencies normalised using the driving frequency. (d) First (top panel) and second (bottom panel) spatially-dependent curvature modes for the same swimmer. 102

7.7 Accumulation height above the wall normalised with respect to filament length plotted against the dimensionless driving amplitude, for dimensionless wavenumber of 4π and dimensionless frequency of 7 (triangles) or 8 (circles). 103

7.8 (a) Head trajectory of a rolling-planar swimmer ($S = 2, A = 5, k = 2\pi$) as it swims towards the wall, plotted against time shown in terms of beat cycles; inset shows the beat waveform one beat cycle. (c) First (top panel) and second (bottom panel) spatially-dependent curvature modes for the swimmer in (a). (e) Plot over 6 beat cycles of the first time-dependent coefficient of curvature against the second. (b) Head trajectory of a helical swimmer ($S = 12, A = 21, k = 4\pi$) as it swims towards the wall, plotted against time shown in terms of beat cycles; inset shows the beat waveform one beat cycle and the blue highlight corresponds to a height of $0.02 - 0.32L$. (d) First (top panel) and second (bottom panel) spatially-dependent curvature modes for the swimmer in (b); solid lines correspond to the first 38 beat cycles, and dotted lines correspond to the last 2 beat cycles. (f) Plot over the first time-dependent coefficient of curvature against the second; the blue line indicates the first 38 beat cycles and black dotted line shows the last 2 beat cycles, which correspond to the blue highlight in (b). 104

7.9 Plots of tangential drag coefficient normalised with respect to the free-space tangential drag coefficient (dots), normal drag coefficient normalised with respect to the corresponding tangential drag coefficient (dashes) and binormal drag coefficient normalised with respect to the corresponding tangential drag coefficient (open circles). Black symbols/dashes denote results obtained using our Stokesian Dynamics calculations, pink symbols/dashes denote results obtained by Ramia et al. (1993) (re-plotted with permission) and the blue line denotes results obtained by Walker et al. (2019) (Figure 3 in the paper; licensed under CC BY 4.0) only for the normalised binormal drag coefficients. The horizontal axis corresponds to the distance from the wall h normalised by rod length L. 105

8.1 Sliding of microtubule doublets (black lines at the top and bottom) past each other due to the action of a dynein motor (structure in the center). Dotted lines show the sliding displacement, Δ. This image has been taken from Figure 1D in Sartori et al. (2016b) (licensed under CC BY 4.0) and has been edited to show the sliding displacement. 110

8.2 Section of the model flagellum containing two doublets (solid lines marked A and B) oriented parallel to the centerline (dashed-dotted line). Shaded circle depicts a single material cross section at a point s along the centerline. Orientations of material frame vectors $\mathbf{d_1}$ and $\mathbf{d_2}$, tangent $\mathbf{t}$ and normal $\mathbf{n}$ at s are shown using arrows. The active forces $\mathbf{f^a}$ experienced by the cross section are shown using the red arrows. 114

8.3 Overall algorithm based on bad Broyden's method to solve the system of equations to obtain positions and orientations of all filament segments at each time step. 118

10.1 Two spheres of equal radius a are separated by a distance r and are at a height h above the wall at $z = 0$. The spheres experience equal and opposite torques of magnitude $\mathbf{T}$ along the line joining their centres. Image reproduced from Swan and Brady (2007) with permission. 130

10.2 Results of Swan and Brady (2007): Normalized rotation rate of the doublet, $8\pi\mu a^3\mathbf{\Omega}/\mathbf{T}$ as a function of distance from the wall, h and particle separation distance r. Figure reproduced with permission. 131

10.3 Results using F-T (top) and F-T-S (bottom): Normalized rotation rate of the doublet, $8\pi\mu a^3\mathbf{\Omega}/\mathbf{T}$ as a function of distance from the wall, h and particle separation distance r. 132

1
Introduction

The motion of mammalian sperm through the female reproductive tract is a complex biological process vital to natural fertilisation. Sperm propel themselves through viscous fluids by actively beating their 'tails' or *flagella*. The complex beating patterns they exhibit are driven by an internal engine known as the *axoneme*, whose mechanism of working is yet to be well understood (Lindemann and Lesich, 2010). Sperm from different species have different morphologies and swimming patterns. However, even within the same species, sperm exhibit a range of different beating patterns when their environmental conditions change. For example, it has been observed experimentally in hamster sperm that a limited increase in the concentration of calcium ions in the cells causes their flagellar beat to become increasingly asymmetric (Pereira et al., 2017). Changes in the viscosity of the surrounding fluid can also lead to changes in swimming patterns (Gaffney et al., 2011). This study focuses on the effect of fluid viscosity as well as the presence of plane surfaces on the beating patterns.

Understanding how flagellar beat patterns change in these different environments can help us understand how sperm navigate their environments to reach the egg. Mammalian sperm, for example, navigate dynamically changing chemical gradients, temperatures, fluid viscosities and channel geometries within the female reproductive tract to reach the egg (Gaffney et al., 2011). Visualising sperm *in vivo* poses practical challenges; hence, much of the *in vivo* behaviour must be inferred from the laboratory or artificial reproduction setting, where the environment encountered by the sperm is very different and notably simpler. There is hence a need for a mechanistic understanding of why beat patterns change before one can make predictions of what beat patterns might look like *in vivo*. On that note, this work addresses the specific question:
"What mechanisms lead to changes in the beating patterns of sperm near walls and in fluids of different viscosities?"

The presence of walls has been observed to affect the swimming patterns of sperm across different species, and in a number of different ways. For example, sperm swimming in helical trajectories in bulk fluid switch to circular or curvilinear trajectories close to a plane wall. These include sperm from vastly different species such as sea urchin, mouse and chinchilla (Elgeti et al., 2010). Sperm tend to swim towards and accumulate at surfaces. This phenomenon is known as surface accumulation or capture, and is thought to be aided by hydrodynamic effects mediated by the surrounding fluid (Elgeti et al., 2010; Lauga and Powers, 2009). The focus of this work, however, is on the changes in beat waveform. It has been observed in experiments that human and bull sperm exhibiting a three-dimensional beating pattern in bulk fluid switch to a two-dimensional 'slithering' motion when swimming close to a wall (Nosrati et al., 2015). The speed of swimming in the slither mode was observed to be relatively faster (in human sperm) or slower (in bull sperm) than bulk-fluid swimming. Moreover, in human sperm, the slither mode was observed only in fluid viscosities above $\sim$20 times that of water. Beat changes due to fluid viscosity have been reported in various species of sperm, ranging from sea urchin (Woolley and Vernon, 2001) to avian (Vernon and Woolley, 1999) and mammalian sperm (Ishimoto et al., 2018). Sea urchin sperm have been reported to switch from a planar beat at low viscosity to a helical shape at high viscosity (Woolley and Vernon, 2001).

The current understanding is that such large changes in beat patterns must involve internal biochemical regulation, and some possible mechanisms have been theorised (Lindemann and Lesich, 2021; Woolley, 2003). This work explores the alternative possibility that beat pattern changes may be brought about by elastohydrodynamic mechanisms. This is inspired by the understanding that flagellar beat patterns emerge as a result of the interplay between the active driving provided by the axoneme, external hydrodynamic forces and the resistance of the flagellum to deformation (Figure 1.1). The exact mechanisms that give rise to observed beating patterns remain unknown, in part due to the limited understanding of the working mechanisms of the axoneme and the nature of the passive flagellar material's resistance to deformation. Yet, many theoretical studies have shown that elastohydrodynamic mechanisms can give rise to spontaneous oscillations in model flagella (Chakrabarti and Saintillan, 2019b; Oriola et al., 2017; Hilfinger, 2006; Camalet and Jülicher, 2000). While such studies provide the first demonstrations of the importance of elastohydrodynamics in determining flagellar beat patterns, these ideas remain to be explored in detail and studies are yet to produce results that would be easy to compare with experiments. With this in mind, we instead explore the role of elastohydrodynamic mechanisms in

beat *transitions*, which are more easily visualised in experiments. The choice of viscosity and wall-related beat transitions enables us to focus on the elastohydrodynamics alone, without the possible interference of biochemical mechanisms. This work uses a combination of theory and experimental data to show that, contrary to existing theories (Lindemann and Lesich, 2021), drastic beat transitions seen in sperm flagella may have elastohydrodynamic origins.

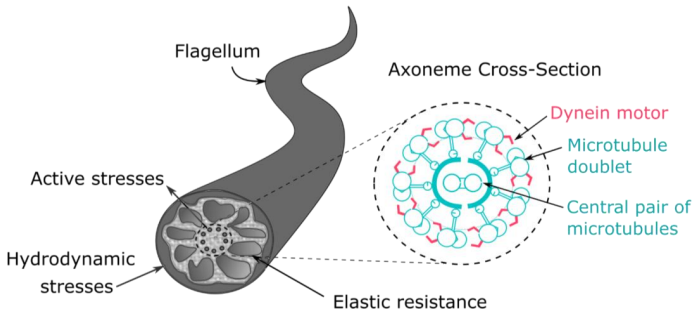

Figure 1.1: Cross-sectional view of a sperm's flagellum, and a closer look at the structure of the axoneme. The axoneme runs along the length of the flagellum and provides the active force that drives it.

To do this, the flagellum is modelled as a slender, inextensible elastic rod, i.e. Kirchhoff rod (Lim, 2010; Olson et al., 2013). The active driving provided by the axoneme is modelled as a prescribed simple travelling wave of active moments acting along the centerline (Gadêlha et al., 2010; Montenegro-Johnson et al., 2015). The chosen form of the active moment is inspired by recent experimental observations of the axoneme in sperm flagella (Lin and Nicastro, 2018), and its effect is similar to an 'active preferred curvature' (Elgeti et al., 2010). The hydrodynamic stresses experienced by the filament are modelled using Stokesian Dynamics (Swan and Brady, 2007) for a quiescent Newtonian fluid medium. We observe the motion of the internally-driven filament in two different hydrodynamic environments – bulk fluid of varying viscosities and in the presence of a plane wall. The internal driving is kept unchanged throughout, so that any beat pattern changes would be a result of elastohydrodynamic effects alone, and not due to biochemically-caused changes to the internal driving.

The next chapter provides more detailed background information and a review of literature to aid the reader's understanding of the remainder of this thesis. Following this, details of the model and solution technique are presented in Chapter 3.

In Chapter 4, planar and three-dimensional beat patterns that emerge

in bulk fluids of different viscosities are described and classified into qualitative types comparable to beat patterns in sperm. The results presented here suggest the first elastohydrodynamic mechanism behind the ability of flagella to exhibit helical as well as planar beating, which is a yet-unresolved mystery (Lindemann and Lesich, 2021). Trends in the beat patterns are also compared to experimental data available in the literature, and it is shown that the simulations are able to qualitatively predict viscosity-related changes in beating patterns that have been observed in sea urchin sperm. This provides the first evidence that such beat transitions may be purely elastohydrodynamic in nature and may not require changes in the internal driving, as currently theorised (Lindemann and Lesich, 2021).

Chapter 5 further explores the origins of the three-dimensional beats obtained in the previous chapter. Here it is shown that three-dimensional beating patterns emerge as a result of an elastohydrodynamic instability, and do not require the action of non-local hydrodynamic interactions. However, non-local hydrodynamic interactions can qualitatively affect the final form of the beat, especially where three-dimensional beats are observed. We then probe the linear stability of planar beat patterns to perturbations in the shape of the filament, and show that linear theory only captures part of the observed transition behaviour between planar and three-dimensional beating, suggesting that the instability involves nonlinear effects.

Chapter 6 presents an analysis of experimental data of bull sperm swimming in methyl cellulose solutions of different viscosities, with the aim of observing beat changes and comparing them with our simulations. The experimental data for this chapter was provided by F. Yazdan Parast (Monash University). This Chapter provides quantitative analyses of the differences between three qualitatively different beat patterns exhibited at different viscosities, and shows that the experimental beat patterns qualitatively match those predicted by the simulations.

In Chapter 7, simulations are used to study how the planar and three-dimensional beat patterns obtained in Chapter 4 change near a plane wall. At some parameters, beating patterns that are planar in bulk space accumulate at a fixed distance from the wall and switch to a quasi-planar beat at that height. While accumulation near a wall has been studied before in detail (Smith et al., 2009a; Ishimoto and Gaffney, 2014), this work presents the first evidence that quasi-planar beating such as that seen in sea urchin sperm (Woolley and Vernon, 2001) can emerge from an originally planar beat, without structural or driving asymmetries. It has traditionally been thought that the beat driven by the axoneme is

naturally helical, and the quasi-planar beat is a result of the 'flattening' of the helical beat (Lindemann and Lesich, 2021). The results in this Chapter also show that non-local hydrodynamic interactions play a significant role near a wall.

Finally, in Chapter 8, a new three-dimensional model for flagella which accounts for the presence of shear is presented, and a numerical method is suggested to solve it. This would enable future studies to take this work further by incorporating more detailed models of the axoneme. A potential future investigation could explore the role of mechanical-feedback-based regulation of the axoneme in supporting the experimentally-observed beat pattern changes in flagella.

Overall conclusions and future directions are summarised in Chapter 9.

2
Background and Literature Survey

The beating motions of cilia and flagella are central to many biological processes, ranging from locomotion of microorganisms such as sperm to the control of fluid flow and sensory functions (Badano et al., 2006). Although they perform a range of different functions, the structures of motile eukaryotic cilia and flagella are remarkably similar across many different species (Konno et al., 2012). Their beating patterns, however, are known to vary between species, within species and even as the same individual cilium or flagellum experiences different external environments. As noted in the previous Chapter, beating exhibited by sperm flagella is known to change drastically in fluids of different viscosities, or near surfaces (Gaffney et al., 2011). Answering the fundamental question *'How are flagellar beating patterns generated and controlled?'* is a precursor to understanding a range of different problems – from how sperm steer towards the egg, to how ciliopathies might occur. In addressing this question, sperm have long been used as model organisms due to the relative ease with which they can be modelled as well as studied experimentally.

Theoretical studies have attempted to uncover the mechanisms behind the complex beating patterns sperm exhibit by considering the fluid-structure interaction between the sperm and its surroundings (Gaffney et al., 2011). The motion of the swimmer originates from active stresses that act internally on the body of the flagellum. This motion causes the body to exert forces on the fluid. The fluid exerts an equal and opposite hydrodynamic force which, in turn, influences the motion of the swimmer. Moreover, the active stresses can be affected by several factors including the shape of the flagellum, the presence of external chemical gradients, and biochemical signals and regulators. Exactly how these factors influence flagellar beating patterns is yet to be understood, although some possible mechanisms have been proposed (Woolley, 2010; Lindemann and Lesich, 2010). Understanding the basic fluid-structure interaction problem would be the first step towards uncovering these

more complex relationships. This involves first identifying the forces or stresses acting on the sperm body, developing models for those stresses and then integrating those models into an overall representation of the sperm. The stresses on sperm can be broadly categorised into external stresses, passive internal stresses and the active internal driving. External stresses consist of the hydrodynamic stresses exerted by fluid surrounding the cell. Passive internal stresses arise due to the flagellum's resistance to bending and twist, whereas active stresses are provided by the axoneme within the flagellum to drive its motion.

Studies have explored various aspects of the fluid-structure problem individually or in combination. This Chapter provides an overview of the physics involved in the motion of sperm and describes the general approach taken by previous studies modelling sperm. The Chapter begins with a background on motion at very low Reynolds numbers and the adaptations that enable forward propulsion under such conditions. Following this, early studies modelling the hydrodynamics of flagellar propulsion are highlighted, and currently-used approaches to model flagellar hydrodynamics, internal stresses and active forcing are discussed. The final sections highlight the open questions that motivate this work.

2.1 Swimming at low Reynolds number

Sperm swim at a Reynolds number in the order of 10^{-4}, which would be similar to the Reynolds number of a man swimming in a pool of molasses at under 1 cm/min (Purcell, 1977). Flow at low Reynolds number is characterised by the dominance of viscous forces as opposed to inertia, presenting an environment where the swimmer experiences nearly *zero net force*. In the absence of other external forces, the forces exerted by the swimmer at every point on its body surface are completely balanced by the hydrodynamic forces exerted by the fluid. Fluid flow in this regime can be approximated by the Stokes equations for a closed system:

$$\boldsymbol{\nabla}.\mathbf{u} = 0; \tag{2.1}$$

$$\boldsymbol{\nabla}.\boldsymbol{\sigma} = 0, \tag{2.2}$$

where $\mathbf{u}$ is the fluid velocity and $\boldsymbol{\sigma}$ is the hydrodynamic stress tensor. The Stokes equations are *time-independent*; however, time-dependence can be brought about through time-dependent boundary conditions. For a Stokesian swimmer undergoing a cyclic series of deformations, its net displacement per cycle only depends on the sequence of configurations and not on the *rate* at which the cycle progresses or repeats. Purcell provides the example of the scallop, a clam-like organism that moves by opening its shell slowly and shutting it fast, squirting out water to push

itself forward. In the Stokes regime, the scallop would not be able to produce any net movement because its cycle of motion involves the same series of configurations in forward and reverse; the motion induced by the first half of the cycle would therefore be reversed in the second half (Figure 2.1(b) shows an example of such motion). This is the famous *Scallop theorem*, which illustrates how a lack of time-dependence affects motion in the Stokes regime. Microswimmers in nature overcome this problem by swimming in an *asymmetric* manner. Purcell notes two common types of swimming cycles observed in flagellated organisms, the 'corkscrew' and the 'flexible oar' (Figure 2.1(a)). The motion of a corkscrew is known to be naturally asymmetric. The asymmetry in the flexible oar, however, may be better understood when it is compared to the symmetric 'stiff oar' (Figure 2.1(b)).

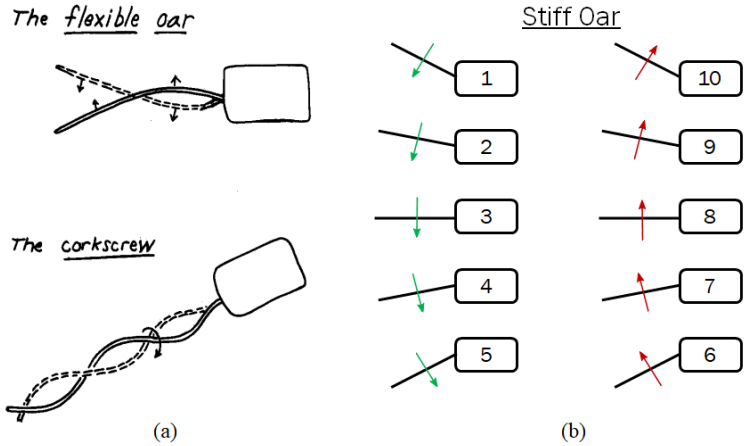

Figure 2.1: (a) Common swimming styles of microorganisms in Stokes flow; reproduced from Purcell (1977), with the permission of the American Association of Physics Teachers. (b) The 'stiff oar' movement, which is time-reversible because the velocities at every point of the 'oar' during the first half of the movement cycle (green arrows) are exactly *opposite* to the velocities at those points during the second half of the cycle (red arrows).

Asymmetry in swimming is linked to the *drag-based propulsion* of these swimmers. An important feature of Stokes flow is *anisotropy* in fluid drag, which organisms exploit to generate forward thrust. In the context of a planar slender filament as in Figure 2.2, the drag force component normal to the filament would be about twice as large as the tangential drag force component, creating a net force which propels the filament (Lauga and Powers, 2009). This anisotropy is implicit in the solution of the Stokes equation itself, as will be explained in the following section. If the normal and tangential drag forces were equal, the resultant force on the filament would simply oppose the motion of the filament. The physics behind drag-based locomotion is discussed in

detail in Lighthill (1976), and Lauga and Powers (2009) provide a mathematical description of the same.

2.2 Modelling Flagellar Hydrodynamics

Many early theoretical studies aimed to determine the propulsive thrust of a swimmer by *prescribing its motion*, and relating its kinematics with hydrodynamics. This review focuses only on motion in a quiescent Newtonian fluid. Efforts to model swimmers at low Reynolds number date back to the classical study by Taylor (1951), which provides a theoretical framework for the self-propulsion of undulating infinite plane sheets in viscous fluid. His approach was, however, not applicable to undulations of large amplitudes in the range typical to microorganisms like sperm. Addressing this limitation, Hancock (1953) analysed the propulsion velocity of thin filaments that propagate two or three-dimensional waves along their lengths, drawing inspiration from Stokes' solution for steady viscous flow past a rigid sphere. He obtained equations for the propulsion velocity of infinite as well as finite thin filaments, and analysed the effect of a non-zero filament radius.

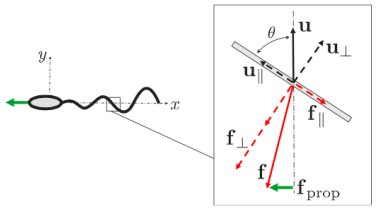

Figure 2.2: The velocity $\mathbf{u}$ at a point on the flagellum can be resolved into components normal and tangential to it. The force opposing normal velocity is *larger* than the force opposing tangential velocity, resulting in a net propulsive force, $\mathbf{f_{prop}}$. Reproduced from Lauga and Powers (2009) with permission.

A model for sperm motion emerged shortly after, in the form of the *Resistive Force Theory* (RFT; Gray and Hancock, 1955). In this work, Gray and Hancock modelled the tail of the sperm as a series of rigid segments conforming to a wave. The velocity $\mathbf{u}$ of each rigid segment was related to the hydrodynamic forces $\mathbf{f^h}$ acting on it through localised resistance coefficients ζ in the normal ($\perp$) and tangential ($||$) directions (Figure 2.2):

$$\mathbf{u} = -\zeta_{||}\mathbf{f}^{\mathbf{h}}_{||} - \zeta_{\perp}\mathbf{f}^{\mathbf{h}}_{\perp}.$$

Approximating the normal drag coefficient to be twice of the tangential drag coefficient, they showed that their calculated results closely agree with experimental data for sea urchin sperm. Their relatively simple method enabled preliminary analyses of various flagellar dynamics problems of the time. Versions of the RFT (such as Lighthill's version (Lighthill, 1976)) remain widely used in both experimental (Mondal et al., 2020; Nandagiri et al., 2021) as well as theoretical studies (Oriola et al., 2017; Moreau et al., 2018; De Canio et al., 2017) due to the simplicity and low computational cost of the approach.

An improvement to the RFT emerged about twenty years later in Lighthill's 1976 lecture (Lighthill, 1976), which argued that the localised friction coefficients proposed by Gray and Hancock did not fully account for *long-range* hydrodynamic interactions characteristic of Stokes flow.

In the proximity of no-slip boundaries, these long-range hydrodynamic interactions are screened (Lauga and Powers, 2009). The RFT would not be suitable in the presence of ambient flows or flow disturbances from other swimmers (Brokaw, 2006). Taking a similar approach to Hancock (1953), Lighthill (1976) proposed that the flagellum may be represented as a series of rigid spheres. This method came to be known as Lighthill's *Slender Body Theory* (SBT), in light of the simplification that the radius of the flagellum is negligible in comparison to its length. Each sphere would be represented by the flow field induced by a point force and a force dipole at the centre of the sphere, which together produce a constant resultant velocity at the sphere's surface. Using appropriate Green's functions to represent the flow, one can ensure that the continuity and Stokes equations are satisfied and hence, the hydrodynamics of the problem is represented more accurately.

A point-force-induced flow field represented using such a Green's function is termed the *Stokeslet*, and the fundamental solution of the Green's function, $\boldsymbol{\mathcal{G}}$ given below is known as the Oseen tensor. Here $\mathbf{u}(\mathbf{x})$ represents the flow field at $\mathbf{x}$, $\mathbf{f}(\mathbf{x_0})$ is the point force at $\mathbf{x_0}$ that drives the flow, and $\mathbf{I}$ is the identity tensor:

$$\mathbf{u}(\mathbf{x}) = \frac{1}{8\pi\mu}\boldsymbol{\mathcal{G}}(\mathbf{x}-\mathbf{x_0}).\mathbf{f}(\mathbf{x_0}), \tag{2.3}$$

$$\text{where} \quad \boldsymbol{\mathcal{G}} = \frac{\mathbf{I}}{|\mathbf{x}-\mathbf{x_0}|} + \frac{(\mathbf{x}-\mathbf{x_0})(\mathbf{x}-\mathbf{x_0})}{|\mathbf{x}-\mathbf{x_0}|^3}.$$

Taking a closer look at the Stokeslet, we realise the origin of *drag anisotropy* in Stokes flow, embodied in the second term of the Green's function. As discussed before, this anisotropy forms the basis for drag-based propulsion of microswimmers in the Stokes regime. Considering that the velocity on the swimmer's surface is equal to the fluid velocity $\mathbf{u}(\mathbf{x})$ at its surface, a swimmer exerting a point force $\mathbf{f}$ on the fluid would be propelled at a velocity $\mathbf{u}$ in a different direction to the hydrodynamic reaction force, $-\mathbf{f}$.

The Stokeslet velocity field becomes singular at the origin of the point force. Derivatives of the Stokeslet with respect to position $\mathbf{x}$ are higher-order solutions of the Stokes equation to other point singularities at the origin. The Stokes doublet, for example, is a directional derivative of the Stokeslet (Ainley et al., 2008) and is a solution of the Stokes equations to a force dipole at the origin. Flow fields can be represented as linear combinations of appropriate singular solutions; methods that take advantage of this are known as *singularity methods*, described in detail in Pozrikidis (1992).

These methods can be used to analyse the flow due to an undulating flagellum in free space or near simple wall geometries. For example, flow around swimmers in a semi-infinite domain near an infinite plane wall can be modelled after modifying the form of the Stokeslet (2.3) to include an image system of singularities developed by Blake (1971). This image system (likely named so because its position is that of a 'mirror image' of the Stokeslet, the plane wall being the mirror) consists of a set of singularities placed on the other side of the 'wall' to exactly cancel out the flow induced by the Stokeslet at the wall, and hence satisfy no-slip conditions at the wall.

Apart from Slender Body Theory, variations of which are also currently used in computational studies (Sangani and Gopinath, 2020; Chakrabarti and Saintillan, 2019b), another traditional singularity-based approach is the Stokesian Dynamics model (Durlofsky et al., 1987; Bossis et al., 1991). This method, which is also known as the Rotne-Prager-Yamakawa tensor (Wajnryb et al., 2013), was originally used for colloidal systems but has recently been applied to flagella-like filaments (Schoeller et al., 2021; Delmotte et al., 2015; Veeraragavan and Prabhakar, 2020). Like the SBT, this method assumes that the flagellum behaves hydrodynamically like a chain of rigid spheres. The main difference is that in this model, the chain of 'spheres' is discrete, whereas in SBT it is a continuous distribution along the centerline.

An inherent limitation in the singularity methods is the presence of singular points in the flow, around which computations can become numerically unstable. This limitation has driven the development of new techniques such as the Method of Regularized Stokeslets (Cortez, 2001). This method involves the replacement of Stokeslets with *regularized Stokeslets*, which represent the flow field due to a regular force distribution dictated by a cutoff function, rather than a point force. Cortez et al. (2005) provide examples involving the application of regularized Stokeslets within the framework of the *boundary integral equation*, which is an integral form of the Stokes equation (Pozrikidis, 1992). The use of regularized Stokeslets eliminates the presence of singular points in the flow and hence enables the computation of the flow field on the 'surface' of the swimmer. The method has been applied in several recent studies modelling flow driven by filaments (Olson et al., 2013; Huang et al., 2018), and it bears likeness to the original singularity methods. However, regularization introduces an additional source of error which depends on the form of the force distribution and is linked to the level of discretization. The nature of the flow field produced by regularized forces and the effects of the cutoff function on the regularization error have been analysed by Zhao et al. (2019). The method has also

been extended to swimmers near a plane wall, using a regularized image system inspired by Blake's image system of singularities (Ainley et al., 2008). Cortez (2018) proposed a variation of the method of regularized Stokeslets in which the regularization and discretization errors can be decoupled for a large enough discretization. A numerical implementation of this method, known as Regularized Stokeslet Segments (RSS), is presented in Walker et al. (2019).

Another class of methods are the Immersed Boundary (IB) methods introduced by Peskin (2002) which are more accurate, but more computationally demanding. A comparison of the method of regularized Stokeslets and the generalised IB method can be found in the computational study by Olson et al. (2013) investigating the motion of an undulating flagellum in viscous fluid. Boundary Element Methods (BEM) are another type of high-accuracy methods which have been used in flagellar propulsion for a long time (Ramia et al., 1993). More recently, Multi-Particle Collision Dynamics (MPC) (Yang et al., 2008; Elgeti et al., 2010) and Lattice-Boltzmann (LB) methods (Liu et al., 2020) have also been used, which involve simulating the fluid as a collection of particles. These methods are powerful tools for highly complex geometries, although for simple domains they would be much more computationally expensive in comparison to methods based on Green's functions. Ultimately, one's choice of method would depend on a combination of computational cost, ease of implementation and degree of hydrodynamic detail desired.

2.3 Modelling Internal Stresses

Flagella have long been thought of as slender elastic filaments (Gray, 1955; Machin, 1958). The passive internal stresses arising from the planar deformations of a flagellum have thus commonly been modelled using elasticity theories, such as the Euler-Bernoulli beam theory. In some studies, the flagellum itself is modelled as an inextensible, unshearable elastic beam (De Canio et al., 2017; Moreau et al., 2018; Machin, 1958). On the other hand, studies focused on modelling the axoneme have modelled the flagellum or axoneme as a pair of inextensible beams which can 'slide' relative to each other, such that the structure as a whole can *shear*. This *sliding filament* model has been extensively applied to study planar filament oscillations (Brokaw, 1972; Lubliner and Blum, 1977; Hines and Blum, 1978; Camalet and Jülicher, 2000; Riedel-Kruse et al., 2007; Gadêlha et al., 2010; Sartori et al., 2016a; Gadêlha and Gaffney, 2019). The relevance of shear in a flagellum is discussed in the following section.

The sliding filament model has also been extended to three-dimensional

ensembles of nine filaments (Hilfinger and Jülicher, 2008; Sartori et al., 2016a; Rallabandi et al., 2022). In three dimensions, flagella are also commonly modelled as *Kirchhoff rods* (Dill, 1992), i.e. slender, inextensible and unshearable rods (Olson et al., 2013; Huang et al., 2018; Ling et al., 2018; Carichino and Olson, 2019; Walker et al., 2020a; Ishimoto and Gaffney, 2018; Ling et al., 2018). In Kirchhoff rod theory, the geometry of the filament is represented using the 'centerline' of the filament along with a three-dimensional material frame at every point along the centerline (as described in the next chapter). Constitutive relations are used to describe the resistance of the elastic filament to bending and twisting.

Others have used a discrete beads-and-springs approximation for the filament, where the elastic resistance is incorporated in the form of an additional spring potential (Elgeti et al., 2010; Delmotte et al., 2015). On the other hand, flagella have also been modelled as weakly extensible but unshearable filaments using continuum models (Olson et al., 2013; Ishimoto and Gaffney, 2018). In both continuum and discrete approaches, geometric nonlinearities as well as the inextensibility and unshearability of the filament introduce numerical stiffness to the problem (Moreau et al., 2018), which becomes more significant when beat amplitudes become large (Gadêlha et al., 2010). Efficient numerical algorithms have hence been developed to enable the implementation of these methods for flexible filaments in three dimensions (Delmotte et al., 2015; Nazockdast et al., 2017; Schoeller et al., 2021; Walker et al., 2020a; Rostami and Olson, 2016).

An inherent limitation to all of the discussed methods is the availability of experimental data on necessary material properties of flagella such as their bending stiffnesses. While measurements of the elastic bending stiffness have been made for certain species (Lindemann and Lesich, 2016), values have been shown to vary by an order of magnitude in some cases depending on various factors such as ATP or ADP concentration in the surrounding fluid (Lindemann et al., 1973; Lindemann and Lesich, 2016). On the other hand, some studies suggest that the flagellar material has significant internal friction (Mondal et al., 2020; Nandagiri et al., 2021), and that purely elastic filament models would be insufficient. Determining the constitutive relations of the flagellar material is hence an ongoing challenge.

2.4 Modelling Active Stresses

The more elusive part of this problem is the nature of *active stresses* exerted by the axoneme, the internal 'engine' which runs along the length of the flagellum. The structure of the axoneme is fairly well understood (Satir et al., 2014). In most eukaryotic species, it consists of a pair of microtubules surrounded by nine microtubule doublets (Figure 2.3), on the surfaces of which dynein protein motors exert forces that cause doublets to slide relative to one another (Figure 2.4). The collective activity of tens of thousands of protein motors distributed along the length of the axoneme leads to the propagation of bends along the flagellum, enabling it to oscillate (Lin and Nicastro, 2018). Experiments suggest that the activity of axoneme may be regulated by mechanical feedback from the motion of the flagellum (Izawa and Shingyoji, 2020). However, the exact mechanisms through which oscillations are generated and regulated remain a mystery (Satir, 1968; Lindemann and Lesich, 2021), and this presents the main challenge in modelling flagellar dynamics.

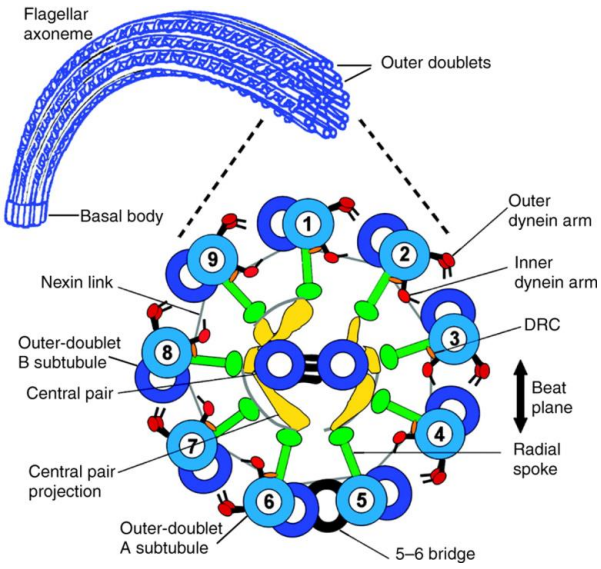

Figure 2.3: The structure of the axoneme. Reproduced from Lindemann and Lesich (2010) with permission.

Studies have modelled the axonemal driving at various degrees of abstraction. The simplest models treat the axonemal driving as a predetermined distribution of active forces or moments acting along the centerline. In these 'open-loop' models, the axonemal driving is not coupled to the motion of the flagellum. Examples include imposing known sinusoidal travelling waves of cross-sectional moments (Hall-McNair et al.,

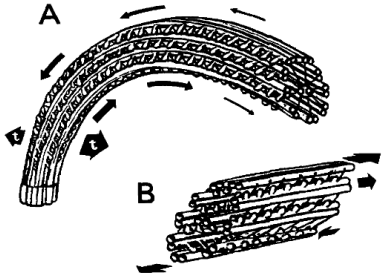

Figure 2.4: Schematic depicting the sliding of microtubules in the axoneme against each other. Reproduced from Lindemann (1994) with permission.

2019; Gadêlha et al., 2010; Montenegro-Johnson et al., 2015; Walker et al., 2020a; Ishimoto and Gaffney, 2018), imposing time-varying preferred curvature (Elgeti et al., 2010; Olson et al., 2013; Simons et al., 2015; Delmotte et al., 2015), and applying 'follower forces' which act along the axial direction of the flagellum (Ling et al., 2018; Fily et al., 2020; De Canio et al., 2017).

On the other hand, 'closed-loop' mechanistic models have also been proposed in which this distribution of active forces or moments is not predetermined, but is instead coupled to filament geometry or motion. For example, three main postulates have been the focus of numerous studies – sliding-control, curvature-control and transverse-force-control. Sliding-control models hypothesize that the active forces are regulated by the degree to which adjacent microtubules in the axoneme slide past each other, i.e. the *sliding displacement* and its time derivatives (Camalet and Jülicher, 2000; Riedel-Kruse et al., 2007; Sartori et al., 2016b; Oriola et al., 2017; Chakrabarti and Saintillan, 2019b). In curvature-control models the active force is regulated primarily by filament curvature and its time-derivatives (Brokaw, 1972; Sartori et al., 2016a,b). In transverse-force-control models such as the the Geometric Clutch (GC) model (Lindemann, 1994; Bayly and Wilson, 2014), forces generated perpendicular to the long axis of the axoneme regulate the active forces by determining whether or not dynein motors are able to attach to the adjacent microtubule. All three types of mechanically-regulated axoneme models have successfully been used to demonstrate that beating patterns can emerge spontaneously due to elastohydrodynamic instabilities.

Others have suggested that the activity of dynein motors is biochemically or mechano-chemically regulated via other components within the axoneme, such as the central-pair-spoke apparatus (Lindemann and Lesich, 2010). Specifically, the CP-spoke apparatus is thought to act as a 'distributor' of signals that activate or inactivate specific sets of dynein motors (Bower et al., 2013). While the exact mechanism is not clear, it has been hypothesised that regulation occurs through the phosphorylation and dephosphorylation of the dynein arms via biochemical complexes that are anchored within the axoneme (Wirschell et al., 2011). Furthermore, various biochemical signals including Ca^{2+} ions have been shown to be involved in dynein regulation, although the exact mechanism of how they contribute to the overall beat pattern remains elusive (King, 2012). The role of calcium signalling in flagellar beating has been investigated in recent modelling studies (Olson et al., 2011; Simons et al., 2014; Carichino and Olson, 2019).

We can hence identify two major schools of thought on how the dynein

motors in the axoneme are regulated – the first is that they are regulated mechanically through the forces generated within the flagellum, and the second is that they are regulated primarily through biochemical mechanisms.

2.5 The Importance of Beat Transitions

While several mechanisms have been suggested to explain the emergence and control of flagellar beat patterns, verifying the proposed mechanisms experimentally remains a challenge. Studies have taken the approach of quantitatively comparing beat waveforms predicted by their models to experimental waveforms, in an effort to distinguish between the different hypotheses (Sartori et al., 2016b,a). An alternative, largely untapped avenue for verifying the different mechanisms is the use of models to predict *beat transitions*.

Passive external environments (which involve no biochemical changes) can exert a dramatic influence on flagellar beating patterns. For example, sea urchin sperm have been observed to predominantly exhibit planar beating at water-like viscosity, helical beating in fluids of high viscosity and planar beating again at very high fluid viscosities (Woolley and Vernon, 2001). Avian sperm such as quail or pigeon sperm exhibit 'complex' three-dimensional beats at water-like viscosity, but have helical beats at high viscosity (Vernon and Woolley, 1999). The beat transitions of sea urchin and pigeon sperm are shown in Figure 2.5. In contrast, mammalian sperm such as bull and human sperm exhibit rolling beats at low viscosity and planar beats at high viscosities (Hyakutake et al., 2015b; Zaferani et al., 2021; Ishimoto et al., 2018).

The presence of plane surfaces such as the microscope slide over which sperm samples are deposited can also affect beating patterns. Woolley and Vernon (2001) report that sea urchin sperm exhibit quasi-planar beating away from the microscope slide and planar beating when very close to the surface of the slide. Similar behaviour has been observed in bull and human sperm (Woolley, 2003; Nosrati et al., 2015), which exhibit rolling away from the surface but switch to a planar 'slithering' beat when within one micrometre of the surface.

The transition between planar and helical or three-dimensional beating is particularly fascinating because the structure of the axoneme suggests that it may naturally produce a helical beat, but planar beating sperm seem to have a natural swimming advantage (Guerrero et al., 2011). Experimental evidence moreover suggests that the pattern of

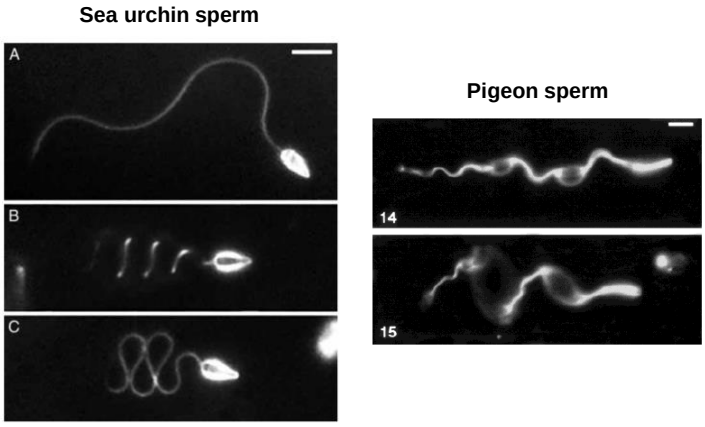

Figure 2.5: Left: Sea urchin sperm at (top) low water-like viscosity, exhibiting planar beating; (middle) high viscosity exhibiting helical beating; (bottom) very high viscosity exhibiting planar beating. Figure reproduced from Woolley and Vernon (2001) with permission. Right: Pigeon sperm at (top) low water-like viscosity exhibiting complex beating; (bottom) high viscosity exhibiting helical beating. Figure reproduced from Vernon and Woolley (1999) with permission.

protein motor activity in the axoneme naturally produces planar beats (Lin and Nicastro, 2018), although alternative interpretations have been suggested which would allow the axoneme to produce both planar as well as helical beats through changes in the pattern of motor activity (Lindemann and Lesich, 2021). Large beat pattern transitions are hence thought to involve regulation of the dynein motors through some unknown biochemical or mechano-chemical mechanism. Woolley and Vernon (2001) provide a preliminary description of a mechano-chemical mechanism that could trigger beat pattern changes in fluids of high viscosity.

2.6 Aims

This work explores another possibility which has previously not been studied – that beat pattern changes may have elastohydrodynamic origins, and do not involve axonemal regulation. The primary aim of this work is to show that simple, predetermined internal driving coupled with an elastohydrodynamic instability can produce the flagellar beat transitions observed in experiments. As discussed in the previous chapter, the focus of this study is on beat pattern changes exhibited by sperm in fluids of different viscosity as well as near a plane wall.

The flagellum is modelled in three dimensions as an Internally-driven Kirchhoff Rod (IDKR) (Nandagiri et al., 2021), with the internal driving

consisting of a simple predetermined travelling wave of active bending moments. The hydrodynamics of the filament is modelled using the Stokesian Dynamics method (Durlofsky et al., 1987; Swan and Brady, 2007). To simulate the motion of the flagellum, the system of nonlinear and numerically-stiff equations is solved using the efficient algorithm proposed by Schoeller et al. (2021) for suspensions of passive elastic filaments. The model and numerical methods are described in the next Chapter.

Simulation results tracking the emergent motion of the flagellum in Newtonian fluid of different viscosities are presented in Chapter 4. The two- and three-dimensional beat waveforms obtained at different parameter values are classified into four major qualitative types, based on visual comparisons as well as quantitative comparisons of beat waveforms using Proper Orthogonal Decomposition (POD) of the centerline curvature profile. POD of centerline curvature has been used in previous experimental studies to compare beat waveforms (Guasto et al., 2020; Smith et al., 2009a). Beat transitions predicted by simulations are compared to literature data of sea urchin sperm swimming in media of different viscosities (Woolley and Vernon, 2001).

Previous studies applying similar internal driving have not reported three-dimensional beating patterns without imposed asymmetries in the structure (Elgeti et al., 2010; Ishimoto and Gaffney, 2018) or changes in the internal driving (Ishimoto and Gaffney, 2018; Walker et al., 2020a). Hence, Chapter 5 probes the emergence of three-dimensional beating in the simulations discussed in the previous Chapter. Considering the important role of long-range hydrodynamic interactions in bacterial flagellar propulsion (Lauga, 2016) as well as synchronisation in eukaryotic cilia and flagella (Brumley et al., 2012; Chakrabarti and Saintillan, 2019a), the role of long-range hydrodynamic interactions is first explored by comparing simulations using the Stokesian Dynamics model to simulations performed using Resistive Force Theory. Secondly, the presence of elastohydrodynamic instabilities leading to non-planarity is investigated through a linear stability analysis. This is informed by the observations of helical buckling in passive filaments in compressional flows (Chakrabarti et al., 2020). In the context of internally-driven filaments, many previous studies have used linear stability analyses to investigate the emergence of spontaneous oscillations in flagella due to elastohydrodynamic instabilities (Camalet and Jülicher, 2000; De Canio et al., 2017; Oriola et al., 2017; Rallabandi et al., 2022).

Chapter 6 presents an analysis and comparison of experimental two- and three-dimensional beat waveforms of bull sperm in media of dif-

ferent viscosities. The aim is to compare observed beat transitions as well as the beat patterns themselves to the simulation results in Chapter 4. While literature data is available for bull sperm swimming in fluids of different viscosities (Hyakutake et al., 2015b; Zaferani et al., 2021), studies have not provided a detailed quantitative analysis of the different waveforms which would allow close comparisons with simulations. The experimental data for this chapter was provided by F. Yazdan Parast at Monash University and the quantitative analysis of the experimental waveforms (using POD of the centerline curvature profile) is presented in this work.

Chapter 7 aims to investigate beat transitions near a plane wall using simulations of an IDKR. The model and numerical methods are the same as in Chapter 4, except that the free-space Stokesian Dynamics tensors are replaced with the near-wall tensors (Swan and Brady, 2007). Changes in the overall trajectory as well as the waveform are studied for each of the different types of beat patterns obtained in Chapter 4.

Chapter 8 presents a new three-dimensional model for an inextensible but shearable flagellum which is driven internally by a mechanically-regulated axoneme. Currently available three-dimensional models of mechanically-regulated axonemes, which consider a nine-filament geometry, consider sliding or shear displacements between individual filaments but neglect shearing of the cross sections of the overall ensemble (Hilfinger and Jülicher, 2008; Sartori et al., 2016a; Rallabandi et al., 2022). This chapter aims to provide a more consistent and general three-dimensional framework for shearable flagella containing mechanically-regulated axonemes, to allow future studies to investigate beat transitions in mechanically-regulated flagella. The proposed model is an adaptation of the Cosserat rod model discussed in (Gazzola et al., 2018) for extensible, shearable filaments to ensure inextensibility while allowing bending and shear. This is coupled to a general sliding-controlled mechanical model of the axoneme inspired by previous work (Camalet and Jülicher, 2000; Riedel-Kruse et al., 2007).

A summary of the findings of this work is provided in Chapter 9 along with suggestions for future work.

3
Methods

This chapter provides details of the Internally-driven Kirchhoff rod (IDKR) model, which is used in Chapters 4-7 to model the motion of an individual sperm. The numerical methods used in the simulations of Chapters 4 and 7 are then described. The final section briefly discusses the use of Proper Orthogonal Decomposition (POD) to extract information about flagellar beat patterns.

3.1 Modelling the Flagellum as an Internally-driven Kirchhoff Rod

The IDKR model (Nandagiri et al., 2021) treats the flagellar material as a Kirchhoff rod, but additionally accounts for the active internal driving provided by the axoneme. Kirchhoff rods are slender elastic rods that can bend and twist, but cannot stretch or shear (Dill, 1992; Coleman et al., 1993). As discussed in Chapter 2, Kirchhoff rod theory has been widely used to model flagella in three dimensions. This section presents a description of the rod geometry and a physics-based derivation of the general governing equations as provided in Nandagiri et al. (2021), and outlines the constitutive relations required to complete the system of equations.

Geometry and Material Frame

Every point on the flagellum, which shall henceforth be referred to as the 'filament', is described by its *material coordinate*. The set of material points that make up the *centerline* of the filament (shown in Figure 3.1) will have a set of material coordinates denoted as s, the arc length variable. In the context of an *inextensible* rod, the centerline of the filament is a line comprising material points that have a fixed distance between them such that the length of the centerline or any part of it always remains constant.

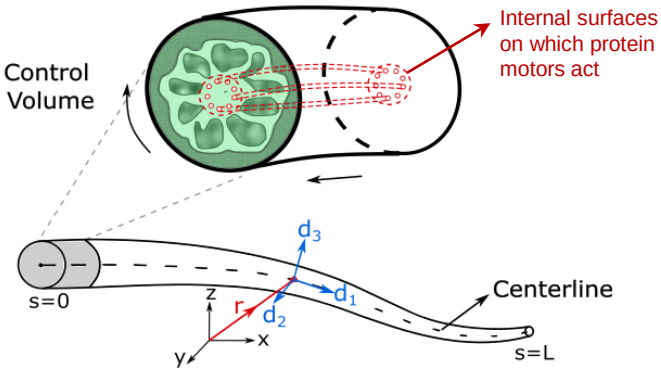

Figure 3.1: Sperm will be modelled as an *Internally-driven Kirchhoff rod (IDKR)*. The control volume is a cross-sectional segment of infinitesimal thickness which *does not* include protein motors that provide the active driving force; the protein motors are assumed to occupy nine thin cylindrical volumes running along the length of the filament (outlined in red).

The arc length variable s is defined as

$$(ds)^2 = d\mathbf{r} \cdot d\mathbf{r} = (dx)^2 + (dy)^2 + (dz)^2, \tag{3.1}$$

where $\mathbf{r}(s,t)$ is the position vector of a point on the centerline at s. The local *material frame* at every point s is defined by an orthonormal triad of unit vectors denoted as $\mathbf{d}_1$, $\mathbf{d}_2$ and $\mathbf{d}_3$, shown in Figure 3.1 in blue. These vectors are represented in a compact form as $\mathbf{d_a}$ where $a \in \{1,2,3\}$.

In an *unshearable* rod, the cross section at any point on the centerline is perpendicular to the centerline. The material frame vector $\mathbf{d}_1$ is then equal to the centerline unit tangent vector:

$$\mathbf{d}_1 = \frac{\partial \mathbf{r}}{\partial s}. \tag{3.2}$$

We shall henceforth use the term 'tangent' for $\mathbf{d}_1$. The vector $\mathbf{d}_1$ is hence perpendicular to the cross section, and vectors $\mathbf{d}_2$ and $\mathbf{d}_3$ lie in the plane of the cross section, such that

$$\mathbf{d}_1 \times \mathbf{d}_2 = \mathbf{d}_3. \tag{3.3}$$

The rotation of the material frame with s is given by

$$\frac{\partial \mathbf{d_a}}{\partial s} = \mathbf{\Omega} \times \mathbf{d_a}, \tag{3.4}$$

where $\mathbf{\Omega}$, the Darboux rotation vector, is resolved in the local material frame as

$$\mathbf{\Omega} = \Omega_1 \mathbf{d}_1 + \Omega_2 \mathbf{d}_2 + \Omega_3 \mathbf{d}_3, \tag{3.5}$$

with

$$\Omega_a = \frac{\partial \mathbf{d_b}}{\partial s}.\mathbf{d_c}, \tag{3.6}$$

where a,b,c $\in \{1, 2, 3\}$ follows a cyclic permutation. From this we observe that the change in the tangent with respect to s, which can be referred to as *bending*, depends only on Ω_2 and Ω_3. These two components of $\mathbf{\Omega}$ are therefore referred to as *curvatures*. The other component Ω_1 is called the *twist*.

The time rate of change of the material frame vectors can be represented in an analogous form to equation (3.4), as

$$\frac{\partial \mathbf{d_a}}{\partial t} = \boldsymbol{\omega} \times \mathbf{d_a}. \tag{3.7}$$

Here, $\boldsymbol{\omega}(s, t)$ is the angular rotation rate of the cross section about the point s. It can be shown that the following compatibility relationship exists between $\boldsymbol{\omega}$ and $\mathbf{\Omega}$:

$$\frac{\partial \boldsymbol{\omega}}{\partial s} = \sum_a \frac{\partial(\Omega_a)}{\partial t}\mathbf{d_a}. \tag{3.8}$$

This relationship implies that if $\partial\boldsymbol{\omega}/\partial s = 0$ over any segment of the filament, i.e. if the segment moves as a rigid body, then $\partial\Omega_a/\partial t = 0$ as well, i.e. the material curvatures and twist do not change with time.

Kinematics

We now wish to describe the kinematics of a single cross-sectional segment of infinitesimal thickness Δs, as depicted earlier in Figure 3.1. The segment is identified by its position along the centerline, $\mathbf{r}(s, t)$. The motion of the rigid segment is described by (i) its translational velocity $\mathbf{v}$, i.e. the rate at which $\mathbf{r}(s, t)$ changes with time and (ii) angular velocity, $\boldsymbol{\omega}$ of the cross-sectional plane about the centerline. The angular velocity describes the change in material orientations (Equation (3.7)) while the translational velocity is the rate of change of the segment's position vector:

$$\frac{\partial \mathbf{r}}{\partial t} = \mathbf{v}. \tag{3.9}$$

The inextensibility of the filament is achieved by ensuring that the tangent vector $\mathbf{d}_1$ is always of unit magnitude. How this is achieved numerically will be described in later sections.

Conservation Laws

Assuming negligible changes in density of the filament material throughout the body volume, conservation of mass implies that the cross-sectional area of the filament at any s must remain constant.

We now examine the forces and moments acting on each cross section. As shown in Figure 3.2, the following forces and moments are considered in this study:

- *hydrodynamic force* $\mathbf{f^h}$ and *moment* $\mathbf{m^h}$ per unit length of the segment, exerted on the external cylindrical surface of the segment by the surrounding fluid;
- *active force* $\mathbf{f^a}$ and *moment* $\mathbf{m^a}$ per unit length of the segment, exerted by protein motors on the internal cylindrical surfaces;
- *passive internal force* $\mathbf{F}$ and *moment* $\mathbf{M}$ that resist bending and twisting, acting on the cross-sectional planes bounding the segment; and
- *steric forces* $\mathbf{f^s}$ between different parts of the flagellum which prevent self-intersection.

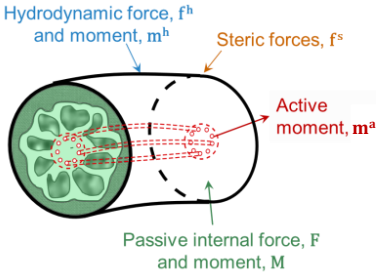

Figure 3.2: The control volume experiences external hydrodynamic forces and moments, internal active moments from protein motors and passive internal forces and moments that resist bending/twisting.

The active-force-generating components of the flagellum are the protein motors distributed along the length of the flagellum. The control volume consists only of the passive flagellar material and does not include the active protein motors, which exert stresses on internal surfaces of the flagellum that they are in contact with (depicted using red dotted lines in Figures 3.1 and 3.2). Since the volume occupied by the protein motors is infinitesimal, it is assumed that the exclusion of the protein motors does not significantly alter the material properties of the control volume. The protein motors are assumed to exert equal and opposite forces on the internal surfaces such that the net active force at each cross section, $\mathbf{f^a} = 0$. These active forces result in a net cross-sectional moment, $\mathbf{m^a}$.

The filament is assumed to be inertialess, i.e. net force and net moment are both equal to zero. Using notation as indicated on Figure 3.2, linear momentum balance is obtained as

$$\mathbf{f^h} + \mathbf{f^s} + \frac{\partial \mathbf{F}}{\partial s} = 0. \tag{3.10}$$

Similarly, the angular momentum conservation equation is:

$$\mathbf{m^h} + \mathbf{m^a} + \frac{\partial \mathbf{M}}{\partial s} + \mathbf{r} \times \mathbf{f^h} + \mathbf{r} \times \mathbf{f^s} + \frac{\partial (\mathbf{r} \times \mathbf{F})}{\partial s} = 0. \tag{3.11}$$

Substituting the linear momentum conservation equation (3.10) into the above equation and noting that $\partial \mathbf{r}/\partial s = \mathbf{d}_1$, we obtain:

$$\mathbf{m^h} + \mathbf{m^a} + \frac{\partial \mathbf{M}}{\partial s} + \mathbf{d}_1 \times \mathbf{F} = 0. \tag{3.12}$$

To understand the nature of the internal bending and twisting moments, it is instructive to consider the energy balance of the filament. A general energy balance for a control volume (CV) can be expressed as

Rate of change of energy within the CV	=	Rate of energy transport into CV	+	Rate of work done on CV	+	Rate of heat input into CV

For the filament being considered, energy changes within the control volume would include changes in kinetic energy, gravitational potential energy, elastic potential energy and thermal internal energy. Of these, kinetic energy changes can be assumed to be negligible due to lack of inertia. Gravitational effects are also negligible, and chemical reactions are not considered within the passive filament material, i.e. the control volume. This leaves elastic potential energy and thermal internal energy on the left hand side of the energy balance equation.

On the right-hand side, the first term describes energy transferred to the system through material inflow. This is zero since there is no exchange of material between the control volume and its surroundings. The last term on the right accounts for heat transfer between the filament and the surrounding fluid. The second term is the rate of work done on the control volume, which consists of the work done by

- *surface stresses* on the external, internal and cross-sectional surfaces of the segment. As discussed before, these consist of hydrodynamic stresses, passive internal stresses, active stresses and any others.
- *external forces* such as steric repulsion.

This can be expressed in the form of the energy balance equation below, where u represents thermal internal energy per unit length of the segment, e represents elastic potential per unit length of the segment and h_{in} represents heat input per unit length of the segment:

$$\frac{\partial(u+e)}{\partial t} = \mathbf{v}\cdot(\mathbf{f^h}+\mathbf{f^e}) + \boldsymbol{\omega}\cdot(\mathbf{m^h}+\mathbf{m^a}+\mathbf{m^e}) + \frac{\partial(\mathbf{v}\cdot\mathbf{F})}{\partial s} + \frac{\partial(\boldsymbol{\omega}\cdot\mathbf{M})}{\partial s} + h_{in}. \tag{3.13}$$

Considering linear and angular momentum balances (3.10) and (3.12), this can be rewritten as

$$\frac{\partial u}{\partial t} + \frac{\partial e}{\partial t} = \frac{\partial \boldsymbol{\omega}}{\partial s}\cdot\mathbf{M} \; + \; h_{in}. \tag{3.14}$$

The elastic and dissipative parts of the internal moment, $\mathbf{M^{el}}$ and $\mathbf{M^{di}}$ are now defined such that $\mathbf{M} = \mathbf{M^{el}} + \mathbf{M^{di}}$ and

$$\frac{\partial u}{\partial t} = \frac{\partial \boldsymbol{\omega}}{\partial s}\cdot\mathbf{M^{di}} \; + \; h_{in}, \tag{3.15}$$

$$\frac{\partial e}{\partial t} = \frac{\partial \boldsymbol{\omega}}{\partial s}\cdot\mathbf{M^{el}}. \tag{3.16}$$

While some studies suggest the presence of a dissipative internal moment (Nandagiri et al., 2021; Mondal et al., 2020), here the flagellum is assumed to be purely elastic, i.e. $\mathbf{M^{di}} = 0$ and $\mathbf{M} = \mathbf{M^{el}}$. Assuming that the internal energy solely depends on temperature, for an isothermal system $\partial u/\partial t = 0$, which means that $h_{in} = 0$.

Constitutive Model for Passive Internal Moment

Here onward, we drop the superscript for the elastic moment. From equations (3.16) and (3.8), the elastic moment must satisfy

$$\frac{\partial e}{\partial t} = \sum_j \frac{\partial \Omega_j}{\partial t}\ M_j,$$

where the subscripts represent the material directions. The simplest model that satisfies this relationship is a linear relation between the local moment components M_j and the corresponding curvature or twist, Ω_j:

$$M_j = K_j(s)\Omega_j, \tag{3.17}$$

where the elastic stiffness coefficients $K_j(s)$ are functions of s. This means that

$$\frac{\partial e}{\partial t} = \sum_j K_j \Omega_j \frac{\partial \Omega_j}{\partial t} = \frac{\partial}{\partial t} \sum_j \frac{1}{2} K_j \Omega_j^2, \tag{3.18}$$

or,

$$e = \sum_j \frac{1}{2} K_j \Omega_j^2. \tag{3.19}$$

For homogeneous filaments with constant cross-sectional areas, K_j do not vary with s (Coleman et al., 1993). To ensure that the lowest elastic energy state corresponds to a straight, untwisted rod, i.e. $\mathbf{\Omega} = \mathbf{0}$, we require that $K_j > 0$. Henceforth K_1 will be referred to as the 'twisting stiffness', and denoted as K_T. The other two stiffnesses are the 'bending stiffnesses', and will be denoted as K_B. For simplicity, K_T is chosen to be equal to K_B.

We now have a system of nine vector equations: linear and angular momentum conservation equations (3.10) and (3.12), kinematic equations (3.9) and (3.7) defining translational and angular velocities, and equations defining the material frame, (3.2)-(3.6). Another four vector equations are required to close this system of equations; these will take the form of constitutive relations for the hydrodynamic force and moment, active moment and steric forces.

Stokesian Hydrodynamics for Motion in Quiescent Newtonian Fluid

Assuming no-slip conditions on the surface of the filament, the linear and angular velocities of each cross section are related to the hydrodynamic

force and moment at every cross section as follows:

$$\begin{bmatrix}\mathbf{v}(s,t)\\ \boldsymbol{\omega}(s,t)\end{bmatrix} = \int_0^L \begin{bmatrix}\boldsymbol{\mathcal{M}}^{\mathrm{tt}}(s,s') & \boldsymbol{\mathcal{M}}^{\mathrm{tr}}(s,s')\\ \boldsymbol{\mathcal{M}}^{\mathrm{rt}}(s,s') & \boldsymbol{\mathcal{M}}^{\mathrm{rr}}(s,s')\end{bmatrix} \cdot \begin{bmatrix}\mathbf{f}^{\mathbf{h}}(s',t)\\ \mathbf{m}^{\mathbf{h}}(s',t)\end{bmatrix} ds', \quad (3.20)$$

where $\boldsymbol{\mathcal{M}}^{\mathrm{tt}}$, $\boldsymbol{\mathcal{M}}^{\mathrm{tr}}$, $\boldsymbol{\mathcal{M}}^{\mathrm{rt}}$ and $\boldsymbol{\mathcal{M}}^{\mathrm{rr}}$ are 3×3 hydrodynamic mobility matrices which depend only on the shape of the filament and the viscosity of the fluid. Here the superscripts 't' and 'r' denote the translational and rotational components respectively (Wajnryb et al., 2013). $\boldsymbol{\mathcal{M}}^{\mathrm{tt}}$ and $\boldsymbol{\mathcal{M}}^{\mathrm{tr}}$ relate the linear velocity to the hydrodynamic forces and hydrodynamic moments respectively, whereas $\boldsymbol{\mathcal{M}}^{\mathrm{rt}}$ and $\boldsymbol{\mathcal{M}}^{\mathrm{rr}}$ relate the angular velocity to the hydrodynamic forces and hydrodynamic moments respectively. The forms of the mobility matrices depend on the hydrodynamic model chosen.

In this study the Stokesian Dynamics tensors, which are also known as the Rotne-Prager-Yamakawa tensors, are used for motion in free space as well as near a plane wall (Durlofsky et al., 1987; Swan and Brady, 2007; Wajnryb et al., 2013). In this model, the cross-sectional segments of the filament are hydrodynamically treated as rigid spheres satisfying no-slip conditions at their surfaces, and pairwise long-range hydrodynamic interactions are accounted for (Durlofsky et al., 1987). Appendix 10.1 discusses how the corresponding mobility matrices are derived. The mobility matrices in free space are given as (Durlofsky et al., 1987; Wajnryb et al., 2013)

$$\boldsymbol{\mathcal{M}}_{ij}^{F,\mathrm{tt}} = \begin{cases}\dfrac{1}{8\pi\mu\, r}\left[\left(1+\dfrac{2\,a^2}{3\,r^2}\right)\mathbf{I}+\left(1-\dfrac{2\,a^2}{r^2}\right)\hat{\mathbf{x}}\hat{\mathbf{x}}\right] & , \quad i\neq j\,,\\ \dfrac{1}{6\pi\mu\, a}\mathbf{I} & , \quad i=j\,,\end{cases}$$

$$\boldsymbol{\mathcal{M}}_{ij}^{F,\mathrm{tr}} = \boldsymbol{\mathcal{M}}_{ij}^{F,\mathrm{rt}\ \dagger} = \begin{cases}\dfrac{1}{8\pi\mu r^2}\,\boldsymbol{\epsilon}\cdot\hat{\mathbf{x}} & , \quad i\neq j\,,\\ 0 & , \quad i=j\,,\end{cases}$$

$$\boldsymbol{\mathcal{M}}_{ij}^{F,\mathrm{rr}} = \begin{cases}\dfrac{1}{16\pi\mu r^3}\,(3\,\hat{\mathbf{x}}\,\hat{\mathbf{x}}-\mathbf{I}) & , \quad i\neq j\,,\\ \dfrac{1}{8\pi\mu a^3}\mathbf{I} & , \quad i=j,\end{cases}$$

where μ is the fluid viscosity, a is the radius of the sphere, $\mathbf{x}=\mathbf{r}_i-\mathbf{r}_j$ for two segments i and j with position vectors $\mathbf{r}_i$ and $\mathbf{r}_j$, $r=|\mathbf{x}|$, $\hat{\mathbf{x}}=\mathbf{x}/r$, $\mathbf{I}$ represents the identity tensor and $\boldsymbol{\epsilon}$ is the three-dimensional Levi-Civita symbol. Here the dagger symbol represents the matrix transpose. Sphere-sphere lubrication interactions are not included since we do not consider cases where they would become significant – in free space, lubrication effects are expected to become important only when distant parts of the flagellum move towards each other such that the gap between them becomes comparable to the filament radius (Lomholt and

Maxey, 2003).

From the above we can observe that when $i = j$, the mobility matrices take on the more well-known forms corresponding to the motion of an individual rigid sphere in free space:

$$\begin{aligned}\mathcal{M}_{ii}^{F,\mathrm{tt}} &= \frac{1}{6\pi\mu a}\mathbf{I},\\ \mathcal{M}_{ii}^{F,\mathrm{rr}} &= \frac{1}{8\pi\mu a^3}\mathbf{I},\\ \mathcal{M}_{ii}^{F,\mathrm{tr}} &= \mathcal{M}_{ii}^{F,\mathrm{rt}} = \mathbf{0}.\end{aligned}$$

The mobility matrices for motion near a wall have a more complicated form, owing to the inclusion of flows induced by the *image system* (Blake, 1971) of every sphere. For a sphere at a position (x, y, z) above a plane wall at $z = 0$, the image system consists of a set of flow singularities placed at $(x, y, -z)$ which act to cancel out the flow induced by the sphere at $z = 0$. The total flow hence vanishes at $z = 0$ and also decays to zero at infinity. The additional contributions to the mobility matrices arising from the image system are expressed as (Swan and Brady, 2007)

$$\boldsymbol{\mathcal{M}}_{ij}^{W,\mathrm{tt}} = \begin{cases} \dfrac{1}{6\pi\mu}\Bigg[-\dfrac{3}{4r_i}(\mathbf{I}+\hat{\mathbf{x}}_\mathbf{i}\hat{\mathbf{x}}_\mathbf{i}) + \dfrac{3h}{2r_i^2}(3\hat{x}_{i,z}\hat{\mathbf{x}}_\mathbf{i}\hat{\mathbf{x}}_\mathbf{i} - \hat{x}_{i,z}\mathbf{I} + \mathbf{e}_z\hat{\mathbf{x}}_\mathbf{i} + \hat{\mathbf{x}}_\mathbf{i}\mathbf{e}_z - 6\hat{x}_{i,z}^2\hat{\mathbf{x}}_\mathbf{i}\mathbf{e}_z) + \\ \quad \dfrac{3h^2}{2r_i^3}(\mathbf{I} - 3\hat{\mathbf{x}}_\mathbf{i}\hat{\mathbf{x}}_\mathbf{i} - 2\mathbf{e}_z\mathbf{e}_z + 6\hat{x}_{i,z}\hat{\mathbf{x}}_\mathbf{i}\mathbf{e}_z) + \dfrac{3a^2}{2r_i^3}(\hat{x}_{i,z}^2\mathbf{I} - 2\hat{x}_{i,z}^2\mathbf{e}_z\mathbf{e}_z - 2\hat{x}_{i,z}\hat{\mathbf{x}}_\mathbf{i}\mathbf{e}_z) - \\ \quad \dfrac{a^2}{2r_i^3}(\mathbf{I} - 3\hat{\mathbf{x}}_\mathbf{i}\hat{\mathbf{x}}_\mathbf{i}) - \dfrac{15a^2}{2r_i^3}(\hat{x}_{i,z}^2\hat{\mathbf{x}}_\mathbf{i}\hat{\mathbf{x}}_\mathbf{i} - 2\hat{x}_{i,z}^3\hat{\mathbf{x}}_\mathbf{i}\mathbf{e}_z) + \dfrac{a^4}{2r_i^5}(\mathbf{I} - 4\mathbf{e}_z\mathbf{e}_z) + \\ \quad \dfrac{35a^4}{2r_i^5}(\hat{x}_{i,z}^2\hat{\mathbf{x}}_\mathbf{i}\hat{\mathbf{x}}_\mathbf{i} - 2\hat{x}_{i,z}^3\hat{\mathbf{x}}_\mathbf{i}\mathbf{e}_z) - \dfrac{5a^4}{4r_i^5}(2\hat{\mathbf{x}}_\mathbf{i}\hat{\mathbf{x}}_\mathbf{i} + 4\hat{x}_{i,z}\mathbf{e}_z\hat{\mathbf{x}}_\mathbf{i} - 8\hat{x}_{i,z}\hat{\mathbf{x}}_\mathbf{i}\mathbf{e}_z + 2\hat{x}_{i,z}^2\mathbf{I} - 12\hat{x}_{i,z}^2\mathbf{e}_z\mathbf{e}_z)\Bigg] & , \quad i \neq j\,, \\ \dfrac{1}{6\pi\mu a}\left[\left(\dfrac{a^3}{8h^3} - \dfrac{9a}{16h} - \dfrac{a^5}{16h^5}\right)(\mathbf{I} + \mathbf{e}_z\mathbf{e}_z) + \dfrac{2a^3}{8h^3}\mathbf{e}_z\mathbf{e}_z\right] & , \quad i = j\,, \end{cases}$$

$$\boldsymbol{\mathcal{M}}_{ij}^{W,\mathrm{rt}} = \boldsymbol{\mathcal{M}}_{ij}^{W,\mathrm{tr}\ \dagger} = \begin{cases} \dfrac{1}{4\pi\mu}\Bigg[\dfrac{h}{r_i^3}(6\hat{x}_{i,z}\mathbf{e}_z\times\hat{\mathbf{x}}_\mathbf{i}\mathbf{e}_z - 3\mathbf{e}_z\times\hat{\mathbf{x}}_\mathbf{i}\hat{\mathbf{x}}_\mathbf{i} - \boldsymbol{\epsilon}\cdot\mathbf{e}_z) + \dfrac{1}{2r_i^2}(\boldsymbol{\epsilon}\cdot\hat{\mathbf{x}}_\mathbf{i}) - \\ \quad \dfrac{a^2}{r_i^4}(5\hat{x}_{i,z}\mathbf{e}_z\times\hat{\mathbf{x}}_\mathbf{i}\hat{\mathbf{x}}_\mathbf{i} - 10\hat{x}_{i,z}^2\mathbf{e}_z\times\hat{\mathbf{x}}_\mathbf{i}\mathbf{e}_z + \hat{x}_{i,z}\boldsymbol{\epsilon}\cdot\mathbf{e}_z + \mathbf{e}_z\times\hat{\mathbf{x}}_\mathbf{i}\mathbf{e}_z)\Bigg] & , \quad i \neq j\,, \\ \dfrac{1}{64\pi\mu}\left(\dfrac{a^2}{h^2}\boldsymbol{\epsilon}\cdot\mathbf{e}_z\right) & , \quad i = j\,, \end{cases}$$

$$\boldsymbol{\mathcal{M}}_{ij}^{W,\mathrm{rr}} = \begin{cases} \dfrac{1}{16\pi\mu r_i^3}\left(\mathbf{I} - 3\hat{\mathbf{x}}_\mathbf{i}\hat{\mathbf{x}}_\mathbf{i} + 6(\mathbf{e}_z\times\hat{\mathbf{x}}_\mathbf{i})(\mathbf{e}_z\times\hat{\mathbf{x}}_\mathbf{i}) + 6\hat{x}_{i,z}\mathbf{e}_z\hat{\mathbf{x}}_\mathbf{i} - 6\hat{x}_{i,z}^2\mathbf{I}\right) & , \quad i \neq j\,, \\ \dfrac{1}{128\pi\mu h^3}(3\mathbf{e}_z\mathbf{e}_z - 5\mathbf{I}) & , \quad i = j, \end{cases}$$

so that $\boldsymbol{\mathcal{M}}_{ij}^{\mathrm{xx}} = \boldsymbol{\mathcal{M}}_{ij}^{F,\mathrm{xx}} + \boldsymbol{\mathcal{M}}_{ij}^{W,\mathrm{xx}}$. Here h is the height of the i-th particle above the wall, $\mathbf{x_i} = \mathbf{r_i} - \mathbf{r_j}^{im}$ for a segment i and the image of segment j

with position vectors $\mathbf{r_i}$ and $\mathbf{r_j}^{im}$, $r_i = |\mathbf{x_i}|$, $\hat{\mathbf{x}}_\mathbf{i} = \mathbf{x_i}/r_i$, $\mathbf{e}_z$ represents the unit vector in the z direction and $\hat{x}_{i,z}$ is the z-component of $\hat{\mathbf{x}}_\mathbf{i}$. Here the force multipole expansion is truncated at the force-torque (F-T) level, and hence this is only a far-field approximation. The effect of including the next term (corresponding to the stresslet) has been investigated in an example problem given in Appendix 10.1. The example, presented in Swan and Brady (2007), calculates the rotation rate of a doublet of spheres at varying distances from a wall and for different particle separation distances. The inclusion of the stresslet did not provide a noticeable improvement over the F-T version, and hence the mobility matrices have been limited to the F-T level in all simulations.

Model for the Active Moment

The simplest models for the active moment provided by protein motors involve applying a travelling wave of active moment propagating along the length of the flagellum (see Chapter 2), which would result in a wave-like beating of the filament. However, using an expression such as $\mathbf{m^a} = \mathbf{A}\cos(\mathrm{k^a s} - \omega^a \mathrm{t})$ as in Hall-McNair et al. (2019) and Walker et al. (2020a) would result in a net torque being exerted on the filament. The integral of the angular momentum balance (3.12) over the entire filament gives

$$\int_0^L \left(\mathbf{m^h} + \mathbf{d}_1 \times \mathbf{F}\right) + \left(\mathbf{m^a} + \frac{\partial \mathbf{M}}{\partial s}\right) ds = 0. \tag{3.21}$$

For a free-swimming filament, $\mathbf{F}|_{s=0} = \mathbf{F}|_{s=L} = 0$. Therefore,

$$\int_0^L \mathbf{d}_1 \times \mathbf{F}\, ds \;=\; \int_0^L \frac{\partial}{\partial s}\left(\mathbf{r} \times \mathbf{F}\right) ds - \int_0^L \mathbf{r} \times \frac{\partial \mathbf{F}}{\partial s} ds \;=\; \int_0^L \mathbf{r} \times \mathbf{f^h}\, ds,$$

where the linear momentum balance (3.10) has been used in the second step. Hence, the first bracketed term in (3.21) corresponds to the net hydrodynamic moment on the filament, which must be equal to zero. This leaves us with

$$\int_0^L \left(\mathbf{m^a} + \frac{\partial \mathbf{M}}{\partial s}\right) ds = 0.$$

We now define $\mathbf{M^a}$ such that $\mathbf{m^a} = \partial \mathbf{M^a}/\partial s$. Then,

$$\int_0^L \frac{\partial \left(\mathbf{M^a} + \mathbf{M}\right)}{\partial s} ds = 0.$$

This reduces the problem of ensuring torque-free conditions to one of setting the boundary conditions $\left(\mathbf{M^a} + \mathbf{M}\right)|_{s=L} - \left(\mathbf{M^a} + \mathbf{M}\right)|_{s=0} = 0$.

Now, to determine an expression for $\mathbf{M^a}$ that would result in wave-like beating, we express $\mathbf{M^a}$ in terms of an 'active preferred curvature' $\mathbf{\Omega^a}$:

$$\mathbf{M^a} = -\mathbf{K} \cdot \mathbf{\Omega^a},$$

so that

$$\mathbf{M} + \mathbf{M^a} = \mathbf{K} \cdot (\mathbf{\Omega} - \mathbf{\Omega^a}),$$

where $\mathbf{K}$ is the diagonal matrix of elastic stiffness coefficients. From studies that use a time-varying preferred curvature to drive the filament (Elgeti et al., 2010; Olson et al., 2013; Delmotte et al., 2015) we know that a travelling wave in the preferred curvature can result in the desired sinusoidal beating. Hence, the following form is chosen for the active moment:

$$\mathbf{M^a} = M_0 \cos(\mathrm{k^a s} - \omega^{\mathrm{a}} \mathrm{t})\mathbf{d}_3. \tag{3.22}$$

The driving moment is only applied along one material direction, $\mathbf{d}_3$, which would result in a wave of active bending moments along the binormal material direction of the filament. The effect of this uni-directional active bending moment would be to induce locally-planar bends at each cross section. However, we note that the orientations of the cross sections are not predetermined, and can evolve according to the emergent shape of the filament. Hence, the nature of the emergent beating cannot be determined based on the active driving alone.

This choice of active driving is an effort to model, at an abstract level, the action of the protein motors in the axoneme as captured in the recent experimental study of Lin and Nicastro (2018). Reproduced in Figure 3.3 is part of Figure 3 from Lin and Nicastro (2018), showing the activity states of the protein motors at three different parts of the flagellum corresponding to a principal bend (top panel), straight region (middle panel) and reverse bend (bottom panel). According to the interpretation in their description of a 'switch-inhibition' mechanism, the blue colour represents active motors while red represents inhibited motors which do not generate any force. The activity patterns seen in the principal and reverse bend regions can be expected to cause no net force but a net moment about the direction along the central pair axis, i.e. perpendicular to the white arrows. Meanwhile in the straight region, when all motors are active, there is no net force or torque. For a detailed discussion the reader is referred to Lindemann and Lesich (2021).

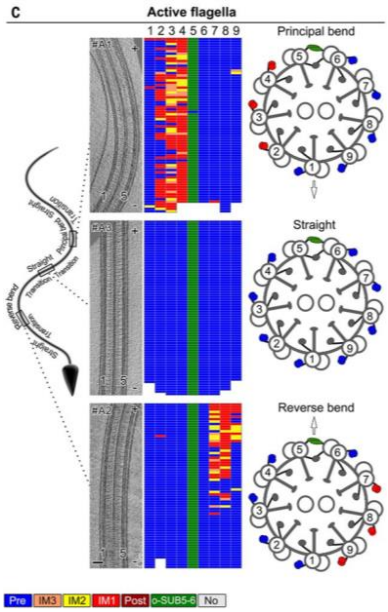

Figure 3.3: Pattern of protein motor activity (outer dynein arms) at three different points along the active flagellum of sea urchin sperm. The colour legend indicates the conformational state of the dynein motor: blue represents pre-power-stroke, red, orange and yellow represent intermediate states, and green represents the cross-link between microtubules 5 and 6. Figure reproduced from Lin and Nicastro (2018) with permission.

This is hence interpreted as a distribution along the length of the flagellum of pure bending moments about a single material direction $\mathbf{d}_3$. This material direction may be physically interpreted as the direction along the central pair in the flagellum.

Model for Steric Repulsion

The steric repulsion between segments is modelled following Schoeller et al. (2021). The force on segment n due to segment m becomes non-zero only when they are within 1.1 times their centre-to-centre distance, and takes the form:

$$\mathbf{F^s} = G\left(\frac{4a^2\chi^2 - r^2}{4a^2(\chi^2-1)}\right)^4 \frac{\mathbf{x}}{2a}, \tag{3.23}$$

where $\mathbf{x} = \mathbf{r_m} - \mathbf{r_n}$ for two segments m and n with position vectors $\mathbf{r_m}$ and $\mathbf{r_n}$, $r = |\mathbf{x}|$, a is the segment radius, and $\chi = 1.1$ sets the required separation distance. The reference force G is set to be large, i.e. 100 times the force scale of the system.

3.2 Dimensionless Quantities and Boundary Conditions

The filament is subject to free-end boundary conditions on both ends: $\mathbf{F}|_{s=L} = \mathbf{F}|_{s=0} = 0$, and $(\mathbf{M^a} + \mathbf{M})\,|_{s=L} = (\mathbf{M^a} + \mathbf{M})\,|_{s=0} = 0$.

The system is non-dimensionalised by selecting a time, length and force scale to determine the dimensionless quantities that govern the system. The inverse of the frequency of the active moment wave, ω_a^{-1}, is used as the time scale. The length scale is the filament length, L and the force scale is chosen to be K_B/L^2, where K_B is the elastic bending stiffness. The following six dimensionless quantities are obtained, which will be used in discussions in the following chapters:

1. Dimensionless frequency of the active driving, also known as the Swimming number (Hall-McNair et al., 2019), which represents the ratio of the time scale of the elastohydrodynamic response to the time-scale of the active driving:

$$S = L\left(\frac{\mu\omega^a}{K_B}\right)^{1/4}.$$

2. Dimensionless amplitude of the active driving:

$$A = \frac{M_0 L}{K_B}.$$

3. Dimensionless wavenumber of the active driving,

$$k = k^a L.$$

4. Dimensionless filament radius, a/L.

5. Ratio of bending and twisting stiffnesses, K_T/K_B.

6. Dimensionless steric force, GL^2/K_B.

3.3 Numerical Method

Computation-friendly Kinematic Equations

The problem can be summarised as a set of equations for a filament centerline discretized into N segments. We first have the kinematic equations (3.9) and (3.7) which can be expressed in the following forms:

$$\frac{\mathrm{d}\mathbf{r_n}}{\mathrm{d}t} = \mathbf{v_n}; \tag{3.24}$$

$$\frac{\mathrm{d}\mathbf{d_{1,n}}}{\mathrm{d}t} = \boldsymbol{\omega_n} \times \mathbf{d_{1,n}}; \tag{3.25}$$

$$\frac{\mathrm{d}\mathbf{d_{2,n}}}{\mathrm{d}t} = \boldsymbol{\omega_n} \times \mathbf{d_{2,n}}. \tag{3.26}$$

We know that

$$\mathbf{d_{3,n}} = \mathbf{d_{1,n}} \times \mathbf{d_{2,n}}.$$

We also have the filament inextensibility constraint (3.2),

$$\frac{\mathrm{d}\mathbf{r_n}}{\mathrm{d}s} = \mathbf{d_{1,n}}.$$

Here the subscript n denotes the segment index. As discussed, the velocity and angular velocity can be expressed in terms of the hydrodynamic forces and moments on each segment, using Equation (3.20). These are in turn expressed in terms of all other forces and moments acting on the segment using the force and moment balances (3.10) and (3.12). The resulting system of equations is nonlinear and also numerically stiff, because of the presence of the passive internal force $\mathbf{F}$ which acts like a tension enforcing the inextensibility and unshearability conditions.

The numerical solution of the system is based on the algorithm proposed by Schoeller et al. (2021) for passive inertialess Kirchhoff rods suspended in fluid. The algorithm, which has been specially designed for computational efficiency, uses the quasi-Newton Broyden's method along with implicit second-order backward difference time-stepping. This would mean that for the above system of equations, at every time step, the unknowns would be $\mathbf{r_n}, \mathbf{d_{1,n}}, \mathbf{d_{2,n}}$ and the passive internal force $\mathbf{F_n}$ at every segment. The problem of updating the unit material frame vectors $\mathbf{d_{1,n}}$ and $\mathbf{d_{2,n}}$ and ensuring that they remain unit is handled by representing the material frame at every time step as a rotation of the global xyz frame about some unknown angle and axis. These rotations are defined using unit quaternions $\tilde{\mathbf{q}} = q_0 + q_1\mathbf{i} + q_2\mathbf{j} + q_3\mathbf{k}$, such that

$$\mathbf{d}_1 = \mathbf{R}(\tilde{\mathbf{q}})\ \mathbf{e_x}, \tag{3.27}$$

$$\mathbf{d}_2 = \mathbf{R}(\tilde{\mathbf{q}})\ \mathbf{e_y}, \tag{3.28}$$

$$\mathbf{d}_3 = \mathbf{R}(\tilde{\mathbf{q}})\ \mathbf{e_z}, \tag{3.29}$$

where $\mathbf{e_x}$, $\mathbf{e_y}$ and $\mathbf{e_z}$ are the x, y and z unit vectors and $\mathbf{R}(\tilde{\mathbf{q}})$ is a quaternion rotation matrix (see Appendix 10.2 for a brief introduction to quaternions and Lie algebra). The use of a quaternion rotation matrix enables us to address the challenge of ensuring that the magnitude of the rotated vector does not change, i.e. we can be ensured that material frame vectors would remain unit if we rotate them by a *unit quaternion*. The kinematic equations are now rewritten as (Schoeller et al., 2021; Boyle, 2017)

$$\frac{\mathrm{d}\mathbf{r_n}}{\mathrm{d}t} = \mathbf{v_n}, \tag{3.30}$$

$$\frac{\mathrm{d}\tilde{\mathbf{q}}_\mathbf{n}}{\mathrm{d}t} = \frac{1}{2}(0, \boldsymbol{\omega_n}) \cdot \tilde{\mathbf{q}}_\mathbf{n}, \tag{3.31}$$

where $(0, \boldsymbol{\omega_n})$ is the representation of $\boldsymbol{\omega_n}$ in quaternion notation, and the quaternion product is defined in Appendix 10.2. The problem of updating the unit vectors has now turned into a problem of updating the unit quaternions. This is addressed by noting that unit quaternions form a Lie group whose Lie algebra consists of vectors in $\mathbb{R}^3$ (with a Lie bracket corresponding to twice of the vector cross product). These Lie algebra elements are denoted as $\hat{\mathbf{u}} = u_1\mathbf{i} + u_2\mathbf{j} + u_3\mathbf{k}$, where $\mathbf{i}$, $\mathbf{j}$ and $\mathbf{k}$ are complex. The unit quaternions at every time step are updated using a geometric multi-step method as (Schoeller et al., 2021):

$$\tilde{\mathbf{q}}_\mathbf{n}(t + \Delta t) = \exp(\hat{\mathbf{u}}_\mathbf{n}(t + \Delta t)) \cdot \tilde{\mathbf{q}}_\mathbf{n}(t), \tag{3.32}$$

with the exponential map defined as

$$\exp(\hat{\mathbf{u}}) = \left(\cos\left(\frac{||\hat{\mathbf{u}}||}{2}\right),\ \sin\left(\frac{||\hat{\mathbf{u}}||}{2}\right)\frac{\hat{\mathbf{u}}}{||\hat{\mathbf{u}}||}\right).$$

Here $||\hat{\mathbf{u}}||$ denotes the norm of $\hat{\mathbf{u}}$. The kinematic equation (3.31) is now replaced with the equation below, which instead updates $\hat{\mathbf{u}}$:

$$\frac{\mathrm{d}\hat{\mathbf{u}}_\mathbf{n}}{\mathrm{d}t} = \mathrm{dexp}^{-1}_{\hat{\mathrm{u}}}(\boldsymbol{\omega_n}), \tag{3.33}$$

with $\hat{\mathbf{u}}(t_0) = 0$. Here, the differential exponent operator dexp^{-1} is defined as (Schoeller et al., 2021):

$$\mathrm{dexp}^{-1}_{\hat{u}}(\boldsymbol{\omega}) = \boldsymbol{\omega} - \frac{1}{2}\hat{\mathbf{u}} \times \boldsymbol{\omega} - \frac{1}{2||\hat{\mathbf{u}}||^2}\left[||\hat{\mathbf{u}}||\cot\left(\frac{||\hat{\mathbf{u}}||}{2}\right) - 2\right]\hat{\mathbf{u}} \times (\hat{\mathbf{u}} \times \boldsymbol{\omega}).$$

Discrete Form of Kinematic Equations

We now have the final kinematic equations (3.30) and (3.33), which can be expressed in discrete form using a second-order backward difference in time as follows (Schoeller et al., 2021):

$$\mathbf{r_n^{t+1}} - \frac{4}{3}\mathbf{r_n^t} + \frac{1}{3}\mathbf{r_n^{t-1}} - \frac{2\Delta t}{3}\mathbf{v_n^{t+1}} = 0 \tag{3.34}$$

$$\hat{\mathbf{u}}_\mathbf{n}^{\mathbf{t+1}} - \frac{1}{3}\hat{\mathbf{u}}_\mathbf{n}^{\mathbf{t}} - \frac{2\Delta t}{3}\mathrm{dexp}^{-1}_{\hat{u}_n^{t+1}}(\boldsymbol{\omega}_\mathbf{n}^{\mathbf{t+1}}) = 0 \tag{3.35}$$

We also have the kinematic constraint (3.2) expressed as shown below, where ΔL is the distance between the centres of segments n and $n+1$:

$$\mathbf{r}_{\mathbf{n+1}}^{\mathbf{t+1}} - \mathbf{r}_{\mathbf{n}}^{\mathbf{t+1}} - \frac{\Delta L}{2}(\mathbf{d}_{\mathbf{1,n}}^{\mathbf{t+1}} + \mathbf{d}_{\mathbf{1,n+1}}^{\mathbf{t+1}}) \tag{3.36}$$

From the above equations, for a total of N segments, the unknowns consist of all $\mathbf{r}_{\mathbf{n}}^{\mathbf{t+1}}$ (3N unknowns), $\hat{\mathbf{u}}_{\mathbf{n}}^{\mathbf{t+1}}$ (3N unknowns), and passive internal forces at the interfaces between each segment, $\mathbf{F}_{\mathbf{n+\frac{1}{2}}}^{\mathbf{t+1}}$ (3N–3 unknowns). In order to reduce the number of unknowns, (3.36) is rewritten in the following form, such that the positions of all other segments depend only on that of the first segment and all tangents $\mathbf{d}_{\mathbf{1,n}}$. The tangents themselves are not additional unknowns – they can be determined from the Lie algebra elements $\hat{\mathbf{u}}_{\mathbf{n}}$.

$$\mathbf{r}_{\mathbf{n}}^{\mathbf{t+1}} = \mathbf{r}_{\mathbf{1}}^{\mathbf{t+1}} + \frac{\Delta L}{2}\sum_{m=2}^{n}(\mathbf{d}_{\mathbf{1,m-1}}^{\mathbf{t+1}} + \mathbf{d}_{\mathbf{1,m}}^{\mathbf{t+1}}) \tag{3.37}$$

We now have the discrete kinematic equations in their final forms below, with 6N unknowns consisting of $\mathbf{r}_{\mathbf{1}}^{\mathbf{t+1}}$ (3 unknowns), $\mathbf{u}_{\mathbf{n}}^{\mathbf{t+1}}$ (3N unknowns) and $\mathbf{F}_{\mathbf{n+\frac{1}{2}}}^{\mathbf{t+1}}$ (3N–3 unknowns).

$$\mathbf{r}_{\mathbf{1}}^{\mathbf{t+1}} - \frac{4}{3}\mathbf{r}_{\mathbf{1}}^{\mathbf{t}} + \frac{1}{3}\mathbf{r}_{\mathbf{1}}^{\mathbf{t-1}} - \frac{2\Delta t}{3}\mathbf{v}_{\mathbf{1}}^{\mathbf{t+1}} = 0 \tag{3.38}$$

$$\mathbf{u}_{\mathbf{n}}^{\mathbf{t+1}} - \frac{1}{3}\mathbf{u}_{\mathbf{n}}^{\mathbf{t}} - \frac{2\Delta t}{3}\mathrm{dexp}^{-1}{}_{u_n^{t+1}}(\boldsymbol{\omega}_{\mathbf{n}}^{\mathbf{t+1}}) = 0 \tag{3.39}$$

$$\mathbf{r}_{\mathbf{1}}^{\mathbf{t+1}} + \frac{\Delta L}{2}\sum\nolimits_{m=2}^{n}(\mathbf{d}_{\mathbf{1,m-1}}^{\mathbf{t+1}} + \mathbf{d}_{\mathbf{1,m}}^{\mathbf{t+1}}) - \frac{4}{3}\mathbf{r}_{\mathbf{n}}^{\mathbf{t}} + \frac{1}{3}\mathbf{r}_{\mathbf{n}}^{\mathbf{t-1}} - \frac{2\Delta t}{3}\mathbf{v}_{\mathbf{n}}^{\mathbf{t+1}} = 0 \tag{3.40}$$

Solving the Equations

We may express the above system of equations as $\mathbf{f}(\mathbf{X}) = 0$, where $\mathbf{X}$ is the vector of 6N variables noted above. The system of equations is solved following the algorithm given in Schoeller et al. (2021), which is summarised in Figure 3.4. Known at time t are the initial segment positions, $\mathbf{r}_{\mathbf{n}}^{\mathbf{t}}$, quaternions $\tilde{\mathbf{q}}_{\mathbf{n}}^{\mathbf{t}}$ and the Lie algebra elements, $\mathbf{u}_{\mathbf{n}}^{\mathbf{t}}$ holding information about the orientation of material frame vectors at each segment n. In all of the simulations presented in this work the initial shape of the filament is a straight line, i.e. all quaternions are set to $(1,0,0,0)$ and Lie algebra elements are set to $(0,0,0)$. The filament has N=50 segments of length $\Delta L = 2a = 0.02$ and radius $a = 0.01$, which results in a total length of $L = 1$. Fluid viscosity μ and elastic stiffness coefficients K_B and K_T are set to 1. Parameters of the active moment wave are then defined based on input values of the dimensionless variables S, A and k defined before.

Now, the solutions at the next time step $t+1$ are guessed for the first segment position $\mathbf{r}_{\mathbf{1}}^{\mathbf{t+1}}$, Lie algebra elements $\mathbf{u}_{\mathbf{n}}^{\mathbf{t+1}}$ as well as the passive internal force $\mathbf{F}_{\mathbf{n}}^{\mathbf{t+1}}$. Time step size is chosen to be 10 times smaller

than the smallest timescale of the system, which for all parameter values corresponds to $\mu(\Delta L)^4/K_B$. The guess values of $\mathbf{u_n^{t+1}}$ are used to calculate quaternions, $\tilde{\mathbf{q}}_\mathbf{n}^{\mathbf{t+1}}$ and subsequently the material frame vectors, $\mathbf{d_{1,n}^{t+1}}, \mathbf{d_{2,n}^{t+1}}, \mathbf{d_{3,n}^{t+1}}$ using equations (3.32) and (3.27). The remaining segment positions $\mathbf{r_n^{t+1}}$ can now be calculated from the guess value of $\mathbf{r_1^{t+1}}$ and calculated $\mathbf{d_{1,n}^{t+1}}$, using equation (3.37).

Next, the material frame vectors calculated at time $t+1$ are used to find the passive internal moment $\mathbf{M_n^{t+1}}$ using equation (3.17). Active moments, $\mathbf{M_n^{a,t+1}}$ and any external forces and moments are also calculated. These are substituted into the force and moment balances (3.10) and (3.12) to find the hydrodynamic forces $\mathbf{f_n^{h,t+1}}$ and moments $\mathbf{m_n^{h,t+1}}$. These are subsequently used to find the segments' translational velocities $\mathbf{v_n^{t+1}}$ and angular velocities $\boldsymbol{\omega}_\mathbf{n}^{\mathbf{t+1}}$ through the hydrodynamic relations (3.20).

These velocity values are now substituted into the kinematic equations (10.14) and (10.15), and check whether the error is within the desired tolerance of 10^{-6}. If it is, then this solution is accepted for time $t+1$ and the same procedure is repeated for the next time step. If the error is too large, the guesses for $\mathbf{r_1^{t+1}}$, $\hat{\mathbf{u}}_\mathbf{n}^{\mathbf{t+1}}$ and $\mathbf{F_n^{t+1}}$ are updated iteratively based on *Bad Broyden's method*, as follows.

First, an approximate initial Jacobian matrix $\mathbf{J}$ is calculated for the system as detailed in (Schoeller et al., 2021), and its inverse $\mathbf{J^{-1}}$ computed. The form of the approximate Jacobian for this system is provided in Appendix 10.3. The new set of guesses $\mathbf{X_k}$ at iteration k is obtained by adding to the previous guess $\mathbf{X_{k-1}}$ an increment ΔX_k, defined as

$$\mathbf{\Delta X_k} = -[\mathbf{J^{-1}} + \sum_{i=1}^{k} \mathbf{C_i D_i^\dagger}]\ f(\mathbf{X_k}), \tag{3.41}$$

where the matrices $\mathbf{C}$ and $\mathbf{D}$ are calculated as:

$$\begin{aligned}
\mathbf{C_k} &= -[\mathbf{J^{-1}} + \sum_{i=1}^{k-1} \mathbf{C_i D_i^\dagger}]\ \frac{f(\mathbf{X_k})}{||f(\mathbf{X_k}) - f(\mathbf{X_{k-1}})||}; \\
\mathbf{D_k} &= \frac{(f(\mathbf{X_k}) - f(\mathbf{X_{k-1}}))}{||f(\mathbf{X_k}) - f(\mathbf{X_{k-1}})||}.
\end{aligned} \tag{3.42}$$

The main advantage of Bad Broyden's method is that the Jacobian of the system is not calculated and inverted at every iteration – only an approximate explicit Jacobian (which has a known form) is calculated at the first iteration of each timestep and inverted, and its *inverse* is directly updated at each iteration. Schoeller et al. (2021) have also explored the use of Good Broyden's method, where at each iteration the approximate Jacobian is updated and then inverted. They find that Bad

Broyden's method is not only more computationally efficient, but also more robust for systems of passive filaments in viscous suspensions.

Simulations are allowed to run for $0.5 - 1$ viscoelastic timescales, defined as $\mu L^4/K_B$. The first $50-100$ beat cycles are discarded to allow the filament to reach a 'stable' beat pattern, after which data is recorded at the resolution of the smallest timescale of the system, $\mu(\Delta L)^4/K_B$. The implementation of this algorithm is based on the MATLAB code provided in Schoeller et al. (2021) for passive elastic filaments, which has been modified for the current model in the following ways:

- The inclusion of the active driving term in the system of equations, which also requires modifications to the approximate Jacobian.
- The modification of hydrodynamic mobility matrices to include near-wall hydrodynamic interaction terms for simulations in Chapter 7.
- The replacement of Stokesian Dynamics mobility matrices with expressions for Resistive Force Theory (as described in Chapter 5) for simulations in Chapter 5. This also requires modifications to the approximate Jacobian.
- Overall code modifications to enable the automatic generation of a Matlab Executable (MEX) file using the Matlab Coder app. The app automatically generates C or C++ code from Matlab code and generates a MEX function. The use of a MEX function significantly reduces computational time.

The modified code was tested in two ways – first by inputting a constant $\mathbf{M^a} = A\ \mathbf{d}_3$ for a filament with $K_B = 1$ and $L = 1$ (which is equivalent to a static preferred curvature of $-A$ at all s) and checking that the filament attains the preferred curvature. The second test checks the implementation of the wall Stokesian Dynamics tensors through two examples; one is described in Chapter 7 and the other is provided in Appendix 10.1. The modified code is available for download (Veeraragavan, 2023).

3.4 Analysing Flagellar Waveforms

Throughout this work we will need to analyse and compare flagellar beat patterns obtained from simulations as well as those observed in experiments. In other words, we would like to study the shape of the centerline without considering the effects of global translation and rotation. One way to do this would be to look at the Darboux curvature function $\mathbf{\Omega}(s,t)$ defined earlier in (3.6), which can be easily computed from simulation results. Experimental studies (Gong et al., 2021; Powar

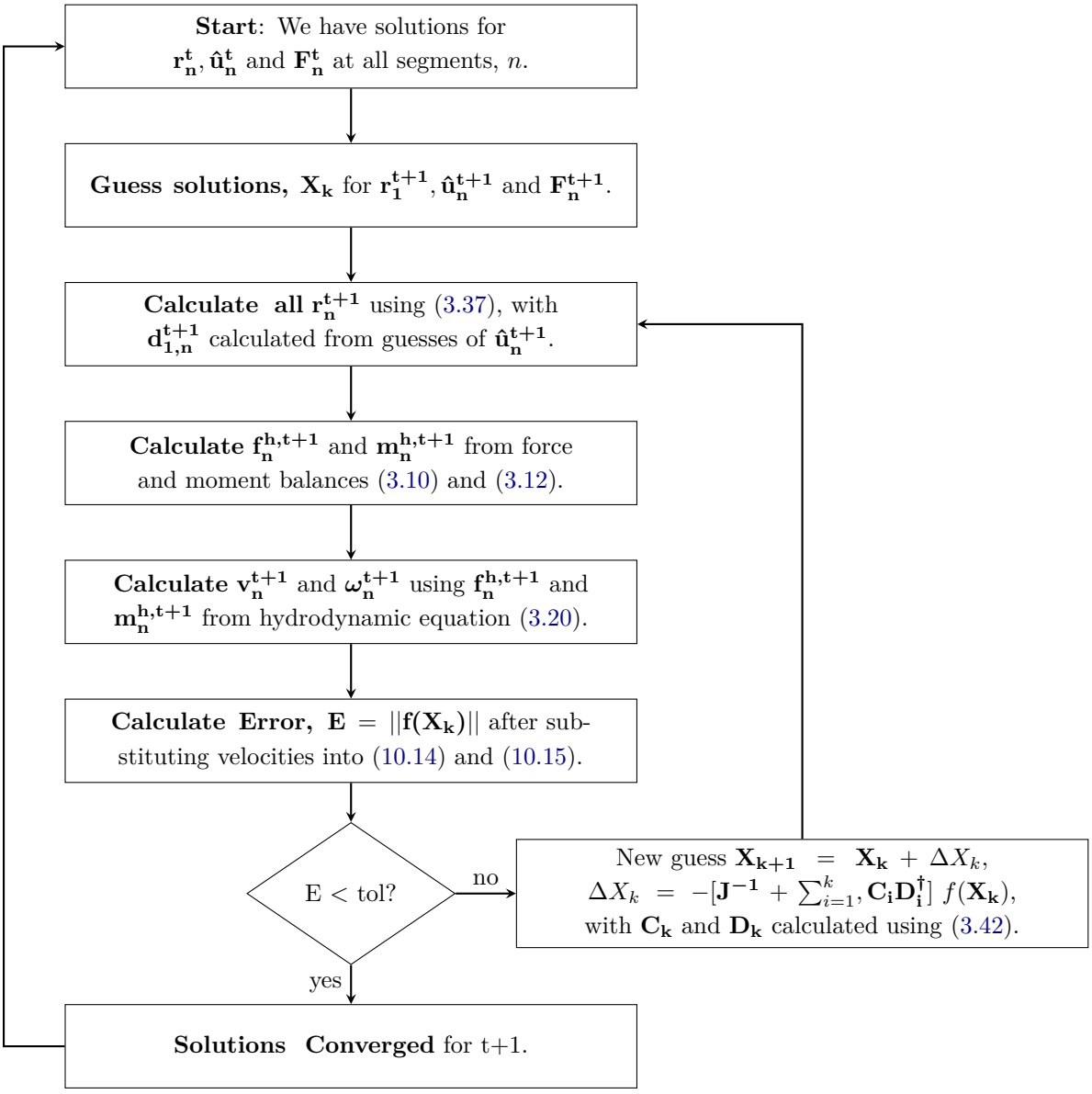

Figure 3.4: Overall algorithm based on bad Broyden's method to solve the system of equations to obtain positions and orientations of all filament segments at each time step.

et al., 2022) more commonly use the Frenet curvature, $\kappa(s,t)$ and torsion, $\tau(s,t)$ which define only the shape of the centerline and do not consider the orientation of the flagellar material:

$$\kappa = \frac{\partial \mathbf{t}}{\partial s} \cdot \mathbf{n}, \tag{3.43}$$

$$\tau = -\frac{\partial \mathbf{b}}{\partial s} \cdot \mathbf{n}, \tag{3.44}$$

where $\mathbf{t} = \mathbf{d}_1$ is the centerline tangent as defined in (3.2), and $\mathbf{n}$ and $\mathbf{b}$ are the normal and binormal vectors defined as

$$\mathbf{n} = \frac{\frac{\partial \mathbf{t}}{\partial s}}{||\frac{\partial \mathbf{t}}{\partial s}||}, \tag{3.45}$$

$$\mathbf{b} = \mathbf{t} \times \mathbf{n}. \tag{3.46}$$

The curvature describes how 'curved' the centerline is at each point, while the torsion is a measure of the degree to which it shifts out of plane. This system provides a simpler approach to understanding three-dimensional flagellar shapes and is sufficient for our purposes.

The curvature and torsion functions are now decomposed into spatially-dependent modes $\kappa_i'(s)$ and $\tau_i'(s)$ and their respective time-dependent coefficients $B_{\kappa,i}(t)$ and $B_{\tau,i}(t)$ using Proper Orthogonal Decomposition (POD), such that

$$\kappa(s,t) = \kappa_0(s) + \sum_{i=1}^{N} B_{\kappa,i}(t)\kappa_i'(s),$$

$$\tau(s,t) = \tau_0(s) + \sum_{i=1}^{N} B_{\tau,i}(t)\tau_i'(s),$$

where $\kappa_0(s)$ and $\tau_0(s)$ are the time-averaged curvature and torsion distributions, respectively, and N is the number of discrete spatial points. POD, otherwise known as Principal Component Analysis (PCA), has been used in many recent experimental studies to quantitatively analyse flagellar beats (Werner et al., 2014; Nandagiri et al., 2021; Guasto et al., 2020). The main advantage of POD over other techniques (such as Fourier decomposition) is that it generates spatial functions which capture the most variance from the least number of modes (Weiss, 2019). The process involves the following steps (Weiss, 2019).

First, the time-average is subtracted to obtain the matrix $\bar{\boldsymbol{\kappa}} = \kappa(s,t) - \kappa_0(s)$, whose rows correspond to time points and columns correspond to spatial points. The covariance of $\bar{\boldsymbol{\kappa}}$ is then calculated as follows, for M time-points:

$$\mathbf{C} = \frac{1}{M-1}\bar{\boldsymbol{\kappa}}^{\dagger}\bar{\boldsymbol{\kappa}}.$$

Then, $\mathbf{C}$ is diagonalised as $\mathbf{C} = \boldsymbol{\Phi}\boldsymbol{\Lambda}\boldsymbol{\Phi}^{\dagger}$ to obtain its eigenvectors $\boldsymbol{\Phi}$ which, when arranged according to the eigenvalues, are the desired shape modes $\kappa_i'(s)$. The shape coefficients are obtained (after arranging the eigenvectors) as

$$\mathbf{B}_{\boldsymbol{\kappa}} = \bar{\boldsymbol{\kappa}}\boldsymbol{\Phi}^{\dagger}.$$

In general, for most of the beat patterns obtained this study, the first two modes capture over 90% of the variance in curvature, but a higher number of modes may be required for torsion depending on the type of beat pattern. Our discussions in the subsequent chapters are hence limited to only the first two spatial modes and time-dependent coefficients of the curvature functions.

4
Effect of Fluid Viscosity on Beat Patterns in Bulk Fluid

4.1 Introduction

This chapter addresses the first objective of this study, which is to explore the mechanisms behind flagellar beat transitions in sperm brought about by changes in external fluid viscosity. As briefly mentioned in previous chapters, changes in fluid viscosity can lead to large flagellar beat transitions in sperm of various species. Sea urchin sperm have been observed to exhibit planar swimming at water-like viscosity, helical beating at 1500 times the viscosity of water and planar beating again at 4000 times the viscosity of water (Woolley and Vernon, 2001). Avian sperm such as quail and pigeon sperm exhibit a geometrically complex beat at water-like viscosity, and a helical beat at 1500 times that viscosity (Vernon and Woolley, 1999). Mammalian sperm also behave differently; bull and human sperm at water-like viscosity exhibit a rolling beat, and at higher viscosities begin to exhibit planar beating (Smith et al., 2009a; Hyakutake et al., 2015b). We note that while the differences between species are striking, differences are also often reported within samples of the same species; reports tend to focus on the predominant behaviour of the population, although some studies such as Hyakutake et al. (2015b) have attempted to quantify differences within the population. Hence the beat patterns and trends mentioned above should not be considered universal across species, but representative.

The mechanisms behind these beat transitions are yet unknown, and are thought to involve changes in the activity of the protein motors within the axoneme (Lindemann and Lesich, 2021). However, only preliminary ideas have thus far been proposed (Woolley and Vernon, 2001) to explain how this might occur when there are no external biochemical changes. This study instead explores the possibility that viscosity-related beat transitions may have elastohydrodynamic origins.

To do this, the motion of a single flagellum-like filament is simulated

in quiescent fluid of different viscosities. The Internally-driven Kirchhoff Rod (IDKR) model is used along with the numerical methods described in Chapter 3. As discussed before, the driving bending moment is predetermined and its direction is kept constant relative to the local reference frame associated with each material cross-section. The qualitative behaviour of this system is governed by S, the frequency of the internal driving wave relative to the time-scale of the elastohydrodynamic response, A, the amplitude of the imposed driving wave relative to the flexibility of the filament, and k, the non-dimensional wavenumber of the driving wave. As noted from their definitions in Chapter 3, the parameters S and A are also dependent on the length and bending stiffness of the flagellum, and S is additionally dependent on the external fluid viscosity. The effect of increasing the external fluid viscosity is studied by increasing S while keeping the length, bending stiffness and frequency of the driving wave constant. This would correspond to fluid viscosity changes for the same species of sperm, assuming that the internal driving remains unchanged. The trends predicted by the simulations are also compared to those seen in experiments of sea urchin sperm, as reported in the literature (Woolley and Vernon, 2001).

4.2 Emergent Planar Waveforms

The emergent motion of a force-free and torque-free IDKR is tracked in time to observe the effect of varying S, A and k. All other parameters are kept constant and approximately within the range observed in sperm. The radius-to-length ratio of the filament is set to $1/100$, which approximately corresponds to that seen in various species of mammalian sperm, considering the radius of the thickest part of the flagellum (Gu et al., 2019). The ratio of bending and twisting stiffnesses is set to unity. The dimensionless wavenumber of the driving wave is set to either 2π or 4π, which is expected to result in one or two waves over the length of the flagellum respectively.

As S, A and k are varied, four visually-distinct types of beating patterns are obtained, the first of which is a planar wave-like beat (Figure 4.1) which is qualitatively similar to the planar beating patterns of various species of sperm. Planar beat patterns have been investigated in various 2D simulation studies employing different types of internal driving (Ishimoto and Gaffney, 2018; Gadêlha et al., 2010; De Canio et al., 2017; Oriola et al., 2017) and are an expected result in this study since the internal driving consists only of bending moments, and should hence act to propagate bends along the filament. Figure 4.2 demonstrates the effect of varying S and A for a set of planar beats at $k = 4\pi$. Noting that the driving wave acts like a time-varying preferred curvature (discussed in Chapter 3), we compare the maximum curvatures of the

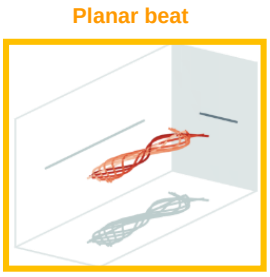

Figure 4.1: Representative beat cycle of a planar beat at $S = 7, A = 5, k = 2\pi$.

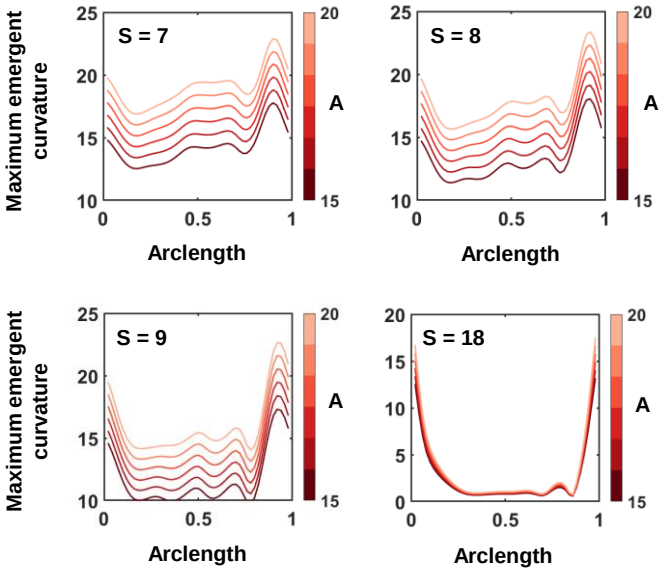

Figure 4.2: Maximum curvatures of the emergent waveforms along the centerline over a beat period for $S = 7, 8, 9$ and 18, for $A = 15$ to 20, $k = 4\pi$. Arclength of $s = 0$ represents the 'head' of the swimmer.

emergent waveforms as A is varied for four different values of S (Figure 4.2). The oscillation of curvature at every point along the centerline is approximately sinusoidal, and hence the maximum value provides a preliminary description. We first note that while the amplitude of the active driving (preferred curvature) is constant along the arclength, the emergent waveforms have a more complex curvature profile due to nonlinearities in the system. We also note that the emergent curvature profiles are not symmetric along the filament's length, although the active driving is symmetric and there is no imposed structural asymmetry or external constraint (such as pinning or clamping).

An increase in the dimensionless driving amplitude A (while keeping all other parameters constant) results in an increase in the emergent curvature profile for the lower S values of $7, 8$ and 9. An increase in the emergent curvature amplitudes corresponds to an increase in the beat amplitude, as shown in Figure 4.3. The curvature values at $S = 18$, however, have a very different profile and vary only slightly as A is increased. This indicates that planar beating at high S may involve different mechanisms – this will be investigated further in the following chapter.

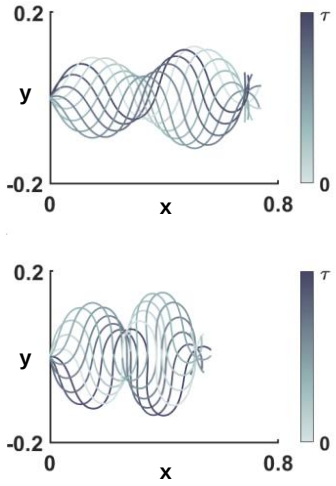

Figure 4.3: Timelapse of the centerline over one beat cycle τ, at $S = 7$, $A = 15$ (top) and $A = 20$ (bottom), $k = 4\pi$. Centerlines have been translated such that the 'head' of the swimmer is located at (0,0) at each time point.

Waveform comparisons using POD

A more formal comparison can be achieved by decomposing the centerline curvature using Proper Orthogonal Decomposition into spatially-dependent modes and time-dependent coefficients, as introduced in Chapter 3. While the maximum curvature provides an initial picture of the variation in curvature along the centerline, it does not capture complex spatial and time-dependent features of the curvature profile. A more complete understanding can be obtained using the POD curvature modes. We recall from Chapter 3 that the curvature function can be decomposed as

$$\kappa(s,t) = \kappa_0(s) + \sum_{i=1}^{N} B_{\kappa,i}(t)\kappa_i'(s),$$

where $\kappa_0(s)$ is the time-averaged curvature, $\kappa_i'(s)$ are the spatially-dependent curvature modes and $B_{\kappa,i}(t)$ are their respective time-dependent coefficients. The time-averaged curvatures are approximately zero for all cases presented here, and hence the shape modes and coefficients together describe the shape of the filament. In all cases presented here, the first two modes account for over 95% of the variation in curvature, as indicated by the cumulative sum of the eigenvalues corresponding to the modes (Figure 4.4).

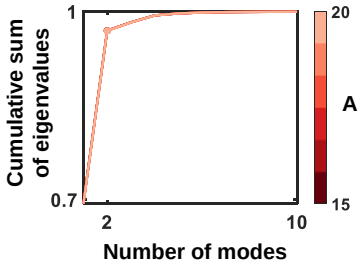

Figure 4.4: Cumulative sum of eigenvalues plotted against number of modes for $S = 18$, $A = 15 - 20$, $k = 4\pi$. Dot indicates sum of eigenvalues of first two modes.

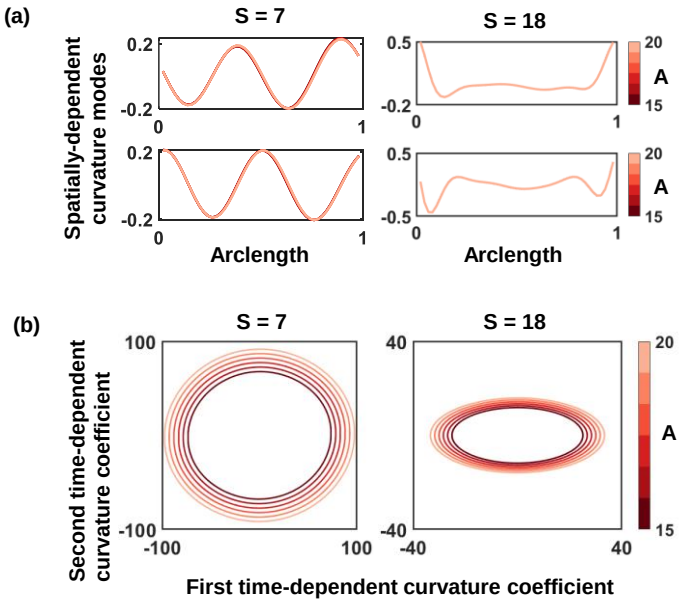

Figure 4.5: (a) First (top panel) and second (bottom panel) spatially-dependent curvature modes for $A = 15$ to 20, $S = 7$ (left) and $S = 18$ (right), $k = 4\pi$. (b) First and second time-dependent coefficients plotted against each other over > 80 cycles for $A = 15$ to 20, $S = 7$ (left) and $S = 18$ (right), $k = 4\pi$.

Figures 4.5(a) shows the first (top panel) and second (bottom panel)

curvature modes $\kappa_1'(s)$ and $\kappa_2'(s)$ for $S = 7$ and $S = 18$ respectively, for various values of A. Figure 4.5(b) shows plots of the first time-dependent coefficient $B_{\kappa,1}(t)$ against the second, $B_{\kappa,2}(t)$, which exhibit closed loops or 'limit cycles'. Limit cycles are commonly observed in the shape decompositions of experimental beat waveforms (Nandagiri et al., 2021; Guasto et al., 2020; Ishimoto et al., 2018) and are indicative of the periodicity of the shape, with one beat cycle corresponding to one complete loop. The overlapping limit cycles, plotted over tens of beat cycles, indicate that the beat pattern remains the same every cycle. The absence of any 'dents' or smaller loops within the limit cycle indicates that both $B_{\kappa,1}$ and $B_{\kappa,2}$ oscillate at the same frequency.

We observe in Figure 4.5(a) that across different values of A at each S, the spatial modes are identical. The increase in curvature amplitude with A is instead reflected as increases in the values of the time-dependent coefficients, which is observed as an increase in the size of the limit cycle. Meanwhile, the differences between waveforms at $S = 7$ and $S = 18$ are very clearly reflected in the spatial modes. On the other hand, a change in the dimensionless wavenumber does not alter the beat waveform. For example, the first two spatial modes and time dependent coefficients at $S = 18$ and $A = 15$ are exactly as shown on the right side in Figure 4.5(a).

Figure 4.6 plots the power spectral densities of the first time-dependent coefficient against frequencies normalised with respect to the driving frequency. Although the plot shows only $A = 15$, all of the planar waveforms show similar peaks at the driving frequency and its harmonics, indicating that the beat frequency of the filament coincides with the driving frequency. The beat period is therefore defined as the period of the driving wave. The same definition will be used throughout this work.

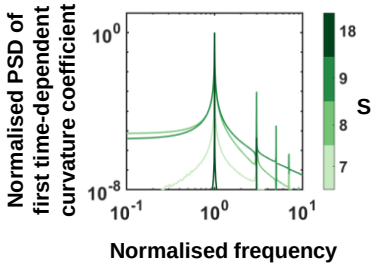

Figure 4.6: Comparison of the normalised power spectral density of the first time-dependent coefficient of curvature at $A = 15$ for $S = 7, 8, 9$ and 18.

4.3 Emergent Three-dimensional Waveforms

The other three types of beating patterns obtained in the simulations are three-dimensional. Shown in Figure 4.7(b) is a 'rolling-planar' beat in which the waveform is approximately planar but the filament rolls about its own axis. This beat is similar to that seen in bull and human sperm swimming in water-like viscosity (Hyakutake et al., 2015b). A snapshot of this beat is provided in Figure 4.7(f), and a more detailed description of this beat in bull sperm is provided in Chapter 6. At higher dimensionless amplitudes of $A = 15$ and above, the high emergent curvatures additionally result in the filament 'looping' over itself, as shown in Figure 4.8.

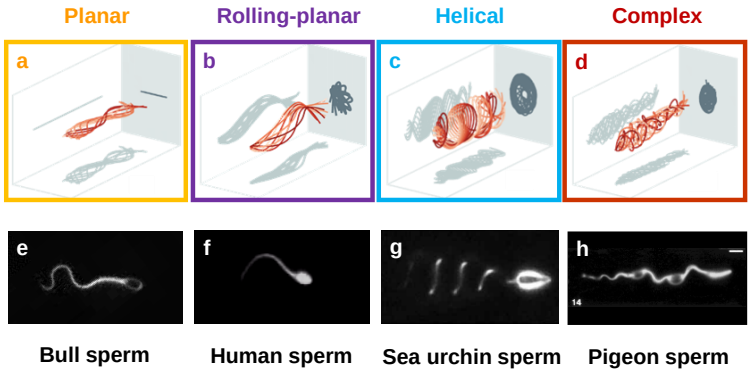

Figure 4.7: (a)-(d) Representative beat cycles of the four qualitative beating types obtained in simulations: (a) planar beat at $S = 7, A = 5, k = 2\pi$; (b) rolling-planar beat at $S = 5, A = 5, k = 2\pi$; (c) helical beat at $S = 12, A = 20, k = 4\pi$; (d) complex beat at $S = 15, A = 20, k = 4\pi$. Note that complex beats may look visually different at different parameters. (e)-(h) Microscope image of (e) bull sperm exhibiting planar beating; (f) human sperm exhibiting rolling-planar beating; (g) sea urchin sperm exhibiting helical swimming, reproduced from (Vernon and Woolley, 1999) with permission; (h) pigeon sperm exhibiting complex beating, reproduced from (Woolley and Vernon, 2001) with permission. Images (e) and (f) were provided by F. Yazdan Parast (Monash University).

Figure 4.7(c) shows a helical beat that repeats regularly in time, such as that seen in sea urchin sperm (Figure 4.7(g)). Remarkably, the helically swimming filaments seem to exhibit 'pulsing', which is described in Woolley and Vernon (2001) as an apparent train of vibrations superimposed over the helical shape of sperm in high viscosity media. The top panel of Figure 4.9 shows a depiction of this behaviour in the simulations – the trajectory of the 'head' is plotted for a pulsing helical swimmer at $S = 12$, $A = 23$ over 4 beat cycles. Describing each oscillation of the head as a 'pulse', we see approximately two pulses per beat cycle, as also indicated by the first peak frequency of the z-coordinate of the head (orange plot in the bottom panel of Figure 4.9). As far as the author is aware, this is the first simulation evidence of this phenomenon. This finding provides support for the suggestion that helical beating in sperm may emerge due to elastohydrodynamic mechanisms. The pulses in helical swimmers are observed to occur as a result of the response of the filament to the active driving wave, superimposed over the overall helical shape. The head of a planar filament would exhibit an oscillation once per cycle, as the beat cycle follows the input frequency (PSD of the first time-dependent coefficient of curvature is shown in Figure 4.11). A pulse, however, occurs twice in a beat cycle. This is explained by the rolling of the filament. The black plot in the bottom panel of Figure 4.9 shows the frequency response of the z-coordinate of the $\mathbf{d}_3$ material vector at the head, which indicates that the head rolls approximately once

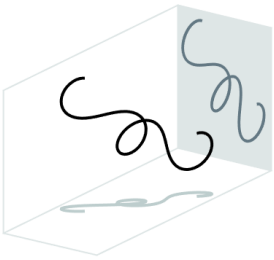

Figure 4.8: Snapshot of 'looping' in a rolling-planar beat.

every beat cycle. This ultimately results in the first half of the head's oscillation matching the second half, which is observed from a global reference frame as two pulses. Importantly, the plot also indicates that the rolling of the filament is a subharmonic response and does not match the filament's beat frequency.

The final category, Figure 4.7(d), comprises a variety of beats that are periodic but more complex. Complex beating patterns such as that shown in the figure have been observed in avian sperm such as pigeon sperm (Figure 4.7(h)). Figure 4.10 shows important differences in the evolution of curvature and torsion for each type of beat pattern. The Frenet curvature of the centerline describes the shape of the filament without taking into account its overall forward motion or rolling, and hence allows us to view the filament just as it might 'view' itself. Planar, rolling-planar and helical beats are observed to have a travelling-wave-like curvature profile (as one may expect) which appears to be the same every beat cycle. In the complex beat, on the other hand, patterns occurring over a few beat cycles can be observed (top panel of the figure). The torsion profile, on the other hand, is different for each type of three-dimensional beat, with the planar beat exhibiting no torsion (bottom panel of the figure). In the rolling-planar beat we see spikes in torsion at just a few points along the flagellum at any instant in time, while the rest of the flagellum remains approximately torsion-free, i.e. planar. The helical beat, on the other hand, exhibits travelling waves in torsion, and the complex beat shows complex patterns that repeat every few cycles.

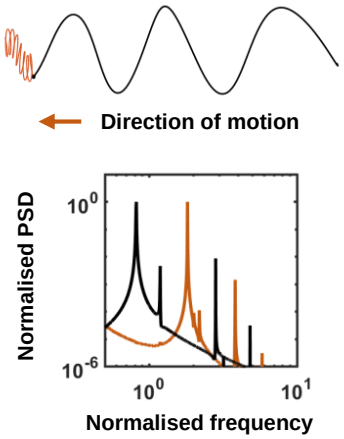

Figure 4.9: Depiction of pulsing in helical filaments. Top panel shows trajectory of the 'head' (black dot) in red over 4 beat cycles. Bottom panel shows the normalised power spectral density (PSD) of the z-coordinate of the head position (orange line) and the z-coordinate of the binormal material vector $\mathbf{d}_3$ at the head (black line), plotted against frequency normalised with respect to the driving frequency.

While the different beat types were first identified visually, it is possible to distinguish between the categories using a more quantitative approach. As before, the curvature function is decomposed into spatially-dependent modes and their respective time-dependent coefficients. Shown in the top panel of Figure 4.11 are the normalised power spectral densities (PSD) of the first time-dependent coefficient of the curvature function for each type of beating. We observe a different frequency response for each type of three-dimensional beat; the rolling-planar beat exhibits a peak at the driving frequency, whereas the helical beat shows peaks at the driving frequency and its harmonics, indicating the presence of shape changes that occur two or more times *within* each beat cycle. Complex beats (last column of the figure) tend to exhibit more complicated frequency responses including several sub-harmonic peaks representing patterns that occur over a few beat cycles. For all types of beating, the main peak occurs at the driving frequency. The same 'beat frequency' definition is hence retained for all beat pattern types.

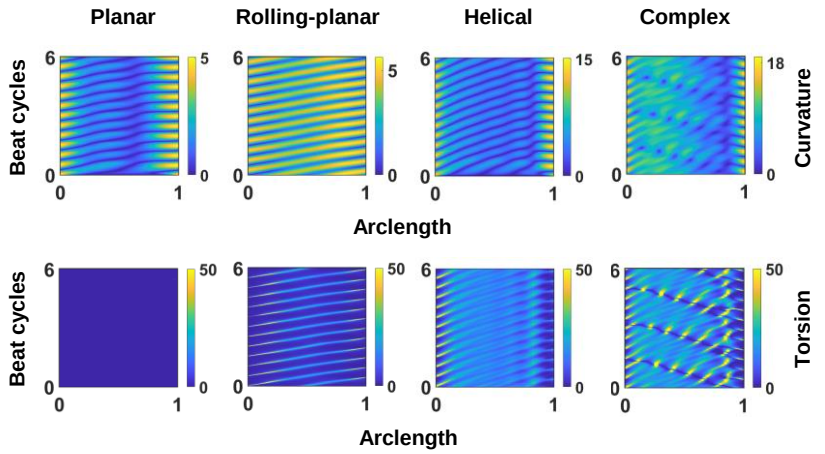

Figure 4.10: Top panel: Kymographs of centerline curvature magnitude for representative planar ($S = 9, A = 10, k = 4\pi$), rolling-planar ($S = 5, A = 5, k = 2\pi$), helical ($S = 12, A = 15, k = 4\pi$) and complex ($S = 15, A = 20, k = 4\pi$) beats as labelled, shown for six beat cycles. Bottom panel: Kymographs of centerline torsion magnitude for the same planar, rolling-planar, helical and complex beats respectively, shown for six beat cycles.

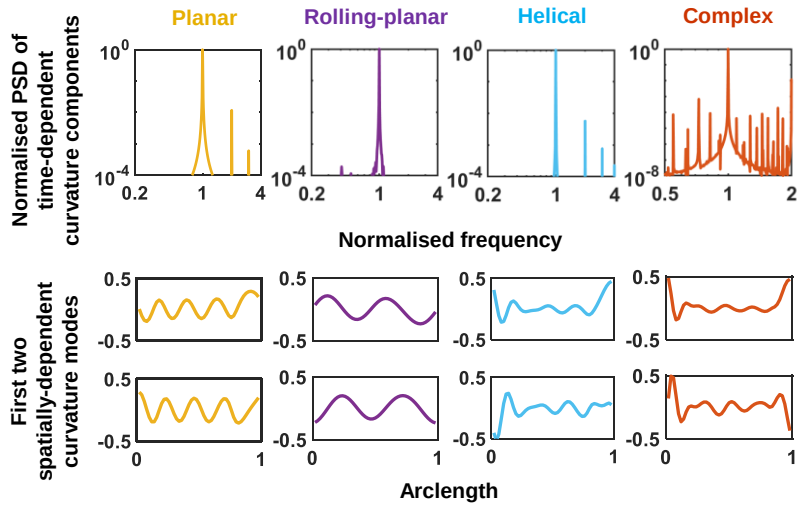

Figure 4.11: Top panel: Comparison of the normalised power spectral densities of the time-dependent components of centerline curvature magnitude for representative planar ($S = 9, A = 10, k = 4\pi$), rolling-planar ($S = 5, A = 5, k = 2\pi$), helical ($S = 12, A = 15, k = 4\pi$) and complex ($S = 15, A = 20, k = 4\pi$) beats as labelled, plotted against frequencies normalised using the driving frequency. Bottom panel: First (top) and second (bottom) curvature modes of the same planar, rolling-planar, helical and complex beats respectively.

The bottom panel of the figure shows the first two curvature modes for each beat. Planar and rolling-planar beats show a wave-like curvature profile, as expected. The number of waves appears to be twice the driving wavenumber because the absolute value of the curvature has been used here. The helical and complex beats show more complex

spatial modes; while this is expected for the complex beat, for the helical beat this may be due to pulsing. In the planar, rolling-planar and helical beats, the first two modes capture over 95% of the variation in curvature, whereas for complex beats they capture just over 60%.

4.4 The Parameter Map explains Viscosity-related Beat Transitions

The remarkable likeness of these beat patterns to those observed in sperm holds very important implications in the biology of flagella and cilia. Previous studies that have used active moments or time-varying preferred curvature have not reported obtaining three-dimensional beat patterns with uni-directional driving; helical beating has been achieved previously by applying driving waves along two material directions instead of one (Ishimoto and Gaffney, 2018). Biologically, this means that the axoneme would have to, through some biochemical mechanism, activate (or inactivate) different sets of dynein motors to switch from planar to helical beating. In that light, some possible patterns of dynein activity for planar and helical beating are discussed in Lindemann and Lesich (2021). The same is true of a previous study that has obtained both planar and three-dimensional beat patterns in filaments clamped on one end, by varying the strength of follower force distributions along the centerline (which is expected to require some biochemical regulation within the axoneme) (Ling et al., 2018). As explained below, the results in this study suggest instead that beating pattern transitions can be achieved without any changes within the axoneme.

Figure 4.12 shows the occurrence of the different types of beats in the parameter space of S and A for two different dimensionless wavenumbers of 2π and 4π. Yellow dots indicate planar beats, purple dots indicate rolling-planar beats, blue dots indicate helical beats and red dots indicate complex beats. We note that rolling-planar beats are only observed at $k = 2\pi$. Moreover, three-dimensional beats occur over a much broader range of S and A at $k = 2\pi$. At $k = 4\pi$, planar beating is most common, and three-dimensional beating (helical beating, largely) appears to be restricted to a small area of the parameter space. Interestingly, complex beats are not spread over a large region but instead occur at interfaces between planar and helical beats. This indicates that complex beats may be a transitional state between planar and three-dimensional beating.

We now compare these beating patterns to experiments of sperm swimming in fluids of different viscosities. In the simulations, external fluid viscosity enters the picture through the Swimming number defined

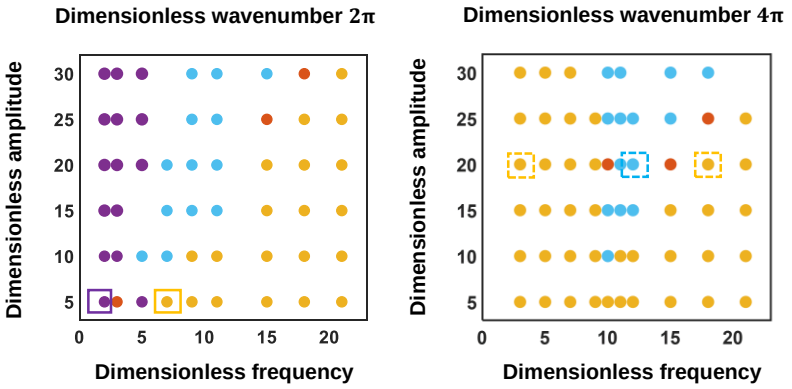

Figure 4.12: Phase map showing the four types of beating for a dimensionless wavenumber of 2π (left) and 4π (right); colours of the dots represent the beating pattern type: planar (yellow), rolling-planar (purple), helical (blue) and complex (red). Dashed boxes highlight one possible set of parameters that correspond to the beat patterns of sea urchin sperm at 1 cP (planar), 1500 cP (helical) and 4000 cP (planar) in the order of increasing dimensionless frequency. Solid boxes highlight a set of parameters that may correspond to the beat patterns of bull sperm at 1 cP (rolling-planar) and above 20 cP (planar).

earlier in Chapter 3, $S = L(\mu\omega^a/K_B)^{1/4}$, where L is filament length, μ is fluid viscosity, ω^a is the frequency of the internal driving wave and K_B is the filament's bending stiffness. An increase in S can hence be interpreted as an increase in fluid viscosity keeping the driving wave frequency, filament length and bending stiffness constant. Due to the simplicity of the model, such comparisons at this stage are preliminary and qualitative at best. Yet, similarities are observed between predicted and observed viscosity-related beating pattern transitions in sperm of different species.

For example, sea urchin sperm have been reported to exhibit planar beating in water-like viscosity, helical beating in a fluid 1500 times the viscosity of water and planar beating again in a fluid 4000 times the viscosity of water (Woolley and Vernon, 2001). This trend is captured in the second phase map as the change from planar to helical to planar beating by increasing S and holding all other parameters constant. While a direct quantitative comparison is not possible since the experimental values of S and A cannot be determined, we can use the ratios of fluid viscosity to estimate that helical beating should occur at 6 times the Swimming number of the initial planar motion, and the second transition to planar beating should occur at 8 times the initial Swimming number. These ratios are captured in the simulation results for initial Swimming numbers (in water-like viscosity) of 2-3, and corresponding dimensionless amplitudes of 20-30. One possible set of parameters is highlighted in the phase map corresponding to $k = 4\pi$ in Figure 4.12

(dashed boxes). Our aim here is not to provide quantitative matches between simulations and experiments, but to demonstrate that the experimental trend is captured reasonably by the simulations while assuming that the frequency of the internal driving wave, ω^a, does not change at all.

As a second example, bull sperm exhibit rolling-planar beating at water-like viscosity and planar beating at high viscosity (Hyakutake et al., 2015b; Zaferani et al., 2021). This transition is captured in the phase map corresponding to $k = 2\pi$ in Figure 4.12 (solid boxes highlight a possible set of parameters). Chapter 6 provides a more detailed comparison highlighting the similarities between the experimentally observed beating patterns in bull sperm and simulation results, and also discusses the differences in the beat transitions exhibited by sea urchin and bull sperm.

4.5 Chapter Summary

This study has shown, for the first time, that an active bending moment wave can give rise to both planar as well as experimentally-relevant three-dimensional beat patterns. Unlike in previous studies, the three-dimensional beat patterns in this work do not arise as a result of any imposed structural or driving asymmetry, or due to bi-directional driving. This work hence suggests a new elastohydrodynamic mechanism behind the emergence of planar and three-dimensional beat patterns from the same internal driving, as observed in sperm. The mechanisms leading to the emergence of three-dimensional beats from uni-directional driving will be explored in the next chapter.

Planar beating is observed both at low dimensionless frequencies and very high dimensionless frequencies, and the beat frequency coincides with the active driving frequency when all other parameters are kept constant. Increasing the driving amplitude while keeping all other parameters constant results in an overall increase in the curvature profile along the centerline, which ultimately results in larger beating amplitudes. This behaviour is more easily observed at lower dimensionless frequencies. Planar waveforms at high dimensionless frequencies appear to be different from those at low dimensionless frequencies. This will be investigated further in the next chapter. It was also observed that the emergent shape can be asymmetric along the length of the filament although there are no structural or driving asymmetries.

The three-dimensional beat patterns obtained were classified into three qualitative types: rolling-planar beating similar to that seen in

bull sperm; helical beating similar to that seen in sea urchin sperm; and complex beating which is a category for beats that are more difficult to describe. Three-dimensional beats occur over a much smaller region of the parameter space at a dimensionless wavenumber of 4π as compared to 2π. Notably, the rolling-planar beat is observed at a dimensionless wavenumber of 2π, but not 4π. All four categories (including planar beating) are visually different, and can also be differentiated based on the spatial and time-dependent components of centerline curvature and torsion. Remarkably, helically swimming filaments exhibit 'pulsing', a previously-unexplained phenomenon observed in helically swimming sea urchin sperm.

Finally, phase maps were constructed to study the occurrence of various types of beating across a parameter space of dimensionless frequency and amplitude, for the two different dimensionless wavenumbers of 2π and 4π. Noting that the dimensionless frequency parameter depends on the external fluid viscosity, transitions between different types of beating were compared to literature data of sea urchin sperm swimming at different fluid viscosities. It was found that the planar-helical-planar transition exhibited by sea urchin sperm in fluids of increasing viscosity is captured by the simulations qualitatively as well as approximately quantitatively. These results suggest the first elastohydrodynamic mechanism behind this viscosity-related beat pattern transition, which is currently thought to require changes in protein motor activity within the axoneme. This is explored further in Chapter 6, which compares the simulation results presented here to experimental data of bull sperm swimming at different fluid viscosities.

5

Exploring the Origins of Non-planar Beating Patterns

5.1 Introduction

This Chapter probes the origins of the three-dimensional beat patterns obtained in the previous Chapter. As discussed before, the emergence of three-dimensional beating patterns from an active-bending-moment driving has not been reported in previous studies. This finding suggests a new elastohydrodynamic mechanism behind the emergence of both planar and three-dimensional beating from the same pattern of internal driving. This elastohydrodynamic mechanism does not require any complex biochemical changes in the active driving (as a result of changes within the axoneme) or any intrinsic structural asymmetries in the filament. Noting the biological importance of understanding the emergence of the three-dimensionality in flagellar beats (Lindemann and Lesich, 2021; Guerrero et al., 2011), we now explore the underlying mechanisms by considering two possibilities.

The first is that the initially planar beat is gradually forced out of plane by long-range hydrodynamic interactions, over the course of a few beat cycles. Long-range hydrodynamic interactions have been shown to play an important role in bacterial flagellar propulsion and flagellar synchronisation (Lauga, 2016) as well as synchronisation in eukaryotic cilia and flagella (Brumley et al., 2012; Chakrabarti and Saintillan, 2019a). To investigate the importance of long-range hydrodynamic interactions, the simulations are repeated after replacing the hydrodynamics model with Resistive Force Theory, which only considers local drag effects. If the transitions in beating patterns are solely due to non-local effects, one would not observe such transitions in simulations using RFT. This is presented in the following section.

The second possibility is the presence of a buckling-type instability, due to which planar beating is unstable at certain regions of the parameter space. Elastohydrodynamic instabilities in flagella have commonly

been investigated in the context of spontaneous emergence of oscillatory beating (Oriola et al., 2017; De Canio et al., 2017; Chakrabarti and Saintillan, 2019b) as well as beat transitions (Ling et al., 2018). The observations of sharp boundaries in the phase diagrams in the previous Chapter suggest that bifurcations occur in the qualitative behaviour with respect to parameter changes. Here a linear stability analysis is performed in an attempt to capture a region in the parameter space where a planar filament would be unstable to perturbations in its shape. Section 5.3 outlines the approach taken before presenting the corresponding results.

5.2 Role of Long-range Hydrodynamic Interactions

Now the Stokesian Dynamics model is replaced with Resistive Force Theory (RFT), which captures only the local hydrodynamic drag on each part of the filament and ignores long-range hydrodynamic interactions (HI). The hydrodynamic force and moment per unit length acting on a cross section are now expressed as

$$\mathbf{f^h} = -(\zeta_1 v_1 \mathbf{d}_1 + \zeta_2 v_2 \mathbf{d}_2 + \zeta_3 v_3 \mathbf{d}_3), \tag{5.1}$$

$$\mathbf{m^h} = -\zeta_r \boldsymbol{\omega}. \tag{5.2}$$

where the subscripts denote material directions $\mathbf{d}_1, \mathbf{d}_2$ and $\mathbf{d}_3$. The resistance coefficients are expressed as

$$\zeta_1 = \frac{2\pi\mu}{\ln(0.18\lambda/a) - \frac{1}{2}};$$

$$\zeta_2 = \zeta_3 = \frac{4\pi\mu}{\ln(0.18\lambda/a) + \frac{1}{2}};$$

$$\zeta_r = 8\pi\mu a^2,$$

where μ is external fluid viscosity, a is the radius of the filament and λ is the beat wavelength. Here the velocity drag coefficients provided in Lighthill (1976) have been used.

Figure 5.1 shows the emergence of different types of beating as the dimensionless frequency and amplitude are varied while keeping the dimensionless wavenumber constant at 4π. We find that while three-dimensional beating patterns still emerge, the range of parameters over which they occur has diminished, leading to qualitative differences in beat pattern types over some regions of the parameter space. This indicates that the three-dimensional beats do not emerge as a result of long-range hydrodynamic interactions. However, the absence of long-range HI can create large qualitative differences in the beat patterns in

some regions of the parameter space, especially at high A and intermediate S values where three-dimensional beats are observed. In regions where the beat patterns are qualitatively similar, differences exist in the beat amplitudes. Shown in Figure 5.2 are comparisons between two planar beats predicted by RFT (yellow lines) and the Stokesian Dynamics model (black lines). For the example at $S = 7$, $A = 15$, $k = 4\pi$ (top), the beat patterns are nearly identical. However, at $S = 9$, $A = 15$, $k = 4\pi$, differences in the curvature amplitude can be observed, as shown in Figure 5.2(d).

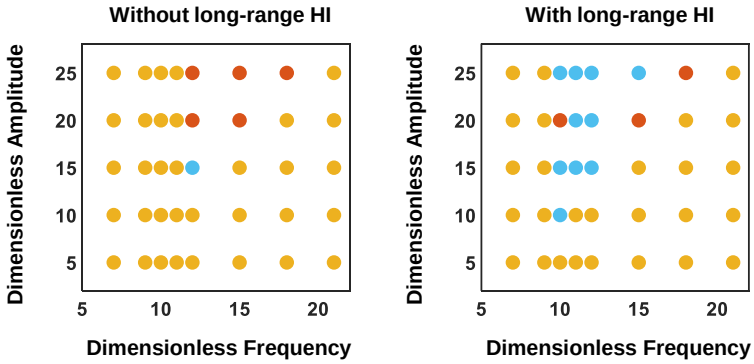

Figure 5.1: Parameter space showing the emergence of three types of beating at a dimensionless wavenumber of 4π, when considering only local anisotropic hydrodynamic drag (left) and when long-range hydrodynamic interactions are included (right). The plot on the right was presented earlier in Chapter 4 Figure 4.12.

We recall from the discussion in Chapter 2 that RFT is still commonly used in both experimental and simulation studies, due to its ease of implementation. These results add to numerous studies (Jung et al., 2007; Walker et al., 2019; Martindale et al., 2016) that have demonstrated the importance of including long-range hydrodynamic interactions when modelling cilia and flagella. On the other hand, since three-dimensional beats can still emerge when using local drag models such as Resistive Force Theory, it is possible that the results discussed in this paper would be broadly applicable to other systems involving the inertialess locomotion of elastic filaments experiencing local drag – for example, inertialess motion of snake-like organisms or robots within dry granular media (Zhang and Goldman, 2014).

More importantly, these results suggest that the underlying mechanism behind three-dimensional motion emerging from the active-bending-moment driving is an instability that is triggered even without non-local hydrodynamic interactions.

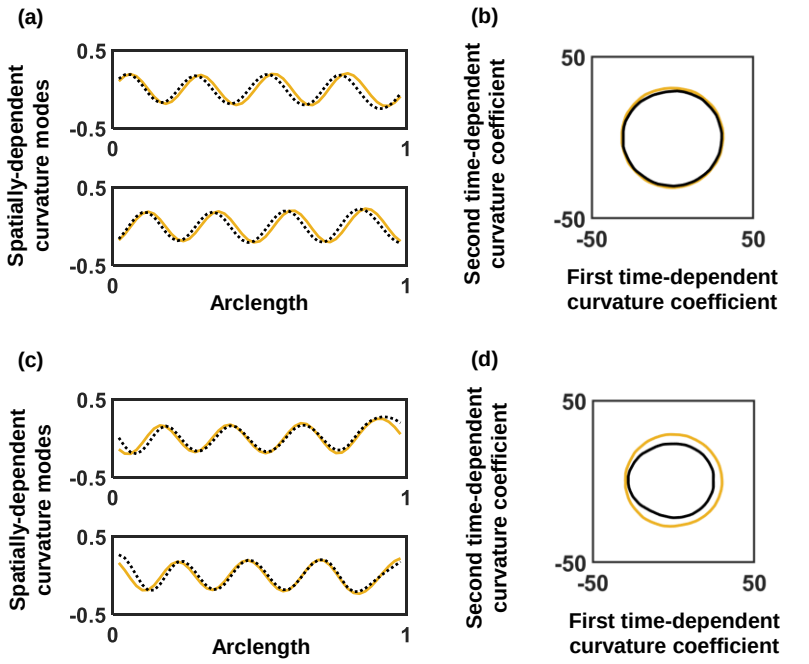

Figure 5.2: Comparison of planar beat patterns obtained using local drag theory (yellow lines) and using the Stokesian Dynamics model (black lines). (a),(c) First (top panel) and second (bottom panel) spatially-dependent curvature modes for a planar swimmer at (a) $S = 7$, $A = 15$, $k = 4\pi$, and at (c) $S = 9$, $A = 15$, $k = 4\pi$. (b),(d) Plots of the first time-dependent coefficient of curvature against the second for the planar swimmers in (a) and (c) respectively.

5.3 Linear Stability of Planar Beating

We now explore the presence of an elastohydrodynamic instability which renders planar beating unstable at parameters where three-dimensional beats are observed. To do this, planar beats, i.e. *base states* are first computed at all parameters including those at which beats become three-dimensional – this is done by restricting the simulations to two dimensions, as discussed in the following subsection. Perturbations are then applied in the filament curvature and the evolution of the perturbations is numerically tracked in time. The analysis here is restricted to linear order.

Determining Planar Base States

For planar oscillating filaments, only two of the material frame vectors change with time, and the shape of the filament can be described by a single variable $\theta(s,t)$, which is referred to as the *tangent angle* (Figure

5.3). For a filament beating in the $x-y$ plane,

$$\mathbf{d}_1 = \cos(\theta)\mathbf{e_x} + \sin(\theta)\mathbf{e_y},$$
$$\mathbf{d}_2 = -\sin(\theta)\mathbf{e_x} + \cos(\theta)\mathbf{e_y},$$
$$\mathbf{d}_3 = \mathbf{e_z}.$$

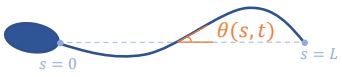

Figure 5.3: Definition of the tangent angle θ for a planar swimmer. The depiction of a head in this figure is for illustrative purposes only.

The model equations presented in Chapter 3 are considerably simplified, since velocities and forces are non-zero only in $\mathbf{d}_1$ and $\mathbf{d}_2$, while angular velocities and torques are non-zero only in the $\mathbf{d}_3$ direction. This also implies that the only non-zero curvature component is Ω_3, so that the passive internal moment is now

$$\mathbf{M} = K_B\Omega_3\ \mathbf{e_z},$$

and the hydrodynamic force and moment are expressed as

$$\mathbf{f^h} = -(\zeta_1 v_1\ \mathbf{d}_1 + \zeta_2 v_2\ \mathbf{d}_2), \tag{5.3}$$
$$\mathbf{m^h} = -\zeta_r\omega_3\ \mathbf{d}_3, \tag{5.4}$$

with the coefficients as defined before. The system is numerically integrated in time taking a similar approach as outlined in Chapter 3, i.e. implicit second-order backward differencing in time and solution using Bad Broyden's method. The implementation is based on the MATLAB code provided in Schoeller et al. (2021) for passive elastic filaments, which has been modified for this system.

Shown in Figure 5.4 are two examples of planar beats, obtained at $S = 9$, $A = 20$, $k = 4\pi$ (top) where the beat predicted by the 3D simulations is also planar, and at $S = 15$, $A = 20$, $k = 4\pi$ (bottom) where 3D simulations predict a complex beat. For the planar swimmer at $S = 9$, $A = 20$, the beat predicted by the 2D simulations (shown in the figure using yellow lines) closely matches that obtained in the 3D simulations (black lines), whereas at $S = 15$, $A = 20$, $k = 4\pi$ the curvature profiles are visibly different.

Equations for the Evolution of Curvature Perturbations

This Section explores whether the planar base states are linearly stable to perturbations in the shape. To aid this analysis, the model equations are first expressed in terms of the evolution of curvature. We recall from Chapter 3 the compatibility relation (3.8), which can be expressed in vector form as

$$\frac{\partial\boldsymbol{\Omega}}{\partial t} = \frac{\partial\boldsymbol{\omega}}{\partial s} + \boldsymbol{\omega}\times\boldsymbol{\Omega}. \tag{5.5}$$

Using the angular momentum balance (3.12), the constitutive relation for the passive internal moment (3.17) and the hydrodynamic relation

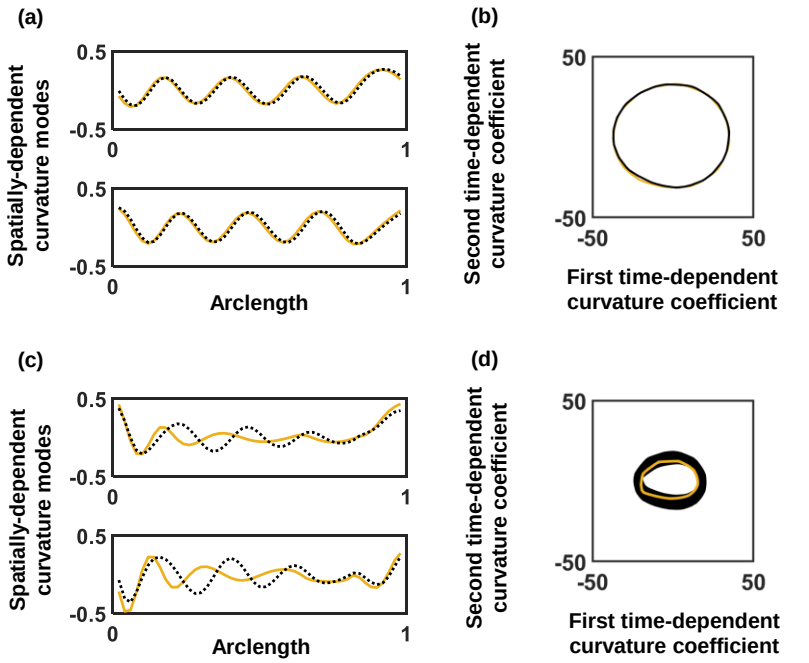

Figure 5.4: Planar beat patterns obtained in 2D simulations. (a),(c) First (top panel) and second (bottom panel) spatially-dependent curvature modes for a planar swimmer at (a) $S = 9$, $A = 20$, $k = 4\pi$, and at (c) $S = 15$, $A = 20$, $k = 4\pi$ where the 3D simulations had predicted a complex non-planar beat. Yellow lines represent the 2D simulations, and black lines represent 3D simulations. (b),(d) Plots of the first time-dependent coefficient of curvature against the second for the swimmers in (a) and (c) respectively.

(5.2), the angular velocity can be expressed as

$$\omega = \frac{1}{\zeta_r}\left[\frac{\partial(\mathbf{K}\cdot\mathbf{\Omega})}{\partial s} + \mathbf{d}_1 \times \mathbf{F} + \frac{\partial \mathbf{M^a}}{\partial s}\right], \tag{5.6}$$

with

$$\mathbf{M^a} = M_0 \cos(k^a s - \omega^a t)\mathbf{d_3}.$$

This has, however, introduced the internal force due to material stresses, $\mathbf{F}$ into the equations. Using the linear momentum balance (3.10) and the hydrodynamic relation (5.2), we obtain

$$\mathbf{v} = \boldsymbol{\mathcal{M}} \cdot \frac{\partial \mathbf{F}}{\partial s}, \tag{5.7}$$

where

$$\boldsymbol{\mathcal{M}} = \frac{1}{\zeta_1}\mathbf{d}_1\mathbf{d}_1 + \frac{1}{\zeta_2}\mathbf{d}_2\mathbf{d}_2 + \frac{1}{\zeta_3}\mathbf{d}_3\mathbf{d}_3. \tag{5.8}$$

We also have the following relationship between linear and angular velocity, which is a consequence of Equations (3.9), (3.7) and (3.2):

$$\frac{\partial \mathbf{v}}{\partial s} = \boldsymbol{\omega} \times \mathbf{d}_1. \tag{5.9}$$

The above expressions for $\mathbf{v}$ and $\boldsymbol{\omega}$ can now be substituted into (5.5) and (5.9) to obtain the following closed set of equations, which shall henceforth be referred to as the curvature-stress equations:

$$\frac{\partial}{\partial s}(\boldsymbol{\mathcal{M}} \cdot \frac{\partial \mathbf{F}}{\partial s}) = \frac{1}{\zeta_r}\left[\frac{\partial(\mathbf{K}\cdot\boldsymbol{\Omega})}{\partial s} + \mathbf{d}_1 \times \mathbf{F} + \frac{\partial \mathbf{M^a}}{\partial s}\right] \times \mathbf{d}_1, \tag{5.10}$$

$$\frac{\partial \boldsymbol{\Omega}}{\partial t} = \frac{1}{\zeta_r}\left[\frac{\partial}{\partial s}\left(\frac{\partial(\mathbf{K}\cdot\boldsymbol{\Omega})}{\partial s} + \mathbf{d}_1 \times \mathbf{F} + \frac{\partial \mathbf{M^a}}{\partial s}\right) + \left(\frac{\partial(\mathbf{K}\cdot\boldsymbol{\Omega})}{\partial s} + \mathbf{d}_1 \times \mathbf{F} + \frac{\partial \mathbf{M^a}}{\partial s}\right) \times \boldsymbol{\Omega}\right]. \tag{5.11}$$

Now the curvature and internal stress are expressed as

$$\boldsymbol{\Omega} = \boldsymbol{\Omega^0} + \boldsymbol{\Omega^1} + \mathcal{O}(\epsilon^2);$$
$$\mathbf{F} = \mathbf{F^0} + \mathbf{F^1} + \mathcal{O}(\epsilon^2),$$

where $\boldsymbol{\Omega^0}$ and $\mathbf{F^0}$ correspond to the respective base states of $\boldsymbol{\Omega}$ and $\mathbf{F}$, and $\boldsymbol{\Omega^1}$ and $\mathbf{F^1}$ represent perturbations about the base state to leading order, with ϵ representing a small parameter. Here $\boldsymbol{\Omega^n} = (\Omega_1^n, \Omega_2^n, \Omega_3^n)$ and $\mathbf{F^n} = (F_1^n, F_2^n, F_3^n)$, where the subscripts denote the material directions $\mathbf{d}_1, \mathbf{d}_2$ and $\mathbf{d}_3$. Substituting the above into the curvature-stress equations and retaining terms only up to first order, the following set of six scalar equations (expressed in dimensionless form), which govern the evolution of the perturbation variables, are obtained:

$$F_1^{1\prime\prime} - \frac{\zeta_1}{\zeta_3}(2F_1^0\Omega_3^0\Omega_3^1 + F_1^1{\Omega_3^o}^2) - (1+\frac{\zeta_1}{\zeta_2})(\Omega_3^0F_2^{1\prime} + \Omega_3^1F_2^{0\prime}) - F_2^0\Omega_3^{1\prime} - F_2^1\Omega_3^{0\prime} = 0;$$
$$F_2^{1\prime\prime} - \frac{\zeta_2}{\zeta_1}(2F_2^0\Omega_3^0\Omega_3^1 + F_2^1{\Omega_3^o}^2) + (1+\frac{\zeta_3}{\zeta_1})(\Omega_3^0F_1^{1\prime} + \Omega_3^1F_1^{0\prime}) + F_1^0\Omega_3^{1\prime} + F_1^1\Omega_3^{0\prime} - \frac{\zeta_2}{\zeta_r}L^2(\Omega_3^{1\prime} + F_2^1 - C) = 0;$$
$$F_2^{1\prime\prime} - (1+\frac{\zeta_2}{\zeta_1})\Omega_2^1F_1^{0\prime} - F_1^0\Omega_2^{1\prime} + F_1^0\Omega_3^0\Omega_1^1 + \frac{\zeta_2}{\zeta_1}F_2^0\Omega_3^0\Omega_2^1 + 2\Omega_1^1F_2^{0\prime} + F_2^0\Omega_1^{1\prime} + \frac{\zeta_3}{\zeta_r}L^2(\Omega_2^{1\prime} - F_3^1 - \Omega_1^1B) = 0;$$
$$-\frac{\zeta_rL^3}{K_B}\dot{\Omega}_1^1 + \frac{K_T}{K_B}\Omega_1^{1\prime\prime} - 2\Omega_2^1C + \Omega_2^{1\prime}B + \Omega_2^1\Omega_3^{0\prime} + F_2^0\Omega_2^1 - \Omega_3^0\Omega_2^{1\prime} + \Omega_3^0\Omega_1^1 + B + \Omega_3^0F_3^1 = 0;$$
$$-\frac{\zeta_rL^3}{K_B}\dot{\Omega}_2^1 + \Omega_2^{1\prime\prime} + 2\Omega_1^1C - B\Omega_1^{1\prime} - F_3^{1\prime} - \Omega_1^1\Omega_3^{0\prime} - F_2^0\Omega_1^1 + \frac{K_T}{K_B}\Omega_3^0\Omega_1^{1\prime} + \Omega_3^0\Omega_2^1B = 0;$$
$$-\frac{\zeta_rL^3}{K_B}\dot{\Omega}_3^1 + \Omega_3^{1\prime\prime} - D + F_2^{1\prime} = 0,$$

with

$$B = A\,\cos(ks - S^4t);$$
$$C = A\,k\sin(ks - S^4t);$$
$$D = A\,k^2\cos(ks - S^4t),$$

where A, S and k represent the dimensionless amplitude, frequency and wavenumber, respectively. Here, primes denote differentiation with respect to s, and the dot superscripts denote differentiation with respect

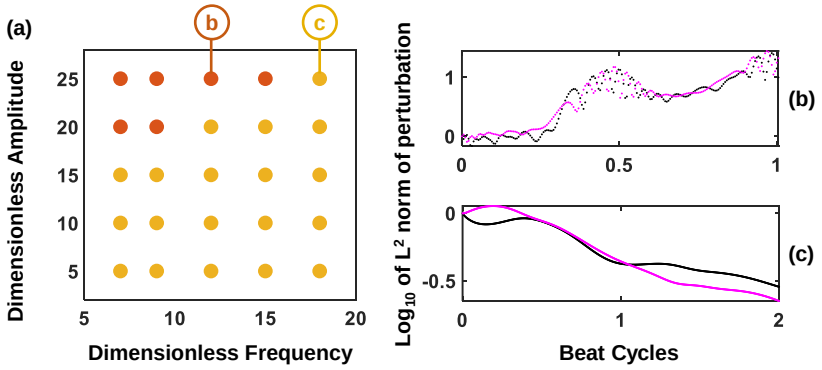

Figure 5.5: (a) Parameter map showing points where the planar base states are linearly stable (yellow) and unstable (red) to curvature perturbations. (b)-(c) Log_{10} of the L^2 norm of $\Omega_1^1(s)$ (black) and $\Omega_2^1(s)$ (magenta) as a function of time (shown in terms of beat cycles) for the points indicated in (a). Values are normalised with respect to the initial magnitude.

to t. The boundary conditions for the force- and torque-free filament are as follows:

$$\Omega_1^1|_{s=0} = \Omega_1^1|_{s=L} = 0, \quad \Omega_2^1|_{s=0} = \Omega_2^1|_{s=L} = 0, \quad \Omega_3^1|_{s=0} = \Omega_3^1|_{s=L} = 0,$$
$$F_1^1|_{s=0} = F_1^1|_{s=L} = 0, \quad F_2^1|_{s=0} = F_2^1|_{s=L} = 0, \quad F_3^1|_{s=0} = F_3^1|_{s=L} = 0.$$

Linearly Unstable Regions in the Parameter Space

The MATLAB PDE solver `pdepe` is used to solve the system of equations. An initial sinusoidal perturbation is applied in both Ω_1 and Ω_2:

$$\Omega_1^1(s_i, t=0) = \Omega_2^1(s_i, t=0) = \epsilon[\sin(\pi s_i) + \sin(2\pi s_i) + \sin(4\pi s_i) + g],$$

where g represents a random number between -0.5 and 0.5, and ϵ is chosen to be 10^{-3}. The aim of this analysis is only to identify whether an initial perturbation grows or decays at a particular set of parameters. To do this, the above system of equations is integrated in time for a duration of 1-5 beat cycles and then the change in the magnitude of the perturbation is noted. Figure 5.5(b) and (c) show how the L^2 norm of $\Omega_1^1(s)$ (black line) and $\Omega_2^1(s)$ (magenta line) change with time, for two example points in the parameter space. A growth in these variables would indicate that the planar base state is unstable. The L^2 norm is defined as

$$||\Omega_1^1|| = \sqrt{\int_0^L (\Omega_1^1(s,t))^2 \, ds}.$$

Figure 5.5(c) shows the evolution of the perturbations for a parameter set where the out-of-plane perturbations decay, hence indicating that the planar state is stable. On the other hand, Figure 5.5(b) shows a point where the perturbations grow, leading to a non-planar beat. Looking at

the parameter space in Figure 5.5(a), we find that at low to intermediate dimensionless frequencies and high dimensionless amplitudes (for example, point (b) in the figure), planar base states are linearly unstable. Meanwhile at high dimensionless frequencies and amplitudes (point (c) in the figure), the planar beat is linearly stable to perturbations. Comparing these results with the full nonlinear simulations (Figure 5.1), we see firstly that the unstable (red) region partially overlaps with the region where three-dimensional beating occurs, i.e. at intermediate dimensionless frequencies and high dimensionless amplitudes.

At low dimensionless frequencies where the nonlinear simulations predict stable planar beating, the linear stability results indicate an unstable behaviour at high dimensionless amplitudes. Hence, nonlinearities appear to have a stabilising influence on beating patterns at low dimensionless frequencies and high dimensionless amplitude. This may be a contributing factor to the observation in Chapter 4 that planar beating at low dimensionless frequencies and high dimensionless frequencies have different shape modes. The transition from three-dimensional beating at intermediate dimensionless frequencies back to planar beating at high dimensionless frequencies, however, appears to be a linear stability effect.

In conclusion, linear stability analysis is able to capture the transition from planar to three-dimensional beating as dimensionless amplitude increases for intermediate dimensionless frequencies, as well as the transition from three-dimensional to planar beating as dimensionless frequency increases for high dimensionless amplitudes. At low dimensionless frequencies and high dimensionless amplitudes, it appears that the growth of out-of-plane perturbations is dampened and countered by nonlinear terms. Further, the onset of three-dimensional beating occurs at much lower dimensionless amplitudes of $15 - 20$ than predicted here. This may be due to the fact that increasing dimensionless amplitudes result in higher flagellar curvatures (as discussed in Chapter 4). Under such conditions, nonlinear effects resulting from coupling between curvature components as well as between curvature and internal tension forces become more significant (Gadêlha et al., 2010).

5.4 Chapter Summary

The emergence of non-planarity (or torsion) in flagellar beating patterns has been a long-standing mystery, with several hypotheses including change in protein motor activity within the axoneme, asymmetries in flagellar structure and internal driving as well as elastohydrodynamic instabilities (Lindemann and Lesich, 2021; Ling et al., 2018; Guerrero

et al., 2011). This Chapter explored the mechanisms that give rise to the three-dimensional beats observed in the simulation results in Chapter 4.

The role of long-range hydrodynamic interactions was first investigated by repeating the simulations after replacing the hydrodynamics model with Resistive Force Theory. The corresponding results showed that while three-dimensional beating patterns still emerge, the range of parameters over which they occur diminishes when using Resistive Force Theory, leading to qualitative differences in beat pattern types at high dimensionless amplitudes and intermediate dimensionless frequencies. It was also observed that even at parameters where the beat patterns qualitatively match, quantitative differences exist. While many studies in the literature continue to use local drag theories when modelling cilia and flagella, these results suggest that long-range hydrodynamic interactions should be included for a more complete understanding.

Since the emergence of three-dimensional beating is not primarily due to the effect of long-range hydrodynamic interactions, the presence of a linear elastohydrodynamic instability in the system was investigated while considering only local drag. This involved applying small out-of-plane shape perturbations to planar base states at each parameter, and observing whether the perturbations grow or decay. It was found that linear stability analysis could capture the transition from three-dimensional beating to planar beating as the dimensionless frequency is increased while keeping the dimensionless amplitude high. The transition from planar to three-dimensional beating as dimensionless amplitude increases is also predicted, although the stability boundary is not accurately captured.

These results indicate that at low dimensionless frequencies and high dimensionless amplitude, nonlinear effects stabilise the planar beating pattern. This may be a contributing factor to the observation in Chapter 4 that planar waveforms at low dimensionless frequencies are different to those at high dimensionless frequencies. These results also demonstrate the importance of modelling cilia and flagella in three dimensions, and at large curvature amplitudes.

6
Experimental Observations of Bull Sperm in Media of Different Viscosities

6.1 Introduction

This chapter discusses changes in the beating patterns of bull sperm swimming in methyl cellulose solutions of different viscosities, using experimental data provided by F. Yazdan Parast and R. Nosrati (Department of Mechanical and Aerospace Engineering, Monash University). Quantitative analysis of the data is performed in this work, with the aim of comparing the beat transitions exhibited by bull sperm to those predicted by the simulation results in Chapter 4. The availability of experimental data allows us to make more quantitative comparisons than those presented in Chapter 4 using literature data.

Experimental reports of sperm swimming in fluids of different viscosities are available in the literature for several species, including sea urchin sperm (Woolley and Vernon, 2001), various avian sperm (Vernon and Woolley, 1999) and various mammalian sperm such as bull sperm (Hyakutake et al., 2015b; Zaferani et al., 2021), human sperm (Ishimoto et al., 2018) as well as mice, chinchilla and ram sperm (Woolley, 2003). Elevation of the fluid viscosity is commonly achieved through the addition of small quantities (up to 2%) of methyl cellulose (Woolley and Vernon, 2001; Vernon and Woolley, 1999; Woolley, 2003; Smith et al., 2009b; Ishimoto et al., 2018). This results in a medium with properties similar to human cervical mucus in terms of sperm penetration (Ivic et al., 2002).

Studies traditionally provide qualitative descriptions of the waveform along with averaged waveform parameters such as beat frequency, amplitude and wavenumber. For example, Hyakutake et al. (2015b) study bovine sperm in Newtonian solutions of polyvinylpyrrolidone and report the average velocities, beat amplitude, frequency and proportion of cells

which exhibit rolling at each of five viscosity levels up to approximately 20 cP. While these parameters provide a first description of the overall features of the waveforms, they cannot be used to describe complex features of the waveform that vary in space and time.

More recently, studies have begun to use computer-assisted image analysis techniques to provide more detailed quantitative analyses of flagellar beat waveforms (Gallagher et al., 2019; Nandagiri et al., 2021; Smith et al., 2009b; Guasto et al., 2020). The waveform is generally described using centerline curvature (Guasto et al., 2020; Smith et al., 2009b) or tangent angle profiles (Nandagiri et al., 2021; Ishimoto et al., 2018; Gallagher et al., 2019), which capture shape variations without the effect of overall forward motion or rolling. Further analyses of the spatial and time-variance of the shape have been performed using techniques such as Proper Orthogonal Decomposition (Nandagiri et al., 2021; Guasto et al., 2020; Ishimoto et al., 2018).

In this study, similar quantitative analyses are performed for bull sperm at three different nominal viscosities of 1 cP, 5 cP and 75 cP, where they exhibit rolling-planar, complex and planar waveforms, respectively. While studies thus far have largely been restricted to planar waveforms, this work provides the first quantitative analysis of more complex three-dimensional beat patterns based on their 2D images. The beat patterns as well as the beat transition trends observed here are then compared to the simulation results in Chapter 4, and parallels with the behaviour exhibited by sea urchin sperm are discussed.

6.2 Sperm Sample Preparation, Imaging and Waveform Extraction

Sperm sample preparation and imaging were performed by F. Yazdan Parast. The procedure is briefly described here. Bull semen was purchased in 150μL straws (from ABS Australia) and stored in liquid nitrogen before use. At the time of the experiment, the semen is thawed to 37°C and diluted in a pre-warmed HEPES buffer of pH 7.4, consisting of 117 mM NaCl, 5.3 mM KCl, 1.8 mM $CaCl_2.2H_2O$, 0.8mM $MgSO_4$, 1mM NaH_2PO_4, 5.5 mM D-glucose, 0.03 mM phenol red, 4 mM $NaHCO_3$, 21 mM HEPES, 0.33 mM Na pyruvate, 21.4 mM Na lactate and 0.3 mg/mL bovine serum albumin. The viscosity of the buffer is raised through the addition of 0.1 to 1% methyl cellulose (M0512, purchased from Sigma-Aldrich). Based on the manufacturer's data, solution of 2% methyl cellulose at 20°C results in a nominal viscosity of 4000 mPa.s. The diluted sperm samples are incubated at 37°C until imaging.

For imaging, a chamber of depth approximately 90 μm is first prepared by fixing two strips of tape along the two long ends of a microscope slide. A 20 μL drop of the diluted semen is added to the chamber, followed by another drop of high-viscosity buffer adjacent to it. A coverslip is placed on top such that the two drops interface, while ensuring minimal air-bubble formation. The sides of the chamber at the short ends of the slide are then sealed to prevent fluid flow driven by evaporation. A duration of $1-2$ minutes is allowed so that the motile sperm swim across the interface area and into the high-viscosity buffer where debris is minimal. This not only provides better images with minimal debris, but also selects only motile sperm from the sample. High-speed high-resolution dark-field microscopy is used to obtain images of free-swimming sperm in the high viscosity buffer at 200 frames per second for 2.5 seconds. The imaging system consists of an AX-70 upright microscope (Olympus, Japan) equipped with an ORCA-Flash4.0 v2 + sCMOS camera (Hamamatsu, Japan), a darkfield condenser (numerical aperture (NA)=0.9), and a U-DFA 18 mm internal diameter dark-field annulus with a UPlanAPO 10× objective (NA= 0.4) (Olympus, Japan). Sperm near the centre of the coverslip that are at a distance of more than one body length away from other sperm are selected for imaging.

Processing of the images and extraction of centerline position vectors was performed in collaboration with F. Yazdan Parast. The videos are first cropped so that each frame contains only a single sperm, and the flagellar centerline is extracted using the automated image analysis algorithm detailed in Nandagiri et al. (2021), which makes use of the MATLAB Image Processing Toolbox and the Bio-Formats library. The Bio-Formats library is used to read the image files and extract metadata containing the timestamps of each image. The images are then processed through a series of steps beginning with background subtraction, followed by contrast enhancement, noise removal using median filters and the application of a Gaussian filter to smoothen the edges of the flagellum. This is followed by thresholding and the identification of the flagellum as the object in the image with the largest area and a high eccentricity (since particles of debris are often circular). The identified flagellum is then skeletonised to obtain the centerline, and any branches or spurs are removed. Finally, a low-pass filter is applied to smoothen the centerline, and its x and y positions are obtained. Image processing parameters are tuned to suit the overall dataset, with some parameters tuned for every individual video.

The obtained position vectors are subsequently used to calculate the total arclength extracted at every frame. Arclength variation between frames is larger for rolling sperm with significant out-of-plane motion.

For subsequent calculations, the centerline is truncated at the minimum extracted arclength for uniformity. The curvature profile is calculated from the centerline position vectors as described in Chapter 3.

6.3 Analyses of Beat Patterns at Different Viscosities

We observe the beat patterns of bull sperm as the nominal viscosity of the medium is increased from 1 cP to 250 cP ($0 - 1\%$ methyl cellulose). Nominal viscosities have been estimated using data provided by the manufacturer, and throughout this chapter 'viscosity' refers to the estimated nominal viscosity.

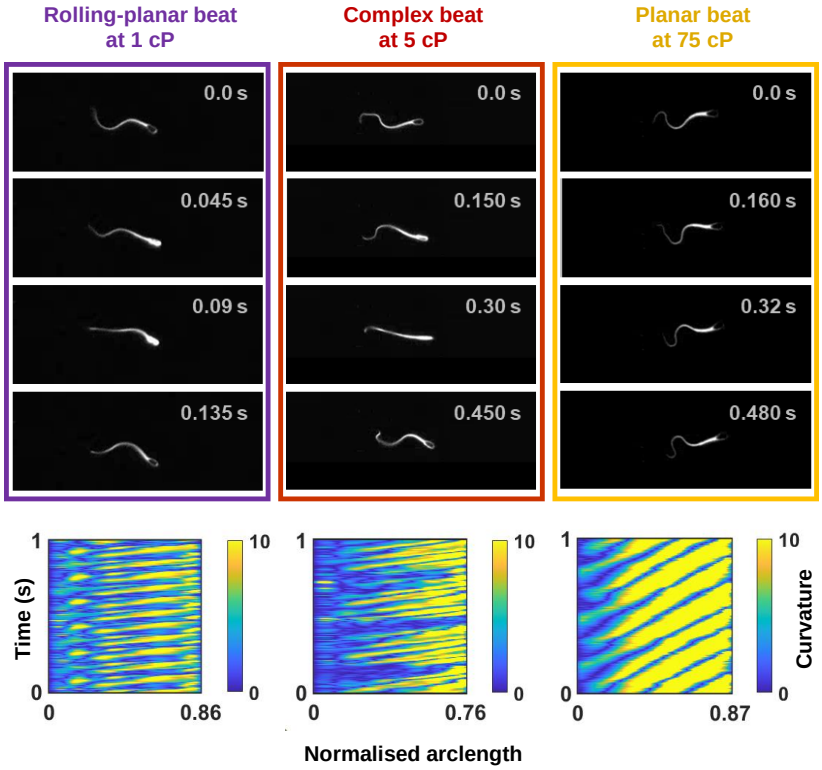

Figure 6.1: Top: Four equally-spaced time points in the individual beat cycles of a representative (a) rolling planar, (b) complex and (c) planar beat observed in bull sperm swimming in external medium viscosity of 1 cP, 5 cP and 75 cP respectively. Bottom: Kymographs of the 2D centerline curvature along the flagellum, up to the minimum extracted arclength.

At 1 cP, sperm cells predominantly exhibit a rolling motion similar to the rolling-planar motion defined in Chapter 4. Video frames of this beat pattern are shown in the leftmost column of Figure 6.1 for a representative swimmer over one beat cycle. Here, a beat cycle is defined in the same manner as in the simulations, i.e. as the minimum frequency of

oscillation exhibited by the curvature. We note that the curvatures calculated here are based only on 2D centerline data and cannot be used to completely describe the three-dimensional waveforms. The aim of this work is only to provide a comparison between the three qualitatively different waveforms.

The 'rolling-planarity' can be inferred from the video frames – the rolling of the head is visible as flashes of high intensity in the head region (purple line in the first plot of Figure 6.2), and the video frame at 0.09s in the figure shows the near-planarity of the beat which becomes visible as the swimmer's beat plane becomes perpendicular to the microscope's plane of focus. At this point in the beat cycle, the 2D length of the flagellum falls to a minimum, and a significant part of the flagellum lies outside the plane of focus. This is indicated by the non-uniform brightness along the length of the flagellum seen in the video frame. The second and third plots in Figure 6.2 show a comparison of the 2D length variation of the experimental swimmer with one from the simulations, which also shows a similar pattern. The 2D curvature profile along the flagellum is shown in the bottom panel of Figure 6.1, from where we observe the periodic variation of the shape.

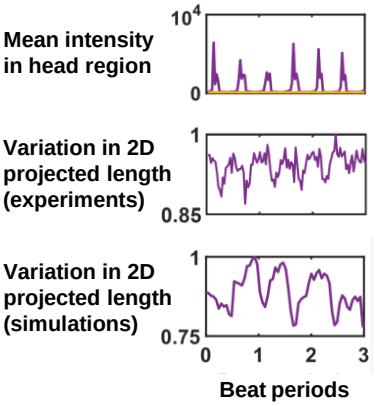

Figure 6.2: Top panel: Mean light intensity over the head region of a rolling-planar (purple line) and planar (yellow line) bull sperm over 3 beat periods, obtained from microscope videos. Middle panel: Variation in the 2D projected length of the rolling-planar bull sperm, based on the plane of view shown in Figure 6.1. Bottom panel: Variation in the 2D projected length of a simulated rolling-planar sperm at $S = 2, A = 5, k = 2\pi$, based on the plane perpendicular to its direction of motion.

When the medium viscosity is increased to 5 cP, the cells continue to roll but the waveform appears more complex, especially towards the distal end as observed in the videos as well as the kymograph in the middle panel of Figure 6.1. Snapshots of the waveform are shown in the middle column of Figure 6.1. We also observe that the rolling becomes slower; this is visible in the curvature kymograph, which has much fewer bands than that of the rolling-planar swimmer.

At higher viscosities of 20 cP, 75 cP and 250 cP, the beating becomes predominantly planar. Snapshots of the waveform of a representative swimmer at 75 cP is shown in the last column of Figure 6.1. The unchanging intensity profile at the head region confirms that the cell doesn't roll – this is indicated by the yellow line in the first plot of Figure 6.2. The beat frequency of the planar beat is also slower than that of the rolling planar beat, as the corresponding kymograph indicates.

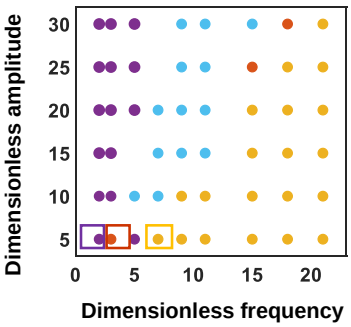

Figure 6.3: Parameter space presented in Chapter 4 showing the occurrence of the four types of beating for a dimensionless wavenumber of 2π; boxes indicate parameter estimates corresponding to the three beat pattern types of bull sperm at 1 cP, 5 cP and 75 cP.

The trends reported here agree qualitatively with other studies that report the transition in bull sperm from rolling motion to planar motion with increasing viscosity (Hyakutake et al., 2015b; Zaferani et al., 2021). In those studies, the viscosity beyond which the beat becomes predominantly planar also appears to lie between $10 - 25$ cP, for different types of Newtonian as well as non-Newtonian fluid media used. However, the transition appears to be more gradual in those studies, with comparable

proportions of rolling and non-rolling sperm observed at viscosities of around 20 cP. For the samples at 20 cP in this study, hardly any sperm exhibit rolling.

The transition from rolling-planar to complex to planar beating is observed in the simulation results at the points indicated in Figure 6.3. The complex beat swimmer predicted by the simulations, however, appears visually different from the one observed in experiments. This could be due to the various simplifying assumptions in the study, which will be further discussed in the following section. Nevertheless, the prediction of the complex beating is noteworthy as it suggests that the simulations likely capture the underlying mechanisms behind these beat transitions. The top panel of Figure 6.4 provides a comparison of the three experimental beat types in terms of the power spectral densities of the first time-dependent coefficients of curvature. We note that the complex beat (red line) has more peaks than the planar and rolling-planar beats. A similar trend is seen in the simulation results as well, as shown in the bottom panel of the figure.

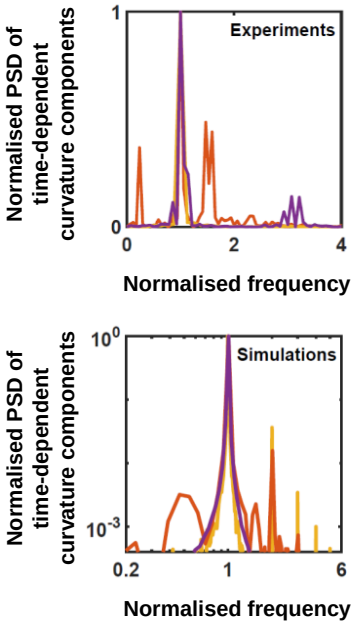

Figure 6.4: Comparison of the normalised power spectral densities of the time-dependent components of centerline curvature for the representative planar (yellow), rolling-planar (purple) and complex (red) beats, for (top panel) the three representative sperm cells shown in Figure 6.1 and (bottom panel) the three points enclosed in solid squares in Figure 6.3.

6.4 An Explanation for Differences between Species and within Species

These transitions are significantly different to those discussed in the previous section for sea urchin sperm. While there exists the possibility that the axonemal driving is itself different in different species, the simulation results point to an alternative explanation. It is known that although the structure of the axoneme remains primarily the same in both species, bull sperm are around 1.6 times longer and possess accessory structures around the axoneme that increase the stiffness of the flagellum and give it a tapering thickness (Gu et al., 2019; Gray and Hancock, 1955). The beating wavenumber of approximately 2π seen in bull sperm is also different to that of sea urchin sperm, whose wavenumber is around 4π (Gray and Hancock, 1955). In the simulations, an increase in bending stiffness and length keeping all else constant (including the internal driving wave and fluid viscosity) would result in different S and A values, possibly pushing the flagellum into a different regime of beating although the external fluid viscosity is the same.

The bending stiffness of bull sperm is estimated to be around $4-5$ times that of sea urchin sperm flagella, using values reported in Lindemann et al. (1973) and Okuno and Hiramoto (1979) for sperm in media containing 10 mM ATP. A four-fold increase in bending stiffness along with a 60% increase in length would result in A decreasing by 60% and S increasing slightly by $5-10\%$. This would mean that for bull sperm

swimming in water-like viscosity, S remains approximately the same as sea urchin sperm (between $2-3$) while A decreases to approximately 10. Looking at the map for $k = 2\pi$ we see that a rolling planar beat is indeed predicted for S between $2-3$ and A between $5-10$. Using the ratio of viscosities as before in Chapter 4, we expect irregular beating at 1.5 times the initial dimensionless frequency, but planar beating is predicted to occur only beyond 3.5 times the initial dimensionless frequency, which corresponds to a much higher viscosity of 150 cP.

It must be noted, however, that a quantitative match cannot be expected at this stage due to the preliminary nature of the model and estimates used. For example, the bending stiffness values used are only estimates and can vary by an order of magnitude depending on several factors (Lindemann et al., 1973). Secondly, the model in this work has not accounted for a tapering flagellum thickness and bending stiffness, which can be expected to alter the observed beating patterns by suppressing buckling instabilities (Gadêlha and Gaffney, 2019). This may be a contributing factor to the transition to planar beating in experiments much earlier than predicted by simulations. The inclusion of a sperm head is not expected to create large qualitative differences in the observed beat patterns, but would be required for more quantitatively accurate predictions (Elgeti et al., 2011; Ishimoto and Gaffney, 2014, 2015). It may also be of interest to vary the radius-to-length ratio to more closely match that of sea urchin and other sperm species to understand its effect on beating patterns. It is further known that methyl cellulose solutions are weakly viscoelastic, exhibiting storage and loss moduli in oscillatory shear experiments, and shear thin under steady shear (Smith et al., 2009b; Walker et al., 2020b; Hyakutake et al., 2015a). The weakly viscoelastic nature of the fluid medium also presents a modelling challenge and may be expected to produce quantitative differences (Zaferani et al., 2021; Pate and Brokaw, 1980).

Nevertheless, in a qualitative sense, these results show that the differences in beating patterns across species may possibly have elastohydrodynamic origins rather than differences in the internal driving, as currently imagined. While one could argue that differences in beat patterns could also involve differences in the internal driving, an elastohydrodynamic mechanism agrees well with the idea that since the structure of the axoneme is very similar across species, its working mechanism should also be similar. It was observed in the experiments that beating patterns can differ even within a sample of the same species. Such differences would be even less likely to involve differences in axonemal driving, and may instead be driven elastohydrodynamically by slight differences in the length of the flagellum. A mere 5% increase in the length of the

flagellum (which is well within that observed in experiments) would result in a 10% increase in A, which would be more than sufficient to keep the longer cell and shorter cell on opposite sides of the transition boundary, as the simulation results suggest. Supporting this idea is the observation that beat pattern differences within a sample are more pronounced at the viscosities around which the transition from irregular to planar beating occurs. This has previously been quantified by Hyakutake et al. (2015b) and Zaferani et al. (2021) as the percentage of rolling and non-rolling bull sperm at different viscosities.

6.5 Chapter Summary

In summary, this Chapter has presented an analysis of experimental data of the motion of bull sperm in methyl-cellulose-supplemented buffer solutions of nominal viscosities between $1 - 250$ cP. At water-like viscosity, sperm predominantly exhibit a rolling motion similar to the rolling-planar motion observed in the simulations in Chapter 4. At a slightly higher viscosity of 5 cP, the rolling motion appears a little more complex, and beyond 20 cP the motion becomes predominantly planar. The rolling-planar beat has a visibly higher beat frequency compared to the other two beats. This work provides the first detailed analysis of 'complex' beats observed in sperm.

The transition from rolling-planar beating to complex beating to planar beating is qualitatively captured in the simulation results of Chapter 4. Although the complex beating in experiments appears visually different to that predicted by the simulations, it is similar in that it displays multiple frequency responses, unlike the other two types of beats. The ability of the simulations to capture this beat transition indicates that it may have elastohydrodynamic origins.

It was further demonstrated that the difference between the beat patterns observed here for bull sperm and those discussed in Chapter 4 for sea urchin sperm may not be due to differences in the internal driving, but could instead be linked to the difference in their lengths and bending stiffnesses. Differences in beating pattern within a sample of the same species, which are more unlikely to involve differences in the internal driving, may also result from such structural differences. This work hence suggests the first elastohydrodynamic mechanism behind beat pattern differences observed between different species as well as within the same species.

An important difference between the experiments and simulations is that the fluid medium in the experiments is weakly viscoelastic. How-

ever, the viscosity value of around 20 cP beyond which the transition to planar beating occurs approximately matches similar experimental studies of bull sperm in different Newtonian and weakly viscoelastic fluid media, indicating that the effect of viscoelasticity may be minor.

Another difference is the presence of surfaces in the experiment – sperm swim in wide but shallow channels of approximately 90μm depth, and may experience hydrodynamic effects from plane surfaces above and below. The next Chapter investigates the effect of surfaces on beat waveforms.

7
Effect of a Plane Wall on Beat Patterns

7.1 Introduction

This Chapter explores the effect of a plane wall on flagellar beat patterns. While sperm in the female reproductive tract encounter surfaces of very complex geometries (Suarez, 2016), experimental studies commonly involve visualising the motion of sperm in a fluid medium bounded by microscope slides or coverslips (Woolley and Vernon, 2001; Nosrati et al., 2015; Friedrich et al., 2010). The presence of a plane wall has been shown to change the overall swimming trajectory of sperm, causing them to swim towards and accumulate at the surface (Winet et al., 1984; Woolley, 2003). Not all sperm in a given sample accumulate, and among those that do, the distance from the wall at which stable swimming occurs can vary over tens of micrometers (Winet et al., 1984). Sperm swimming very close to the surface have been observed to swim in circular trajectories (Woolley and Vernon, 2001; Woolley, 2003), while away from the wall their trajectories are linear. Sperm have also been observed to change their beat waveform near a wall; a striking example is the 'slither' transition exhibited by bull and human sperm (Nosrati et al., 2015), where sperm switch from a three-dimensional rolling in bulk fluid to a planar slithering motion within a micrometre of the surface. This transition results in an increased swimming speed in human sperm, but reduced speed in bull sperm.

Near-wall swimming behaviour is hence complex and yet to be fully understood. Theory as well as simulation studies have been able to provide valuable insight into some of the mechanisms driving the observed behaviour. In the far field, sperm behave as *pusher* force dipoles (Lauga and Powers, 2009). The tendency of sperm to swim towards boundaries has been attributed to the hydrodynamic attraction of pusher dipoles. The dipole approximation also predicts the approximately parallel orientation of the pusher with respect to the wall (Lauga and Powers, 2009; Elgeti et al., 2015). While the far-field approximation provides a pre-

liminary understanding, the near-field becomes increasingly important near a wall (Elgeti et al., 2015).

A number of studies have hence modelled the three-dimensional motion of a flagellum near a plane wall using more detailed hydrodynamic descriptions, and have been able to qualitatively capture various near-wall phenomena observed in experiments, such as the tendency of sperm to accumulate at walls, adhere to walls and swim in circular trajectories near the wall. Smith et al. (2009a) used a hybrid slender-body theory (SBT) approach to study the surface accumulation behaviour of model sperm with planar and three-dimensional waveforms prescribed in the body frame. They reported two main regimes of motion depending on beating wavenumber and initial angle of orientation - accumulation of the cell at a finite distance from the wall, and 'escape' from the wall after initially swimming towards it. Complementarily, Elgeti et al. (2010) used multi-particle collision dynamics (MPC) to simulate the motion of model sperm driven by time-varying preferred curvature. They studied motion very close to the wall, at distances where SBT approaches would no longer be valid (Smith et al., 2009a), and reported that hydrodynamic interactions could be the mechanism behind adhesion of sperm to walls. They also report the emergence of circular trajectories near the wall for model sperm with an intrinsically asymmetric shape, but do not observe swimming at a finite distance from the wall (Smith et al., 2011; Elgeti et al., 2011). It was, however, later shown by Ishimoto and Gaffney (2014) using high-accuracy boundary element method (BEM) simulations that stable swimming at finite distances from the wall persists over a very wide range of head morphologies and beat wavenumbers, although it is predicted to be unstable for certain head morphologies and for swimmers with beat patterns resembling that of hyperactivated sperm, i.e. low wavenumber, large beat amplitude and asymmetry in the waveform. The height above the wall at which the sperm accumulate is predicted to depend on the beating wavenumber, as concluded earlier by Smith et al. (2009a) for a limited set of parameters, although it was demonstrated that quantitative differences arise when using the hybrid SBT of Smith et al. (2009a). Further explorations by Xu et al. (2018) that solve the full Navier-Stokes equations for a periodically-driven headless filament report stable finite-distance accumulation for asymmetric driving waves over a wide range of parameters, with the accumulation height varying with driving asymmetry and time period, bending stiffness of the filament and fluid viscosity.

While studies thus far have focused on the swimming trajectory near walls, the hydrodynamic effect of the wall on beating waveforms is not well-explored, and would provide insight into the origins of the slither

transition. In this Chapter, the motion of an IDKR is simulated near a plane wall with the aim of observing how each of the four qualitative types of beat patterns presented in Chapter 4 changes near the wall. The focus here is on the overall swimming trajectory and changes in the beat waveform. The model and methods used are the same as in Chapter 4, except that the hydrodynamic effects of the wall are now included into the hydrodynamic model as described in Chapter 3. The filament is kept headless as the aim is to capture qualitative changes in beating waveform; previous studies investigating the role of head geometry on surface accumulation behaviour conclude that it does not produce large qualitative changes (Elgeti et al., 2011; Ishimoto and Gaffney, 2014). On the other hand, this would also mean that our results can be extended to isolated axonemes, which have also been shown to follow boundaries (Mojiri et al., 2021). Just as in Chapter 4, the filament is force- and torque-free, and the driving is dependent only on the filament's internal configuration or body frame. This ensures the broad applicability of these results to natural internally-driven filaments. The full nonlinear dynamics of the filament are considered, and the importance of long-range hydrodynamic interactions are investigated in the context of beat pattern changes near walls. Finally, limitations of the hydrodynamic model are discussed and suggestions are provided for future explorations.

7.2 Effect of a Wall on Planar Beat Patterns

We first consider two sets of parameters at which the beating is planar in free space. The first is at dimensionless frequency $S = 9$, and the second is at $S = 7$. Both swimmers have a dimensionless amplitude of $A = 12$ and dimensionless wavenumber of $k = 4\pi$. The simulations are initialised with the filament oriented parallel to the wall and positioned 1.5 body-lengths from the wall. The shape of the filament is initially straight. In both cases, the filament starts swimming towards the wall, with a trajectory that exhibits vertical oscillations before stabilising at a constant height above the wall. Figure 7.1 shows the trajectory for $S = 9$. This surface-accumulating behaviour, as discussed before, has been explored extensively in simulation studies; vertical oscillations of the trajectory have also been reported before in Smith et al. (2009a) for accumulating swimmers.

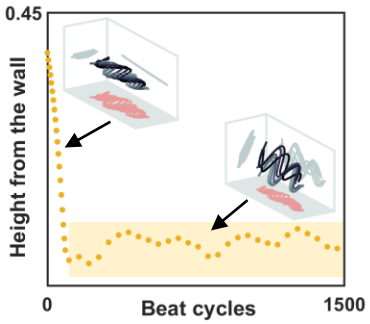

Figure 7.1: Head trajectory of an originally planar swimmer ($S = 9, A = 12, k = 4\pi$) as it swims towards the wall, plotted against time shown in terms of beat cycles; insets show the beat waveform over one beat cycle when the filament is above $0.2L$ (top) and below $0.2L$ (bottom). The yellow highlight corresponds to a height of $0.02 - 0.22L$.

In both cases, the beat is initially planar as described before in the case without the wall, except that the beat plane now develops a slight inclination of approximately 1° towards the wall (top inset of Figure 7.1). For the filament at $S = 7$, the beat remains planar and periodic throughout. This is demonstrated by the overlapping limit cycles in Figure 7.2(c), plotted over hundreds of cycles. The filament at $S = 9$,

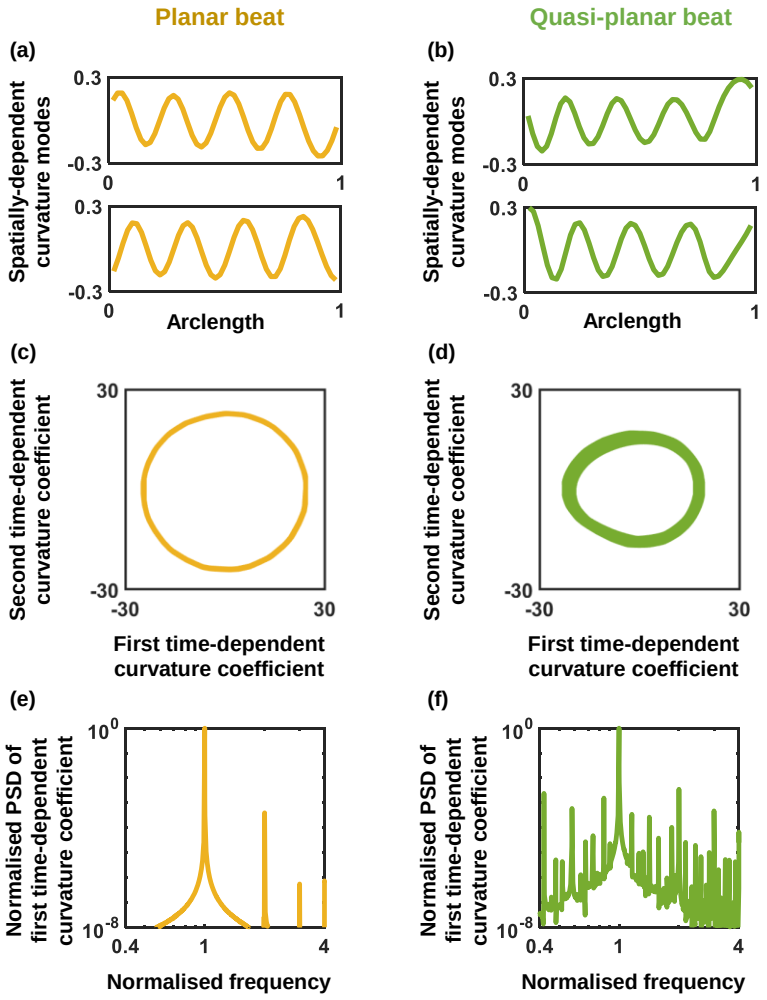

Figure 7.2: (a)-(b) First (top panel) and second (bottom panel) spatially-dependent curvature modes for (a) a planar swimmer at $S = 7$, $A = 12$, $k = 4\pi$, and (b) a quasi-planar swimmer at $S = 9$, $A = 12$, $k = 4\pi$. (b)-(c) Plots of the first time-dependent coefficient of curvature against the second for the same (c) planar swimmer and (d) quasi-planar swimmer. (e)-(f) Normalised power spectral density of the first time-dependent coefficient of curvature plotted against frequencies normalised using the driving frequency, for the same (e) planar swimmer and (f) quasi-planar swimmer.

however, switches to a quasi-planar beat (bottom inset of Figure 7.1) as it reaches a height of approximately $0.2L$ above the wall. The beat plane rolls slightly from one side to another, appearing as though a complete roll has been suppressed. This motion matches the description of quasi-planar swimming in experimental studies of sea urchin sperm (Woolley and Vernon, 2001). Figure 7.3 compares the evolution of centerline torsion in rolling-planar and quasi-planar beats for 6 beat cycles. We note that the centerline torsion of the quasi-planar beat exhibits jumps in a similar manner to the rolling-planar beat (Chapter 4, Figure 4.10), and

additionally shows variations occurring every few beat cycles. In the rolling-planar beat, the direction of the roll always remains the same and the torsion is always negative. Meanwhile the rolling direction in quasi-planar beats keeps alternating – this is captured in the torsion kymograph. Figure 7.2 provides a quantitative comparison of the planar and quasi-planar beat, in terms of the spatial and time-dependent components of curvature. The 'bands' in the limit cycle in Figure 7.2(d) demonstrate that the beat does not exactly repeat every cycle. Comparing Figures 7.2(e) and (f), we observe that the quasi-planar beat is more complex than the planar beat and exhibits sub-harmonic frequency responses, as we also observe in the corresponding torsion kymograph in Figure 7.3.

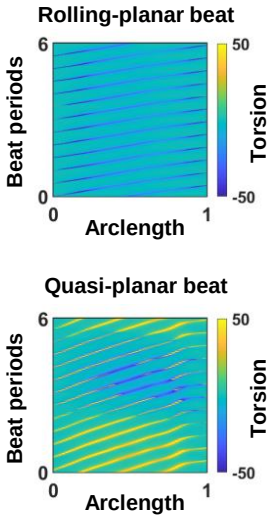

Figure 7.3: Torsion of the centerline over 6 beat cycles in a rolling-planar swimmer at $S = 7$, $A = 18$, $k = 2\pi$ (top) and quasi-planar swimmer at $S = 9$, $A = 12$, $k = 4\pi$ (bottom).

We note that this is the first simulation evidence of a transition from planar to quasi-planar beating (as described in experiments) above the wall. A previous study (Huang et al., 2018) reported small out-of-plane deviations in planar filaments near a wall, but the details of those waveform changes are not described. Furthermore, they report that this is not seen in filaments whose beat plane is parallel to the wall, which is the case in our simulations. To investigate the emergence of the quasi-planar beat, the simulations are repeated using the wall-RFT model of Katz et al. (1975). We find that the filament does not swim towards the wall or change its beat pattern. This is indicated by the trajectory and limit cycle plots in Figure 7.4 for a swimmer initialised at 0.3 body-lengths above the wall. We may hence conclude that accumulation as well as the transition to a quasi-planar beat must involve the effects of long-range hydrodynamic interactions.

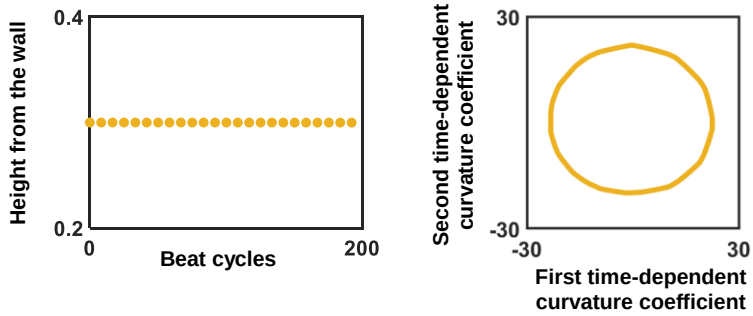

Figure 7.4: Near-wall behaviour of a planar swimmer simulated using local drag theory, at a parameter set where a beat transition is observed in simulations considering long-range HI. Left: Head trajectory of the planar filament ($S = 9, A = 12, k = 4\pi$) as it swims above the wall, plotted against time shown in terms of beat cycles. Right: Plot over 200 beat cycles of the first time-dependent coefficient of curvature against the second.

Another example of beat waveform transition is observed at $S = 7$, $A = 18$, $k = 4\pi$, where a beat that was planar in free space begins to

roll even at a distance of $1.5L$ from the wall. This beat, shown in Figure 7.5, resembles the rolling-planar beat and does not accumulate above the wall. The similarity between this beat and the rolling-planar beat (Chapter 4, Figure 4.10) is also captured in its curvature and torsion profiles, shown in Figure 7.6. The emergence of this beat is noteworthy since the rolling-planar beat is not observed at $k = 4\pi$ in free space.

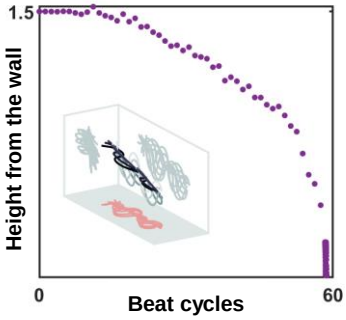

Figure 7.5: Head trajectory of filament at $S = 7$, $A = 18$, $k = 4\pi$ as it swims towards the wall, plotted against time shown in terms of beat cycles; inset shows the beat waveform over one beat cycle. The filament at these parameters is planar in free space but exhibits rolling-planar motion near the wall for all points shown here.

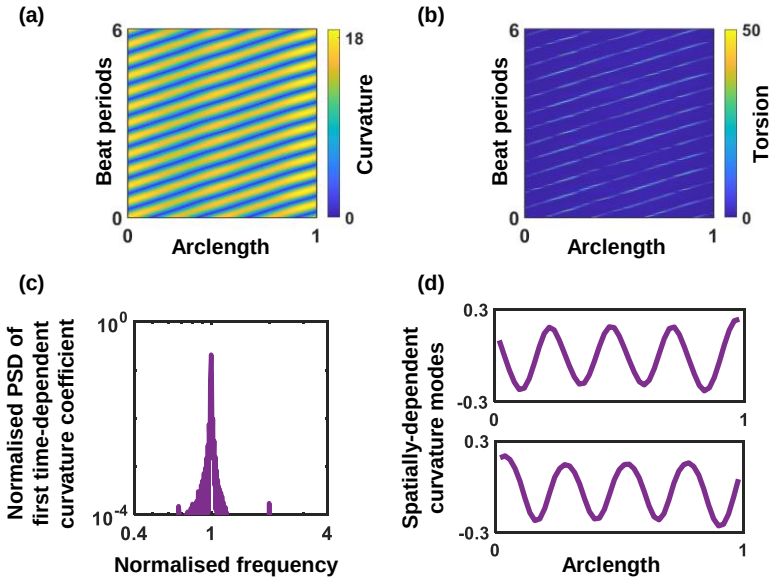

Figure 7.6: (a) Curvature and (b) torsion of the centerline over 6 beat cycles for a rolling swimmer at $S = 7$, $A = 18$, $k = 4\pi$ initially at $1.5L$ above the wall. (c) Normalised power spectral density of the first time-dependent coefficient of curvature for the same swimmer, plotted against frequencies normalised using the driving frequency. (d) First (top panel) and second (bottom panel) spatially-dependent curvature modes for the same swimmer.

The above examples demonstrate that accumulation and beat transition behaviours are sensitive to waveform parameters. We briefly investigate the variation in accumulation height with dimensionless amplitude which, as shown in Chapter 4, changes the beat amplitude when all other parameters are kept constant. Shown in Figure 7.7 is the change in accumulation height with the dimensionless amplitude for two different dimensionless frequencies, $S = 7$ and 8. We observe that the accumulation height decreases with beat amplitude for both dimensionless frequencies. The influence of beat amplitude on accumulation has in general not received much attention, with studies thus far focusing on beat wave number, initial orientation with respect to the wall and head morphology (Smith et al., 2009a; Ishimoto and Gaffney, 2014). In those studies, the beat waveform is kinematically prescribed; such an approach is more suitable for studying the isolated effects of various parameters on the accumulation height. In this study, however, although

the waveform is not prescribed, the waveform remains the same over the duration of our simulations for the points shown in Figure 7.7. The filaments also remain approximately parallel to the wall throughout (inclination towards the wall is in the order of 1°). This hence allows us to draw conclusions about the effects of beat amplitude on accumulation height in an isolated manner.

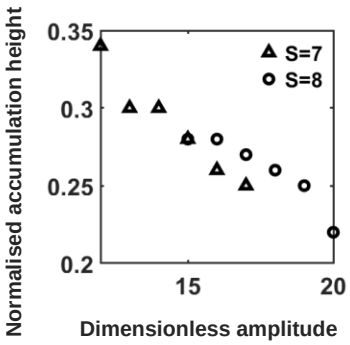

Figure 7.7: Accumulation height above the wall normalised with respect to filament length plotted against the dimensionless driving amplitude, for dimensionless wavenumber of 4π and dimensionless frequency of 7 (triangles) or 8 (circles).

7.3 Effect of a Wall on Three-dimensional Beat Patterns

We now consider helical and rolling-planar filaments near the wall. We do not study complex filaments since it would be difficult to identify waveform changes, and the waveform itself may be very different at different parameters. For numerous parameters considered, helical and rolling-planar filaments initialised at $1.5L$ from the wall appear to maintain their respective waveforms until they crash headfirst into the wall. Shown in Figure 7.8(a) and (b) are trajectories of swimmers at $S = 2, A = 5, k = 2\pi$ (rolling-planar) and $S = 12, A = 21, k = 4\pi$ (helical) respectively. Like planar swimmers, helical and rolling-planar swimmers also have a slight inclination towards the wall, as shown in the insets of Figure 7.8. Looking at the curvature limit cycles in Figures 7.8(e) and (f), we see that the rolling-planar swimmer maintains its waveform exactly throughout, whereas the helical swimmer begins to show signs of a waveform transition beyond $0.32L$ (blue highlight in Figure 7.8(b)). This is indicated by the dotted lines in the limit cycles in Figure 7.8(f), which correspond to the filament's waveform when it is between $0.02 - 0.32L$ above the wall. The spatial curvature modes in that region (dotted lines in Figure 7.8(d)) are also slightly different.

While this transition is not explored further in this work, further investigation may be done in two ways – by looking for parameters and conditions under which the helical swimmer accumulates, or by allowing the filament to swim closer to (and interact with) the wall. A previous simulation study showed that accumulation of swimmers with a prescribed helicoidal wave is possible under certain conditions (Smith et al., 2009a). While their results may not be directly comparable to ours due to the difference in approach, since the helical swimmer in our simulation retains its helical beat as it approaches the wall, it may be possible to obtain situations where the helical swimmer accumulates above the wall with further study on the factors affecting accumulation in our model swimmer. The second option of allowing the swimmer to approach and collide with the wall will require a more accurate hydrodynamic model than the one used in this study – this is discussed in the following section.

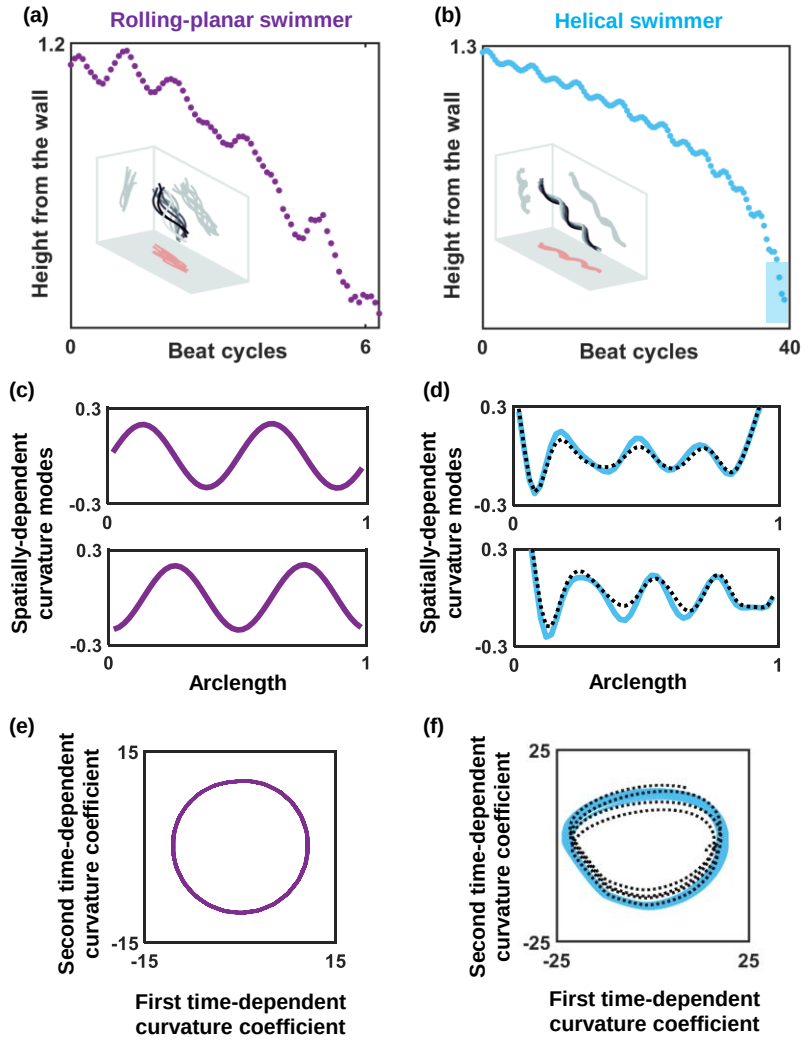

Figure 7.8: (a) Head trajectory of a rolling-planar swimmer ($S = 2, A = 5, k = 2\pi$) as it swims towards the wall, plotted against time shown in terms of beat cycles; inset shows the beat waveform one beat cycle. (c) First (top panel) and second (bottom panel) spatially-dependent curvature modes for the swimmer in (a). (e) Plot over 6 beat cycles of the first time-dependent coefficient of curvature against the second. (b) Head trajectory of a helical swimmer ($S = 12, A = 21, k = 4\pi$) as it swims towards the wall, plotted against time shown in terms of beat cycles; inset shows the beat waveform one beat cycle and the blue highlight corresponds to a height of $0.02 - 0.32L$. (d) First (top panel) and second (bottom panel) spatially-dependent curvature modes for the swimmer in (b); solid lines correspond to the first 38 beat cycles, and dotted lines correspond to the last 2 beat cycles. (f) Plot over the first time-dependent coefficient of curvature against the second; the blue line indicates the first 38 beat cycles and black dotted line shows the last 2 beat cycles, which correspond to the blue highlight in (b).

7.4 Limitations of the Hydrodynamic Model

The data presented thus far is limited to motion beyond a minimum distance from the wall of $2a$, where a is the radius of the filament. As noted by Elgeti et al. (2011), and as demonstrated below, simulating the motion of Stokesian swimmers very close to a wall will require more sophisticated hydrodynamic models which better capture the near-field of the swimmer. Where the filament collides with the wall, one would also need to account for surface interactions; this may not be trivial to model, although approximate models have been used in some studies (Ishimoto and Gaffney, 2015). In this study, however, surface interactions have not been modelled for two reasons. Firstly, the hydrodynamic model itself becomes increasingly inaccurate as the filament approaches the wall. This is demonstrated below using an example involving the application of the Stokesian Dynamics method (Swan and Brady, 2007) used in this study to a slender rod translating parallel to a wall. Secondly, at distances closer than $2a$ from the wall, simulation timesteps are required to be 10–100 times smaller in order to achieve convergence. This is likely due to the very large hydrodynamic forces experienced at such distances, which is also demonstrated in the example.

The aim in this example is to calculate the drag coefficients in the normal, tangential and binormal directions on a slender rod translating parallel to a plane wall as in Ramia et al. (1993), but using the Stokesian Dynamics approach instead of the Boundary Element Method. Here the tangential direction is aligned with the axis of the rod, the normal direction is perpendicular to the wall and the binormal direction is perpendicular to the normal and tangential directions. Drag coefficients are calculated at varying distances from the wall, h for a rod with a length-to-radius aspect ratio of $L/a = 100$. The same problem has partly been considered in Walker et al. (2019) as well; the Regularised Stokeslet Segments (RSS) method was used in that study. The results obtained in this work are compared in Figure 7.9 with the results of both studies.

We observe that the Stokesian Dynamics method provides a good agreement with the more accurate BEM results, and appears to be more accurate than RSS in predicting the binormal drag coefficients for this case. We also observe that the drag coefficients are under-predicted as the rod approaches the wall, with the Stokesian Dynamics results beginning to deviate from the BEM results below $h/L = 0.2$. The normalised tangential drag coefficients (black and magenta dots in Figure 7.9, where black dots represent our results and magenta dots represent BEM results) show an 8% deviation at a normalised height of 0.05 rod-lengths from the wall, i.e. 5 times the rod radius. Meanwhile, the nor-

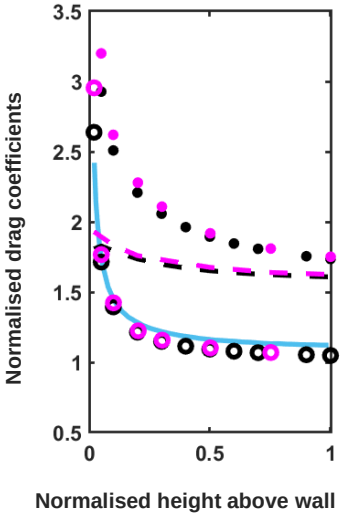

Figure 7.9: Plots of tangential drag coefficient normalised with respect to the free-space tangential drag coefficient (dots), normal drag coefficient normalised with respect to the corresponding tangential drag coefficient (dashes) and binormal drag coefficient normalised with respect to the corresponding tangential drag coefficient (open circles). Black symbols/dashes denote results obtained using our Stokesian Dynamics calculations, pink symbols/dashes denote results obtained by Ramia et al. (1993) (re-plotted with permission) and the blue line denotes results obtained by Walker et al. (2019) (Figure 3 in the paper; licensed under CC BY 4.0) only for the normalised binormal drag coefficients. The horizontal axis corresponds to the distance from the wall h normalised by rod length L.

malised binormal drag coefficients (black and magenta circles in Figure 7.9, where black circles represent our results and magenta circles represent BEM results) show a 10% deviation at a normalised height of 2 times the rod radius, which is the height at which the IDKR simulations are terminated. While these results cannot be used to make direct inferences about the corresponding error magnitudes that can be expected in the IDKR simulations, this example provides an order-of-magnitude estimate of the errors and demonstrates that errors can be expected to increase as the filament moves closer to the wall.

7.5 Chapter Summary

In this Chapter, the behaviour of planar, rolling-planar and helical filaments was studied at distances within 1.5 body-lengths above a plane wall at selected parameters. Changes in beat waveform as well as the overall trajectory were studied.

The results presented here show, for the first time, that filaments with a planar beat pattern in bulk space can exhibit quasi-planar and rolling-planar waveforms above the wall. The quasi-planar beat matches descriptions of quasi-planar beating in sea urchin sperm above a wall; this hence suggests a new elastohydrodynamic mechanism behind the emergence of the quasi-planar beat, which does not involve asymmetries in the structure of the flagellum or in the internal driving. This beat transition was observed at a height of around 0.2 body-lengths above the wall, at which the swimmer accumulated. The rolling-planar beat, on the other hand, emerged at around 1.5 body-lengths from the wall. The swimmer in this case did not accumulate and swam into the wall.

These beat transitions are observed only at a few parameters; the majority of planar swimmers between dimensionless frequencies of $7-9$ and dimensionless amplitudes of $10-20$ do not exhibit beat transitions. It was also found that most of these swimmers accumulate above the wall, with an accumulation height that decreases as the dimensionless amplitude is increased. This would mean that for a surface-accumulating planar filament, an increase in the beat amplitude can result in a decrease in its accumulation height. This finding extends previous work studying the factors affecting surface accumulation and accumulation height, which focused on beat wavenumber, initial orientation with respect to the wall and head morphology. It must be noted, however, that the absence of a sperm head in the model used in this work is likely to introduce quantitative differences; this may be a subject of future investigation.

In the case of rolling-planar swimmers swimming above a wall, the beat pattern is maintained exactly until the filament swims into the wall. Helical swimmers maintain their waveforms up to a distance of about 0.3 body-lengths above the wall, beyond which the waveform begins to change. We were, however, unable to investigate this beat transition further as the filament swam into the wall. The simulations in this work were limited to motion above a minimum distance of twice the filament radius from the wall, since the hydrodynamic model used becomes increasingly inaccurate as the filament approaches the wall. This was demonstrated by calculating the drag coefficients of a slender rigid rod at varying heights above the wall, and comparing it to more accurate BEM results in the literature.

Future investigations into helical beat transitions may be performed by looking for conditions under which the helical swimmer accumulates, or by implementing more accurate hydrodynamic models and allowing the filament to swim closer to the wall.

8

Modelling Flagella with Mechanically-regulated Axonemes

8.1 Introduction

Thus far in this work, flagellar beat transitions have been studied in fluids of different viscosities and in the presence of a plane wall by modelling flagella as Internally-driven Kirchhoff Rods. The results presented showed that beat transitions such as those observed in sperm can be achieved via purely elastohydrodynamic mechanisms. This finding presents an opportunity for future studies to address a fundamental problem – the yet-unknown nature of the axonemal regulation.

As discussed in Chapter 2, there are currently two main alternative schools of thought regarding how dynein motors may be regulated to generate beating motions in flagella. The first is that the activity of the dynein motors is coupled to the motion of the flagellum or to reaction forces exerted by the passive parts of the flagellum. Models based on this hypothesis have predicted spontaneous oscillations of the filament due to mechanical instabilities, as discussed in Chapter 2. The second possibility is that the dynein motors are controlled via biochemical reactions which may be decoupled from the motion or forces within the flagellum. The IDKR simulations presented in the previous chapters, which consider a predetermined internal driving, could be thought of as predictions of the second hypothesis for variations in beating patterns with viscosity or in the presence of walls. Although the predictions appear to agree qualitatively with experiments, it may be of interest to explore the predictions of models corresponding to the first hypothesis. This could provide a way to distinguish between the different hypotheses.

When modelling a mechanically-regulated axoneme, however, the Internally-driven Kirchhoff Rod model cannot be used. This is because a fundamental aspect of the working of the axoneme are *shear deformations*, which originate in the axoneme when adjacent microtubule doublets 'slide' past each other under the action of active dynein motors

(Figure 8.1). This motion forms the basis of various axoneme models in the literature (Lindemann and Lesich, 2010), which attempt to explain how the dynein motors (and hence, the sliding motion itself) is regulated. As discussed in Chapter 2, three main modes of mechanical regulation have been hypothesised – sliding control, curvature control, and normal-force-control – and spontaneous oscillations have been obtained using all three models.

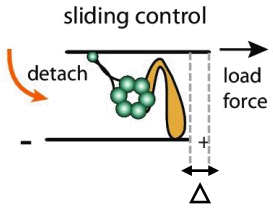

Figure 8.1: Sliding of microtubule doublets (black lines at the top and bottom) past each other due to the action of a dynein motor (structure in the center). Dotted lines show the sliding displacement, Δ. This image has been taken from Figure 1D in Sartori et al. (2016b) (licensed under CC BY 4.0) and has been edited to show the sliding displacement.

Since there is still no universally-accepted model, we begin with a general mechanically-regulated model for the active force $\mathbf{f^a}$ inspired by previous studies (Camalet and Jülicher, 2000; Riedel-Kruse et al., 2007; Sartori et al., 2016b):

$$\mathbf{f^a} + \alpha \frac{\partial \mathbf{f^a}}{\partial t} = \beta \Delta + \gamma \frac{\partial \Delta}{\partial t},$$

where Δ represents the sliding displacement (Figure 8.1) and α, β and γ are parameters. In this model, the active force which causes sliding is assumed to depend on the sliding displacement between the adjacent microtubules. Further details are provided in the next section.

Studies commonly model the axoneme in two dimensions as a system of two parallel elastic rods experiencing an 'effective shear force' which consists of passive and active components (Camalet and Jülicher, 2000; Riedel-Kruse et al., 2007; Sartori et al., 2016b; Chakrabarti and Saintillan, 2019a). In these models, the sliding displacement, i.e the shear displacement between adjacent filaments is related to the integral of the centerline curvature. Studies have extended this approach to three-dimensional axonemes by considering the presence of nine doublets which can slide relative to each other (Sartori et al., 2016a; Hilfinger and Jülicher, 2008; Rallabandi et al., 2022). While this approach may be convenient when modelling axonemes alone, it may be difficult to integrate these models into an overall description of a flagellum based on current models, which treat the flagellum as an unshearable filament. The aforementioned three-dimensional models consider sliding or shear displacements between individual filaments but neglect shearing of the cross sections of the overall ensemble.

A more general framework would be to model the entire flagellum as a shearable rod – this can be done using Cosserat rod theory (Antman, 1973), which accounts for passive shear through the constitutive relations of the flagellar material. The Cosserat rod is allowed three types of deformations – bending (or twisting), stretching and shearing. For a flagellum, however, stretching would be undesirable. In this work, the three-dimensional Cosserat rod model is hence adapted to restrict stretching, such that we now have a general three-dimensional model

of the flagellum which would allow only bending and shear. Like in previous studies, the axoneme is modelled as a two-microtubule system and its geometry is described within the framework of the inextensible Cosserat rod.

The following Section provides the governing equations of the model and outlines the differences between this model and the IDKR model used thus far. Following this, a numerical method is suggested to solve the system of equations. This can be implemented in future simulations.

8.2 Governing Equations

Geometry and Material Frame

This Section introduces the model for a shearable but inextensible flagellum, which is inspired by the work of Gazzola et al. (2018). As in the IDKR model, we would first like to describe the position of every material point in the flagellum relative to its centerline, whose material coordinates are denoted by the arclength parameter s. In an inextensible filament, the centerline may be composed of any set of material points which have a fixed distance between them, so that the length of the centerline always remains constant. As before, the position of the local material frame at every point s is defined by a position vector $\mathbf{r}(s,t)$ and its orientation is described by the orthonormal triad of unit vectors, $\mathbf{d_1}$, $\mathbf{d_2}$ and $\mathbf{d_3}$. The vector $\mathbf{d_1}$ is perpendicular to the cross section while $\mathbf{d_2}$ and $\mathbf{d_3}$ lie on the plane of the cross section.

In the Kirchhoff rod model, the movement of the material is restricted so that material cross sections at any point s along the centerline always remain perpendicular to the centerline. Mathematically, this is expressed as $\mathbf{t} = \mathbf{d_1}$, i.e. the vector $\mathbf{d_1}$ which is perpendicular to the plane of the cross section must be aligned with the tangent vector to the centerline, $\mathbf{t} = \partial\mathbf{r}/\partial s$. Removing this condition allows the material to shear, i.e. cross-sectional planes may now be oriented in any manner with respect to the centerline.

For a rod with no intrinsic shear, the shear strain for small deformations is obtained as the deviation of the $\mathbf{d_1}$ vector from the centerline tangent:

$$\boldsymbol{\sigma} = \mathbf{t} - \mathbf{d_1}. \tag{8.1}$$

As in the IDKR model, the evolution of material frame vectors $\mathbf{d_a}$ with s is described through the rotation vector $\boldsymbol{\Omega}$, and the time rate of change of the material frame vectors is represented using the angular velocity

$\boldsymbol{\omega}$:

$$\frac{\partial \mathbf{d_a}}{\partial s} = \boldsymbol{\Omega} \times \mathbf{d_a}, \tag{8.2}$$

$$\frac{\partial \mathbf{d_a}}{\partial t} = \boldsymbol{\omega} \times \mathbf{d_a}. \tag{8.3}$$

Here $\boldsymbol{\Omega}$ is defined as before in Chapter 3 and represents bending and twisting strains. Additionally, we now define another rotation rate $\boldsymbol{\Theta}$ describing the time rate of change of the tangent:

$$\frac{\partial \mathbf{t}}{\partial t} = \boldsymbol{\Theta} \times \mathbf{t}. \tag{8.4}$$

This definition will aid the numerical implementation of the model, as will be described in the next section. For the same reason, $\boldsymbol{\Theta}$ is expressed in the corresponding orthonormal frame of vectors $\{\mathbf{t}, \mathbf{n}, \mathbf{b}\}$ as

$$\boldsymbol{\Theta} = \Theta_t \mathbf{t} + \Theta_n \mathbf{n} + \Theta_b \mathbf{b},$$

where the normal and binormal vectors $\mathbf{n}$ and $\mathbf{b}$ are defined as

$$\mathbf{n} = \frac{(\mathbf{t} \times \mathbf{d_2}) \times \mathbf{t}}{|\mathbf{t} \times \mathbf{d_2}|}, \tag{8.5}$$

$$\mathbf{b} = \mathbf{t} \times \mathbf{n}. \tag{8.6}$$

Since only the components of $\boldsymbol{\Theta}$ perpendicular to $\mathbf{t}$ are needed in (8.4), we may set $\Theta_t = 0$, without any loss of generality. We note that the above definition of the normal vector has been chosen to aid the description of the active moment, as will be explained in a later subsection.

Kinematics and Conservation Laws

Cross sections are once again assumed to be rigid and circular. The motion of a cross-sectional segment of infinitesimal thickness Δs positioned at $\mathbf{r}$ is described by its linear velocity $\mathbf{v}$ and angular velocity $\boldsymbol{\omega}$. The angular velocity describes the rate of rotation of the material frame (Equation (8.3)), and the linear velocity describes the rate at which the segment position vector changes:

$$\frac{\partial \mathbf{r}}{\partial t} = \mathbf{v}, \tag{8.7}$$

$$\frac{\partial \mathbf{d_a}}{\partial t} = \boldsymbol{\omega} \times \mathbf{d_a}. \tag{8.8}$$

The filament experiences hydrodynamic stresses from the surrounding fluid, passive internal stresses that resist bending, stretching and shearing, and active stresses from the 'axoneme'. Linear and angular momentum balances hence remain unchanged, and are expressed as

$$\mathbf{f^h} + \mathbf{f^s} + \frac{\partial \mathbf{F}}{\partial s} = 0, \tag{8.9}$$

$$\mathbf{m^h} + \mathbf{m^a} + \frac{\partial \mathbf{M}}{\partial s} + \mathbf{t} \times \mathbf{F} = 0, \tag{8.10}$$

where $\mathbf{f^h}$ and $\mathbf{m^h}$ are the hydrodynamic force and moment per unit length, $\mathbf{F}$ and $\mathbf{M}$ are the passive internal force and moment, $\mathbf{m^a}$ is the active moment density and $\mathbf{f^s}$ is the steric force per unit length.

Constitutive Model for Passive Internal Stresses

The restoring elastic internal moment for a filament with no intrinsic curvature is once again expressed as

$$\mathbf{M} = \mathbf{K} \cdot \boldsymbol{\Omega}, \tag{8.11}$$

where $\mathbf{K}$ is a diagonal matrix containing the stiffness coefficients.

The passive internal force opposes stretching as well as shear, so that

$$\mathbf{F} = \mathbf{S} \cdot \boldsymbol{\sigma} + T\mathbf{t}, \tag{8.12}$$

where $\mathbf{S}$ is a diagonal matrix containing the shear stiffness coefficients and T is the tension that enforces the inextensibility constraint. Here we have assumed a linear stress-strain constitutive relationship, as with the elastic internal moment. We note that in the IDKR model, the shear components of the internal force $\mathbf{F}$ enforced the no-shear constraint.

In order to close this system of equations, constitutive relations are needed for the hydrodynamic force and moment, active moment and steric forces. We recall that the hydrodynamic force and moment are related to the linear and angular velocities as follows (see Chapter 3 for details):

$$\begin{bmatrix} \mathbf{v}(s,t) \\ \boldsymbol{\omega}(s,t) \end{bmatrix} = \int_0^L \begin{bmatrix} \boldsymbol{\mathcal{M}}^{\mathrm{tt}} & \boldsymbol{\mathcal{M}}^{\mathrm{tr}} \\ \boldsymbol{\mathcal{M}}^{\mathrm{rt}} & \boldsymbol{\mathcal{M}}^{\mathrm{rr}} \end{bmatrix} \cdot \begin{bmatrix} \mathbf{f^h}(s',t) \\ \mathbf{m^h}(s',t) \end{bmatrix} ds', \tag{8.13}$$

where $\boldsymbol{\mathcal{M}}^{\mathrm{tt}}$, $\boldsymbol{\mathcal{M}}^{\mathrm{rr}}$ and $\boldsymbol{\mathcal{M}}^{\mathrm{tr}}$ and $\boldsymbol{\mathcal{M}}^{\mathrm{rt}}$ are hydrodynamic mobility matrices. The mobility matrices and steric force relations remain unchanged from those provided in Chapter 3 Section 3.1. Here only the mechanically-regulated active moment is described.

Model for Active Moment

The form of the active moment will depend on the assumed geometry of the 'axoneme'. As with the IDKR model, all elements of the axoneme are treated as part of the control volume, except for the active force-generating dynein motors. We use the simple two-doublet arrangement used in previous studies (Camalet and Jülicher, 2000; Riedel-Kruse et al.,

2007; Sartori et al., 2016b), except that the two microtubules are now embedded in a three-dimensional flagellum, as shown in Figure 8.2. The flagellum (containing passive elements of the axoneme) is treated as a homogeneous elastic filament which deforms as a whole. The shaded circular plane in the figure represents a material cross section at an arbitrary s which also contains cross sections of the microtubule doublets marked A and B. Without loss of generality, the positions of doublets A and B at each cross section can be expressed as

$$\mathbf{R}_{\mathrm{A}}(s,t) = \mathbf{r}(s,t) - \frac{a_t}{2}\,\mathbf{d_2}(s,t),$$
$$\mathbf{R}_{\mathrm{B}}(s,t) = \mathbf{r}(s,t) + \frac{a_t}{2}\,\mathbf{d_2}(s,t),$$

where a_t is the diameter of the axoneme. The doublets are also assumed to be inextensible; hence, the total arclengths up to the points on the doublets that coincide with a material cross section (black lines in the figure) are equal.

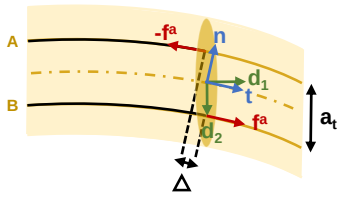

Figure 8.2: Section of the model flagellum containing two doublets (solid lines marked A and B) oriented parallel to the centerline (dashed-dotted line). Shaded circle depicts a single material cross section at a point s along the centerline. Orientations of material frame vectors $\mathbf{d_1}$ and $\mathbf{d_2}$, tangent $\mathbf{t}$ and normal $\mathbf{n}$ at s are shown using arrows. The active forces $\mathbf{f^a}$ experienced by the cross section are shown using the red arrows.

The force exerted by the dynein motors are assumed to act along the centerline tangent $\mathbf{t}$, with the force at $\mathbf{R}_{\mathrm{A}}$ being equal and opposite to that at $\mathbf{R}_{\mathrm{B}}$ (red arrows in the figure). Hence, each cross section experiences no net force and only a net moment,

$$\mathbf{m^a} \;=\; (\mathbf{R}_{\mathrm{A}} - \mathbf{r}) \times -\mathbf{f^a} + (\mathbf{R}_{\mathrm{B}} - \mathbf{r}) \times \mathbf{f^a} \;=\; a_t \mathbf{f^a} \times \mathbf{d_2}, \qquad (8.14)$$

where $\mathbf{f^a} = f^a\mathbf{t}$. As in the IDKR model, for ease of implementing force- and torque-free boundary conditions we define

$$\frac{\partial \mathbf{M^a}}{\partial s} = \mathbf{m^a}.$$

Inspired by the ideas of (Camalet and Jülicher, 2000; Riedel-Kruse et al., 2007), f^a is assumed to be controlled by the sliding displacement Δ. In the language of control systems theory, if f^a is proportional to Δ, we have proportional control. On the other hand, if it is proportional to $\partial\Delta/\partial t$, the regulation is differential whereas if f^a is proportional to $\int_{-\infty}^{t} \Delta\, dt'$, the regulation is integral. In general, a linear Proportional-Integral-Differential (PID) model for regulation of f^a by Δ can be written as:

$$f^a + \alpha\frac{\partial f^a}{\partial t} = \beta\Delta + \gamma\frac{\partial \Delta}{\partial t}. \qquad (8.15)$$

Estimates for the coefficients α, β and γ can be obtained through comparisons with models such as in Camalet and Jülicher (2000) which incorporate details of the dynein motor kinetics. In a periodic beating state, if the equation is Fourier-transformed, we obtain

$$\tilde{f}^a + i\tilde{\omega}\alpha\tilde{f}^a = \beta\tilde{\Delta} + i\gamma\tilde{\omega}\tilde{\Delta},$$

where $\tilde{\omega}$ is the angular frequency. This can be rearranged to obtain the following form which can be compared to the expressions provided in the literature (Camalet and Jülicher, 2000; Riedel-Kruse et al., 2007):

$$\tilde{f}^a = \left[\frac{(\beta + \alpha\gamma\tilde{\omega}^2) + i\tilde{\omega}(\gamma - \alpha)}{(1 + \alpha^2\tilde{\omega}^2)}\right]\tilde{\Delta}.$$

Alternatively, the expressions in previous studies can be recast as differential equations comparable to (8.15) through an inverse Fourier transform. This would allow the integration of motor kinetics into the model.

The sliding displacement Δ (shown in Figure 8.2) is defined as

$$\Delta(s) = \Delta_0 + \int_0^s a_t \mathbf{n} \cdot d\boldsymbol{\sigma}\ ds', \tag{8.16}$$

where $\boldsymbol{\sigma}$ is the shear strain vector defined in (8.1), Δ_0 is the sliding displacement at $s = 0$ (basal sliding) and the normal vector $\mathbf{n}$ is chosen to be parallel to $\mathbf{t}$ and lie in the plane of $\mathbf{d_2}$ and $\mathbf{t}$:

$$\mathbf{n} = \frac{(\mathbf{t} \times \mathbf{d_2}) \times \mathbf{t}}{|\mathbf{t} \times \mathbf{d_2}|},$$

since the doublets lie along the $\mathbf{d_2}$ direction. For simplicity we could set $\Delta_0 = 0$, or model it further.

This completes the set of equations. The boundary conditions for a force- and torque-free filament are specified as $\mathbf{F}|_{s=L} = \mathbf{F}|_{s=0} = 0$, and $(\mathbf{M^a} + \mathbf{M})\,|_{s=L} = (\mathbf{M^a} + \mathbf{M})\,|_{s=0} = 0$.

8.3 Numerical Method

In this Section, an adaptation of the numerical method described in Chapter 3 is proposed for this new system of equations. The main difference between the current and previous systems of equations is the requirement to update $\mathbf{t}$ as well as $\mathbf{d_1}$ which are no longer equal. Summarising the system of equations, we have:

$$\begin{aligned}
&\frac{\mathrm{d}\mathbf{r_n}}{\mathrm{d}t} = \mathbf{v_n},\\
&\frac{\mathrm{d}\mathbf{d_{1,n}}}{\mathrm{d}t} = \boldsymbol{\omega_n} \times \mathbf{d_{1,n}},\\
&\frac{\mathrm{d}\mathbf{d_{2,n}}}{\mathrm{d}t} = \boldsymbol{\omega_n} \times \mathbf{d_{2,n}},\\
&\mathbf{d_{3,n}} = \mathbf{d_{1,n}} \times \mathbf{d_{2,n}},\\
&\frac{\mathrm{d}\mathbf{r_n}}{\mathrm{d}s} = \mathbf{t_n},
\end{aligned}$$

$$\frac{\mathrm{d}\mathbf{r_n}}{\mathrm{d}s} = \mathbf{t_n},$$
$$\mathbf{n_n} = \frac{(\mathbf{t_n} \times \mathbf{d_{2,n}}) \times \mathbf{t_n}}{|\mathbf{t_n} \times \mathbf{d_{2,n}}|},$$
$$\mathbf{b_n} = \mathbf{t_n} \times \mathbf{n_n},$$
$$\frac{\partial \mathbf{t_{n+\frac{1}{2}}}}{\partial t} = \mathbf{\Theta_{n+\frac{1}{2}}} \times \mathbf{t_{n+\frac{1}{2}}}.$$

Here the subscript n denotes the segment index. We note that the tangent vector is only required at intermediate positions between segments, which are denoted as $n + \frac{1}{2}$. As mentioned in Chapter 3, $\mathbf{v}$ and $\boldsymbol{\omega}$ can be expressed in terms of hydrodynamic forces and moments on each segment, which are in turn expressed in terms of all other forces and moments acting on the segment using the force and moment balances.

We saw in Chapter 3 that updating the material frame vectors is more easily performed by instead updating a set of Lie Algebra elements, which are denoted here as $\hat{\mathbf{u}}_{\mathbf{1,n}}$:

$$\frac{\mathrm{d}\hat{\mathbf{u}}_{\mathbf{1,n}}}{\mathrm{d}t} = \mathrm{dexp}^{-1}_{\hat{u}_{1,n}}(\boldsymbol{\omega_n}). \tag{8.17}$$

In a similar manner, we use another set of Lie Algebra elements $\hat{\mathbf{u}}_{\mathbf{2,n}}$ for the tangent vectors so that the tangent update equation is replaced with

$$\frac{\mathrm{d}\hat{\mathbf{u}}_{\mathbf{2,n}}}{\mathrm{d}t} = \mathrm{dexp}^{-1}_{\hat{u}_{2,n}}(\mathbf{\Theta_n}). \tag{8.18}$$

The associated quaternions are obtained as

$$\tilde{\mathbf{q}}_{\mathbf{1,n}}(t + \Delta t) = \exp(\hat{\mathbf{u}}_{\mathbf{1,n}}(t + \Delta t) \cdot \tilde{\mathbf{q}}_{\mathbf{1,n}}(t)), \tag{8.19}$$
$$\tilde{\mathbf{q}}_{\mathbf{2,n}}(t + \Delta t) = \exp(\hat{\mathbf{u}}_{\mathbf{2,n}}(t + \Delta t) \cdot \tilde{\mathbf{q}}_{\mathbf{2,n}}(t)). \tag{8.20}$$

The quaternions are used to calculate the tangent and material frame vectors:

$$\mathbf{d_1} = \mathbf{R}(\tilde{\mathbf{q}}_\mathbf{1})\ \mathbf{e_x}, \tag{8.21}$$
$$\mathbf{d_2} = \mathbf{R}(\tilde{\mathbf{q}}_\mathbf{1})\ \mathbf{e_y}, \tag{8.22}$$
$$\mathbf{d_3} = \mathbf{R}(\tilde{\mathbf{q}}_\mathbf{1})\ \mathbf{e_z}, \tag{8.23}$$
$$\mathbf{t} = \mathbf{R}(\tilde{\mathbf{q}}_\mathbf{2})\ \mathbf{e_x}, \tag{8.24}$$

where $\mathbf{R}(\tilde{\mathbf{q}})$ represents the quaternion rotation matrix associated with a quaternion $\tilde{\mathbf{q}}$ (see Appendix 10.2).

Applying second-order backward differencing in time, the discretised

system of equations now reads

$$\mathbf{r_1^{t+1}} - \frac{4}{3}\mathbf{r_1^t} + \frac{1}{3}\mathbf{r_1^{t-1}} - \frac{2\Delta t}{3}\mathbf{v_1^{t+1}} = 0, \tag{8.25}$$

$$\mathbf{u_{1,n}^{t+1}} - \frac{1}{3}\mathbf{u_{1,n}^t} - \frac{2\Delta t}{3}\mathrm{dexp}^{-1}_{u^{t+1}_{1,n}}(\boldsymbol{\omega}_\mathbf{n}^{\mathbf{t+1}}) = 0, \tag{8.26}$$

$$\mathbf{u_{2,n+\frac{1}{2}}^{t+1}} - \frac{1}{3}\mathbf{u_{2,n+\frac{1}{2}}^t} - \frac{2\Delta t}{3}\mathrm{dexp}^{-1}_{u^{t+1}_{2,n+\frac{1}{2}}}(\boldsymbol{\Theta}_{\mathbf{n+\frac{1}{2}}}^{\mathbf{t+1}}) = 0, \tag{8.27}$$

$$\mathbf{r_1^{t+1}} + \frac{\Delta L}{2}\sum\nolimits_{m=2}^{n}\mathbf{t_{m-\frac{1}{2}}^{t+1}} - \frac{4}{3}\mathbf{r_n^t} + \frac{1}{3}\mathbf{r_n^{t-1}} - \frac{2\Delta t}{3}\mathbf{v_n^{t+1}} = 0. \tag{8.28}$$

Note that here the definition of the tangent has been implemented as in Chapter 3:

$$\mathbf{r_n^{t+1}} = \mathbf{r_1^{t+1}} + \frac{\Delta L}{2}\sum_{m=2}^{n}\mathbf{t_{m-\frac{1}{2}}^{t+1}}. \tag{8.29}$$

There are 9N–3 unknowns consisting of $\mathbf{r_1^{t+1}}$ (3 unknowns), $\mathbf{u_{1,n}^{t+1}}$ (3N unknowns), $\mathbf{u_{2,n+\frac{1}{2}}^{t+1}}$ (3N–3 unknowns), $T^{t+1}_{n+\frac{1}{2}}$ (N–1 unknowns), $\Theta^{t+1}_{n,n+\frac{1}{2}}$ (N–1 unknowns) and $\Theta^{t+1}_{b,n+\frac{1}{2}}$ (N–1 unknowns).

The system of equations can now be solved using the same algorithm detailed in Chapter 3, which is summarised in the Figure 8.3 for the current system.

8.4 Chapter Summary

In this chapter, a new method has been described to model flagella whose internal driving is regulated via mechanical feedback. The axoneme is modelled as a system of two microtubule doublets, as in several previous studies, except that this two-doublet system is now embedded within a three-dimensional flagellum. This would hence allow the flagellum to bend, twist and shear in three dimensions.

The geometry of the axoneme is presented within the framework of an inextensible Cosserat rod model. To enable this, the well-known Cosserat rod model was first adapted to suit the current problem by restricting stretching deformations while allowing bending and shear. The advantage of the Cosserat rod approach is that it allows passive shear resistances to be modelled independently of the orientation of the doublets. This allows us to consider shear resistances from various components of the flagellum, and not just the interdoublet links considered in previous studies.

In the spirit of the IDKR model, the control volume is made up of the flagellum and all passive elements of the axoneme, which excludes the

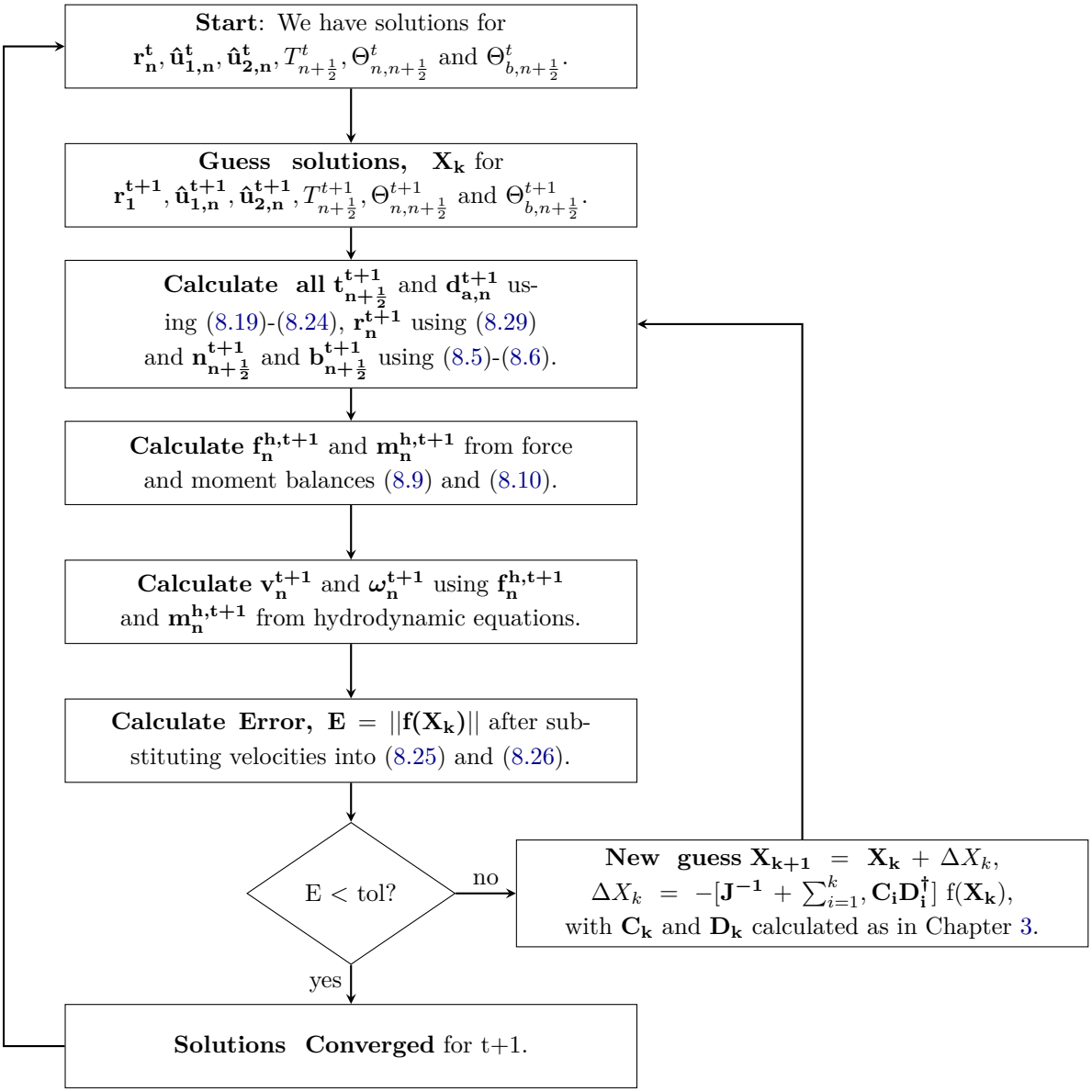

Figure 8.3: Overall algorithm based on bad Broyden's method to solve the system of equations to obtain positions and orientations of all filament segments at each time step.

active dynein motors. The dynein motors exert internal active forces on the control volume, which results in a net active moment at each material cross section. As in previous studies, the forces exerted by the dynein motors are assumed to act longitudinally along the doublets, causing them to slide relative to each other. These active forces in turn depend on the sliding displacement, which has been defined here for the three-dimensional filament. The model can be easily extended to other axoneme geometries and other forms of mechanical regulation, such as

curvature- and normal-force-control.

Finally, a numerical algorithm is described which can be used to solve the system of equations. The suggested technique is an adaptation of the algorithm used in previous chapters, which is based on Bad Broyden's method. Future studies may hence implement this model to explore the role of mechanically-regulated internal driving in shaping flagellar beat patterns in different environments. Based on current results in the literature, spontaneous oscillations should begin to emerge due to instabilities in certain ranges of the axonemal regulation parameters α, β and γ. Simulations could then explore how these oscillations are affected by changes in the environment such as changes in the medium viscosity or the presence of walls, and compare the results obtained with different types of internal driving. Such parallel simulations could suggest experiments that could be used to elucidate the nature of the axonemal regulation.

9
Conclusions

This study has explored the possible elastohydrodynamic origins of flagellar beat transitions of sperm in fluids of different viscosity as well as in the presence of a plane wall. Flagella are modelled as internally-driven, inextensible and unshearable slender elastic filaments (Internally-driven Kirchhoff Rods or IDKRs) suspended in a viscous Newtonian fluid medium. Inspired by experimental observations of the axoneme (Lin and Nicastro, 2018), the internal driving is modelled as a simple sinusoidal wave of active bending moments. This internal driving induces locally-planar bending with respect to the material frame of each cross section, which can itself rotate depending on the emergent shape of the filament.

In the first part of this work, simulations of the motion of the IDKR in quiescent fluids of different viscosities showed that various types of planar and three-dimensional beat patterns emerge. The beat patterns are classified into four major qualitative types comparable to beat patterns in sperm – planar beating, rolling-planar beating, helical beating and more complex beating patterns. The predicted viscosity-related changes in beating patterns qualitatively match those that have been observed in sea urchin and avian sperm, as reported in the literature (Woolley and Vernon, 2001; Vernon and Woolley, 1999). Experimental data of bull sperm swimming in methyl cellulose solutions of different viscosities has also been analysed to compare the beat pattern changes with simulations. Analysis of the three qualitatively different beat patterns exhibited by bull sperm at different viscosities shows that the experimental beat patterns qualitatively match those predicted by the simulations.

This work provides the first simulation evidence that flagellar beat transitions may be purely elastohydrodynamic in nature and may not involve any regulation of the internal driving, as current theories suggest (Lindemann and Lesich, 2021; Woolley, 2003). Furthermore, this work provides the first evidence that three-dimensional beating can emerge from internal driving that produces locally-planar bends, without any

structural or driving asymmetries. The origins of the obtained three-dimensional beats have been explored further by analysing the linear stability of planar base states to shape perturbations. It was found that the linear stability analysis captures the transition from three-dimensional beating to planar beating as dimensionless frequency is increased while the dimensionless amplitude is kept high, but does not predict the transition to planar beating when dimensionless frequency is lowered. This suggests that planar beat patterns at low dimensionless frequencies and high dimensionless amplitudes are stabilised by nonlinear effects. One could begin to verify this by performing a weakly nonlinear stability analysis, which may be the subject of future work. It was also observed that non-local hydrodynamic interactions can qualitatively affect the final form of the beat, especially at parameters where three-dimensional beats are observed.

Simulations have also been used to study how the planar and three-dimensional beat patterns change near a plane wall. At some parameter values, beating patterns that are planar in bulk space accumulate at a fixed distance from the wall and switch to a quasi-planar beat at that height. While accumulation near a wall has been studied before in detail (Smith et al., 2009a; Ishimoto and Gaffney, 2014), this work presents the first evidence that quasi-planar beating such as that seen in sea urchin sperm (Woolley and Vernon, 2001) may emerge from an originally planar beat and not from the 'flattening' of an originally helical beat (Lindemann and Lesich, 2021), or due to any structural asymmetries in the flagellum (Guerrero et al., 2011). However, beat transitions are only observed at a few parameter values, and are a result of long-range hydrodynamic interactions. Meanwhile, filaments with three-dimensional beating patterns are found to maintain their respective waveforms until they nearly collide with the wall. This study is limited to motion above 0.02 body-lengths of the filament (which corresponds to about a few micrometers from the wall) due to limitations of the hydrodynamic model used. Future studies using more sophisticated hydrodynamic models may explore the motion of such filaments much closer to a wall to observe whether beat transitions such as the slither transition (Nosrati et al., 2015) can be captured.

This work has demonstrated, for the first time, qualitative matches in the flagellar beat transitions predicted by simulations and those observed in experiments of sperm. However, since the nature of the axonemal regulation remains unknown, it may be of interest to examine the beat transitions predicted by other models of the axoneme available in the literature. In the final part of this work, a new three-dimensional model is presented for flagella which accounts for the presence of shear

while maintaining inextensibility, and a numerical method is suggested to solve it. This would enable future work to incorporate more detailed models of the axoneme that consider the sliding of microtubule doublets relative to each other. A potential future investigation could explore the role of mechanical-feedback-based regulation of the axoneme in supporting the experimentally-observed beat pattern changes in flagella.

10
Appendices

10.1 The Stokesian Dynamics Method

In this Section we outline the derivation of the Stokesian Dynamics tensors based on the Faxén laws for spherical particles, as in Durlofsky et al. (1987); Swan and Brady (2007). We then discuss an example problem demonstrating the application of this method to spheres above a wall.

Faxén Laws for a Spherical Particle

The generalized Faxén laws provide a relationship between the rigid-body motion of an object and the hydrodynamic forces and torques acting on it. We wish to determine the Faxén relations for a spherical particle translating and rotating in an ambient singularly-forced flow. The following derivation draws upon approaches presented in Pozrikidis (1992) and Kim and Karrila (2005).

We first consider a translating spherical particle. Let $\mathbf{u}^t$ and $\boldsymbol{\sigma}^t$ describe the flow due to the rigid particle translating at velocity $\mathbf{V}$ in a still fluid. Let $\mathbf{u}^d$ and $\boldsymbol{\sigma}^d$ be the disturbance flow due to the same particle translating at velocity $\mathbf{U}$ in an ambient point-force-driven flow $\mathbf{u}_s$, such that $\boldsymbol{\nabla}.\boldsymbol{\sigma}^d = -\mathbf{F}_s\delta(\mathbf{x}-\mathbf{x}_0)$. For these flows, the general form of the Lorentz reciprocal theorem can be written as (Kim and Karrila, 2005)

$$\int_S \mathbf{u}^t \cdot (\boldsymbol{\sigma}^d \cdot \mathbf{n}) dS - \int_V \mathbf{u}^t \cdot (\boldsymbol{\nabla} \cdot \boldsymbol{\sigma}^d) dV = \int_S \mathbf{u}^d \cdot (\boldsymbol{\sigma}^t \cdot \mathbf{n}) dS - \int_V \mathbf{u}^d \cdot (\boldsymbol{\nabla} \cdot \boldsymbol{\sigma}^t) dV, \tag{10.1}$$

where S denotes the surface of the particle and V is the fluid volume which excludes the particle. This now reduces to

$$\mathbf{V} \cdot \mathbf{F}^d + \mathbf{u}^t(\mathbf{x}_0) \cdot \mathbf{F}_s = \mathbf{U} \cdot \mathbf{F}^t, \tag{10.2}$$

where $\mathbf{F}^d$ and $\mathbf{F}^t$ denote the total surface force on the particle due to $\boldsymbol{\sigma}^d$ and $\boldsymbol{\sigma}^t$ respectively, and $\mathbf{F}_s$ is the point force at $\mathbf{x}_0$. We now express

the flow due to the translation of the spherical particle, $\mathbf{u}^t(\mathbf{x}_0)$ as the sum of flows due to a point force and potential doublet located at the center of the sphere, $\mathbf{x}_c$ (Pozrikidis, 1992):

$$\mathbf{u}^t(\mathbf{x}_0) = \mathbf{V} \cdot \left(\frac{3a}{4} + \frac{a^3}{8}\nabla^2 \right) \boldsymbol{\mathcal{G}}(\mathbf{x}_0, \mathbf{x}_c),$$

where a is the radius of the sphere and $\boldsymbol{\mathcal{G}}$ is the velocity Green's function. The corresponding force on the sphere can be expressed as

$$\mathbf{F}^t = \mathbf{V} \cdot \boldsymbol{\mathcal{R}}^t,$$

where the translational resistance matrix for the sphere, $\boldsymbol{\mathcal{R}}^t = 6\pi\mu a\mathbf{I}$. After substituting in these expressions for $\mathbf{u}^t$ and $\mathbf{F}^t$ and simplifying, Equation (10.2) now reads

$$\mathbf{F}^d + \left(\frac{3a}{4} + \frac{a^3}{8}\nabla^2 \right) \boldsymbol{\mathcal{G}}(\mathbf{x}_0, \mathbf{x}_c) \cdot \mathbf{F}_s = 6\pi\mu a\mathbf{U}.$$

But,

$$\boldsymbol{\mathcal{G}}(\mathbf{x}_0, \mathbf{x}_c) \cdot \mathbf{F}_s = \mathbf{F}_s \cdot \boldsymbol{\mathcal{G}}(\mathbf{x}_c, \mathbf{x}_0) = 8\pi\mu\mathbf{u}_s(\mathbf{x}_c),$$

where $\mathbf{u}_s$ represents the velocity of a flow driven by a point force, i.e. a Stokeslet. Noting that the surface force due to the disturbance flow $\mathbf{F}^d$ is equivalent to the total force $\mathbf{F}$ experienced by the sphere, we obtain the desired relation:

$$\mathbf{U} = \frac{\mathbf{F}}{6\pi\mu a} + \left(1 + \frac{a^2}{6}\nabla^2 \right) \mathbf{u}_s(\mathbf{x}_c). \tag{10.3}$$

Now we consider rotation of the particle in the same ambient flow. Let $\mathbf{u}^r$ and $\boldsymbol{\sigma}^r$ describe the flow due to the rigid particle rotating with angular velocity $\boldsymbol{\Omega}$ in a still fluid. Let $\mathbf{u}^d$ and $\boldsymbol{\sigma}^d$ be the disturbance flow due to the same particle rotating with angular velocity $\boldsymbol{\omega}$ in an ambient point-force-driven flow $\mathbf{u}_s$, such that $\boldsymbol{\nabla}.\boldsymbol{\sigma}^d = -\mathbf{F}_s\delta(\mathbf{x} - \mathbf{x}_0)$. For these flows, the Lorentz reciprocal theorem (10.1) now reads:

$$\int_S \mathbf{u}^r \cdot (\boldsymbol{\sigma}^d \cdot \mathbf{n}) dS - \int_V \mathbf{u}^r \cdot (\boldsymbol{\nabla} \cdot \boldsymbol{\sigma}^d) dV = \int_S \mathbf{u}^d \cdot (\boldsymbol{\sigma}^r \cdot \mathbf{n}) dS - \int_V \mathbf{u}^d \cdot (\boldsymbol{\nabla} \cdot \boldsymbol{\sigma}^r) dV. \tag{10.4}$$

Substituting $\mathbf{u}^r = \boldsymbol{\Omega} \times \mathbf{r}$ and rearranging using standard vector operations, we obtain

$$\int_S \boldsymbol{\Omega} \cdot (\mathbf{r} \times \boldsymbol{\sigma}^d \cdot \mathbf{n}) dS - \int_V \mathbf{u}^r \cdot (\boldsymbol{\nabla} \cdot \boldsymbol{\sigma}^d) dV = \int_S \boldsymbol{\omega} \cdot (\mathbf{r} \times \boldsymbol{\sigma}^r \cdot \mathbf{n}) dS - \int_V \mathbf{u}^d \cdot (\boldsymbol{\nabla} \cdot \boldsymbol{\sigma}^r) dV, \tag{10.5}$$

which reduces to

$$\boldsymbol{\Omega} \cdot \mathbf{T}^d + \mathbf{u}^r(\mathbf{x}_0) \cdot \mathbf{F}_s = \boldsymbol{\omega} \cdot \mathbf{T}^r, \tag{10.6}$$

where $\mathbf{T}^d$ and $\mathbf{T}^t$ denote the total surface moment on the particle due to $\boldsymbol{\sigma}^d$ and $\boldsymbol{\sigma}^r$ respectively, and $\mathbf{F}_s$ is the point force at $\mathbf{x}_0$. We now express the flow due to the rotation of the spherical particle, $\mathbf{u}^r(\mathbf{x}_0)$ as the flow due to a rotlet at the center of the sphere, $\mathbf{x}_c$ (Pozrikidis, 1992):

$$\mathbf{u}^r(\mathbf{x}_0) = \boldsymbol{\Omega} \cdot \left(\frac{a^3}{2} \boldsymbol{\nabla} \times \boldsymbol{\mathcal{G}}(\mathbf{x}_0, \mathbf{x}_c) \right).$$

The corresponding torque on the sphere can be expressed as

$$\mathbf{T}^r = \boldsymbol{\Omega} \cdot \boldsymbol{\mathcal{R}}^r,$$

where the translational resistance matrix for the sphere, $\boldsymbol{\mathcal{R}}^r = 8\pi\mu a^3 \mathbf{I}$. After substituting in these expressions for $\mathbf{u}^r$ and $\mathbf{F}^r$ and simplifying, Equation (10.6) now reads

$$\mathbf{T}^d + \frac{a^3}{2} \boldsymbol{\nabla} \times \boldsymbol{\mathcal{G}}(\mathbf{x}_0, \mathbf{x}_c) \cdot \mathbf{F}_s = 8\pi\mu a^3 \boldsymbol{\omega}.$$

Once again we note,

$$\boldsymbol{\mathcal{G}}(\mathbf{x}_0, \mathbf{x}_c) \cdot \mathbf{F}_s = \mathbf{F}_s \cdot \boldsymbol{\mathcal{G}}(\mathbf{x}_c, \mathbf{x}_0) = 8\pi\mu \mathbf{u}_s(\mathbf{x}_c).$$

Since the surface torque due to the disturbance flow, $\mathbf{T}^d$ is equivalent to the total torque experienced by the sphere, we obtain the desired relation:

$$\boldsymbol{\omega} = \frac{\mathbf{T}}{8\pi\mu a^3} + \frac{1}{2} \boldsymbol{\nabla} \times \mathbf{u}_s(\mathbf{x}_c). \tag{10.7}$$

We have thus derived the Faxén laws for the linear and angular velocities of (or conversely, force and torque on) a spherical particle in ambient point-force-driven flow. The same laws can be used for flows driven by higher-order singularities as well.

Derivation of the Stokesian Dynamics tensors

The Stokesian Dynamics tensors are useful for suspensions of rigid spheres in free space as well as in half space. Here we demonstrate how the free-space mobility tensors are derived, which relate the velocity of each sphere to the forces and torques exerted by all spheres. We begin with the Faxén laws for the linear velocity $\mathbf{v}$ and angular velocity $\boldsymbol{\omega}$ of a sphere i of radius a in an ambient singularity-driven flow $\mathbf{u}^\infty$ with viscosity μ, as derived above:

$$\mathbf{v}_i = \frac{\mathbf{F}_i}{6\pi\mu a_i} + \left(1 + \frac{a_i^2}{6} \nabla^2 \right) \mathbf{u}^\infty(\mathbf{x}_c), \tag{10.8}$$

$$\boldsymbol{\omega}_i = \frac{\mathbf{T}_i}{8\pi\mu a_i^3} + \frac{1}{2} \boldsymbol{\nabla} \times \mathbf{u}^\infty(\mathbf{x}_c), \tag{10.9}$$

where $\mathbf{F}$ and $\mathbf{T}$ represent the total force and torque on the sphere. The ambient flow consists of flow driven by all of the remaining spheres j.

This is written as the flow due to the translation and rotation of a sphere j in still fluid, as introduced in the previous section:

$$\mathbf{u}^{\infty}(\mathbf{x}_c) = \sum_j \left(\frac{3a_j}{4} + \frac{a_j^3}{8}\nabla^2 \right) \boldsymbol{\mathcal{G}}(\mathbf{x}_c, \mathbf{x}_j) \cdot \frac{\mathbf{F}_j}{6\pi\mu a_j} + \left(\frac{a_j^3}{2}\nabla \times \boldsymbol{\mathcal{G}}(\mathbf{x}_c, \mathbf{x}_j) \right) \cdot \frac{\mathbf{T}_j}{8\pi\mu a_j^3}.$$

Substituting this into the Faxén laws (10.8) and (10.9) and simplifying yields the desired free-space mobility matrices for spheres of the same radius:

$$\boldsymbol{\mathcal{M}}_{ij}^{F,\mathrm{tt}} = \begin{cases} \dfrac{1}{8\pi\mu\, r}\left[\left(1+\dfrac{2\,a^2}{3\,r^2}\right)\mathbf{I} + \left(1-\dfrac{2\,a^2}{r^2}\right)\hat{\mathbf{x}}\hat{\mathbf{x}}\right] & , \quad i \neq j\,, \\ \dfrac{1}{6\pi\mu\, a}\mathbf{I} & , \quad i = j\,, \end{cases}$$

$$\boldsymbol{\mathcal{M}}_{ij}^{F,\mathrm{tr}} = \boldsymbol{\mathcal{M}}_{ij}^{F,\mathrm{rt}\ \dagger} = \begin{cases} \dfrac{1}{8\pi\mu r^2}\,\boldsymbol{\epsilon}\cdot\hat{\mathbf{x}} & , \quad i \neq j\,, \\ 0 & , \quad i = j\,, \end{cases}$$

$$\boldsymbol{\mathcal{M}}_{ij}^{F,\mathrm{rr}} = \begin{cases} \dfrac{1}{16\pi\mu r^3}\left(3\,\hat{\mathbf{x}}\,\hat{\mathbf{x}} - \mathbf{I}\right) & , \quad i \neq j\,, \\ \dfrac{1}{8\pi\mu a^3}\mathbf{I} & , \quad i = j. \end{cases}$$

where μ is the fluid viscosity, a is the radius of the sphere, $\mathbf{x} = \mathbf{r}_i - \mathbf{r}_j$ for two spheres i and j with position vectors $\mathbf{r}_i$ and $\mathbf{r}_j$, $r = |\mathbf{x}|$, $\hat{\mathbf{x}} = \mathbf{x}/r$, $\mathbf{I}$ represents the identity tensor and $\boldsymbol{\epsilon}$ is the three-dimensional Levi-Civita symbol. The dagger symbol denotes the matrix transpose.

The same procedure can be followed to obtain the mobility matrices near a wall, in which case the ambient flow additionally contains flows induced by the image system (Blake, 1971) of every sphere. For a sphere at a position (x, y, z) above a plane wall at $z = 0$, the image system consists of a set of flow singularities placed at $(x, y, -z)$ which acts to cancel out the flow induced by the sphere at $z = 0$. Since the flow due to a translating and rotating sphere is represented as the sum of a stokeslet (S), potential dipole (PD) and rotlet (R) flow (see previous section), we can represent the image system as a sum of the respective individual image system flows; the total flow is hence represented as

$$\mathbf{u} = \mathbf{u_S} + \mathbf{u_{S,i}} + \mathbf{u_{PD}} + \mathbf{u_{PD,i}} + \mathbf{u_R} + \mathbf{u_{R,i}}, \tag{10.10}$$

where the subscript i indicates flow due to the image system. The image system for a stokeslet of strength $\mathbf{f}$ is represented as follows:

$$\mathbf{u_{S,i}} = -\mathbf{f}\cdot\boldsymbol{\mathcal{G}} + (\mathbf{b}\cdot\boldsymbol{\nabla_o})(\boldsymbol{\mathcal{G}}\cdot\mathbf{e_x}) + \frac{1}{2}h\nabla_o^2(\mathbf{b}\cdot\boldsymbol{\mathcal{G}}),$$

where $\mathbf{b} = 2h(\mathbf{f} - 2f_x\mathbf{e_x})$ and $\boldsymbol{\mathcal{G}}$ is the velocity Green's function defined earlier. Here $\boldsymbol{\nabla_o}$ represents derivation with respect to the position vector of the sphere, $\mathbf{x_o}$ and h represents the $z-$height above the wall.

Similarly the image system for a potential dipole of strength $\mathbf{q}$ and rotlet of strength $\mathbf{t}$ are represented as

$$\mathbf{u_{PD,i}} = \frac{1}{2}\nabla_o^2\boldsymbol{\mathcal{G}}\cdot(\mathbf{q}\cdot(\mathbf{I}-4\mathbf{e_x}\mathbf{e_x})) + h\nabla_o^2(\mathbf{b}\cdot\boldsymbol{\nabla_o})(\boldsymbol{\mathcal{G}}\cdot\mathbf{e_x}) + 2(\mathbf{e_x}\cdot\boldsymbol{\nabla_o})(\mathbf{b}\cdot\boldsymbol{\nabla_o})(\boldsymbol{\mathcal{G}}\cdot\mathbf{e_x}),$$
$$\mathbf{u_{R,i}} = \frac{1}{2}\boldsymbol{\nabla_o}\times(-\mathbf{t}\cdot\boldsymbol{\mathcal{G}}) - h\nabla_o^2(\mathbf{t}\times\mathbf{e_x})\cdot\boldsymbol{\mathcal{G}} - \frac{6}{r_i^5}(\mathbf{e_x}\cdot\hat{\mathbf{x}}_\mathbf{i})\hat{\mathbf{x}}_\mathbf{i}\hat{\mathbf{x}}_\mathbf{i}\cdot(\mathbf{t}\times\mathbf{e_x}),$$

where $\mathbf{b} = \mathbf{q}\cdot(\mathbf{I}-2\mathbf{e_x}\mathbf{e_x})$, $\hat{\mathbf{x}}_\mathbf{i} = \mathbf{x}-\mathbf{x_{o,i}}$ with $\mathbf{x_{o,i}}$ representing the position of the image singularity, $r_i = |\hat{\mathbf{x}}_\mathbf{i}|$ and $\mathbf{I}$ is the identity tensor.

Using this we obtain the following terms of the mobility tensor corresponding to the image systems of all particles:

$$\boldsymbol{\mathcal{M}}_{ij}^{W,\mathrm{tt}} = \begin{cases} \frac{1}{6\pi\mu}\Big[-\frac{3}{4r_i}(\mathbf{I}+\hat{\mathbf{x}}_\mathbf{i}\hat{\mathbf{x}}_\mathbf{i}) + \frac{3h}{2r_i^2}(3\hat{x}_{i,z}\hat{\mathbf{x}}_\mathbf{i}\hat{\mathbf{x}}_\mathbf{i} - \hat{x}_{i,z}\mathbf{I} + \mathbf{e}_z\hat{\mathbf{x}}_\mathbf{i} + \hat{\mathbf{x}}_\mathbf{i}\mathbf{e}_z - 6\hat{x}_{i,z}^2\hat{\mathbf{x}}_\mathbf{i}\mathbf{e}_z) + \\ \quad \frac{3h^2}{2r_i^3}(\mathbf{I}-3\hat{\mathbf{x}}_\mathbf{i}\hat{\mathbf{x}}_\mathbf{i}-2\mathbf{e}_z\mathbf{e}_z+6\hat{x}_{i,z}\hat{\mathbf{x}}_\mathbf{i}\mathbf{e}_z) + \frac{3a^2}{2r_i^3}(\hat{x}_{i,z}^2\mathbf{I} - 2\hat{x}_{i,z}^2\mathbf{e}_z\mathbf{e}_z - 2\hat{x}_{i,z}\hat{\mathbf{x}}_\mathbf{i}\mathbf{e}_z) - \\ \quad \frac{a^2}{2r_i^3}(\mathbf{I}-3\hat{\mathbf{x}}_\mathbf{i}\hat{\mathbf{x}}_\mathbf{i}) - \frac{15a^2}{2r_i^3}(\hat{x}_{i,z}^2\hat{\mathbf{x}}_\mathbf{i}\hat{\mathbf{x}}_\mathbf{i} - 2\hat{x}_{i,z}^3\hat{\mathbf{x}}_\mathbf{i}\mathbf{e}_z) + \frac{a^4}{2r_i^5}(\mathbf{I}-4\mathbf{e}_z\mathbf{e}_z) + \\ \quad \frac{35a^4}{2r_i^5}(\hat{x}_{i,z}^2\hat{\mathbf{x}}_\mathbf{i}\hat{\mathbf{x}}_\mathbf{i} - 2\hat{x}_{i,z}^3\hat{\mathbf{x}}_\mathbf{i}\mathbf{e}_z) - \frac{5a^4}{4r_i^5}(2\hat{\mathbf{x}}_\mathbf{i}\hat{\mathbf{x}}_\mathbf{i} + 4\hat{x}_{i,z}\mathbf{e}_z\hat{\mathbf{x}}_\mathbf{i} - 8\hat{x}_{i,z}\hat{\mathbf{x}}_\mathbf{i}\mathbf{e}_z + 2\hat{x}_{i,z}^2\mathbf{I} - 12\hat{x}_{i,z}^2\mathbf{e}_z\mathbf{e}_z)\Big] & , \ i\neq j\,, \\ \frac{1}{6\pi\mu a}\left[\left(\frac{a^3}{8h^3}-\frac{9a}{16h}-\frac{a^5}{16h^5}\right)(\mathbf{I}+\mathbf{e}_z\mathbf{e}_z) + \frac{2a^3}{8h^3}\mathbf{e}_z\mathbf{e}_z\right] & , \ i=j\,, \end{cases}$$

$$\boldsymbol{\mathcal{M}}_{ij}^{W,\mathrm{rt}} = \boldsymbol{\mathcal{M}}_{ij}^{W,\mathrm{tr}\ \dagger} = \begin{cases} \frac{1}{4\pi\mu}\Big[\frac{h}{r_i^3}(6\hat{x}_{i,z}\mathbf{e}_z\times\hat{\mathbf{x}}_\mathbf{i}\mathbf{e}_z - 3\mathbf{e}_z\times\hat{\mathbf{x}}_\mathbf{i}\hat{\mathbf{x}}_\mathbf{i} - \boldsymbol{\epsilon}\cdot\mathbf{e}_z) + \frac{1}{2r_i^2}(\boldsymbol{\epsilon}\cdot\hat{\mathbf{x}}_\mathbf{i}) - \\ \quad \frac{a^2}{r_i^4}(5\hat{x}_{i,z}\mathbf{e}_z\times\hat{\mathbf{x}}_\mathbf{i}\hat{\mathbf{x}}_\mathbf{i} - 10\hat{x}_{i,z}^2\mathbf{e}_z\times\hat{\mathbf{x}}_\mathbf{i}\mathbf{e}_z + \hat{x}_{i,z}\boldsymbol{\epsilon}\cdot\mathbf{e}_z + \mathbf{e}_z\times\hat{\mathbf{x}}_\mathbf{i}\mathbf{e}_z)\Big] & , \ i\neq j\,, \\ \frac{1}{64\pi\mu}\left(\frac{a^2}{h^2}\boldsymbol{\epsilon}\cdot\mathbf{e}_z\right) & , \ i=j\,, \end{cases}$$

$$\boldsymbol{\mathcal{M}}_{ij}^{W,\mathrm{rr}} = \begin{cases} \frac{1}{16\pi\mu r_i^3}\left(\mathbf{I}-3\hat{\mathbf{x}}_\mathbf{i}\hat{\mathbf{x}}_\mathbf{i} + 6(\mathbf{e}_z\times\hat{\mathbf{x}}_\mathbf{i})(\mathbf{e}_z\times\hat{\mathbf{x}}_\mathbf{i}) + 6\hat{x}_{i,z}\mathbf{e}_z\hat{\mathbf{x}}_\mathbf{i} - 6\hat{x}_{i,z}^2\mathbf{I}\right) & , \ i\neq j\,, \\ \frac{1}{128\pi\mu h^3}(3\mathbf{e}_z\mathbf{e}_z - 5\mathbf{I}) & , \ i=j, \end{cases}$$

so that $\boldsymbol{\mathcal{M}}_{ij}^{\mathrm{xx}} = \boldsymbol{\mathcal{M}}_{ij}^{F,\mathrm{xx}} + \boldsymbol{\mathcal{M}}_{ij}^{W,\mathrm{xx}}$. This is equivalent to the expressions presented in Swan and Brady (2007) for the Force-Torque level of truncation of the multipole expansion.

Application of the Stokesian Dynamics model near a Wall

Here we implement the example described in Swan and Brady (2007) to obtain a deeper understanding of the near-wall Stokesian Dynamics model as well as to test the code. A system of two spheres separated by

a distance r is initially parallel to a plane wall at $z = 0$, and equal and opposite torques are applied to each of the spheres along the line joining their centres, as shown in Figure 10.1. This can be imagined to be a set of two spheres connected by a thin wire and twisted in opposite directions such that the wire becomes twisted. When released, if the spheres had been in free space, they would simply 'untwist', i.e. rotate individually in opposite directions along the same axis as the applied torque; in the presence of a wall, however, the doublet rotates as a whole as shown in the bottom panel of Figure 10.1, with an angular velocity of $\mathbf{\Omega}$.

In the absence of externally imposed flows, the linear velocity $\mathbf{U}$ and angular velocity $\boldsymbol{\omega}$ of each sphere can be calculated as in Equation (10.11) using a system of mobility matrices $\boldsymbol{\mathcal{M}}$ which depend only on fluid viscosity and the positions of each sphere. The forms of the mobility matrices depend on the chosen hydrodynamics model, which in our case can be referred to as the Stokesian Dynamics method extended to particles near a wall. The velocities here have been represented as functions of the total surface force $\mathbf{F}$ exerted by each particle as well as the first and higher moments of the surface force; the torque $\mathbf{T}$ and stresslet $\mathbf{S}$ are the anti-symmetric and traceless symmetric components of the first moment. The equation results from the *multipole expansion* of the boundary integral equation which itself is a direct result of the Stokes equations, and is hence general for a rigid body.

$$\begin{pmatrix} \mathbf{U} \\ \boldsymbol{\omega} \\ \mathbf{0} \\ . \\ . \end{pmatrix} = \begin{pmatrix} \boldsymbol{\mathcal{M}}^{\mathbf{UF}} & \boldsymbol{\mathcal{M}}^{\mathbf{UT}} & \boldsymbol{\mathcal{M}}^{\mathbf{US}} & . & . \\ \boldsymbol{\mathcal{M}}^{\boldsymbol{\omega}\mathbf{F}} & \boldsymbol{\mathcal{M}}^{\boldsymbol{\omega}\mathbf{T}} & \boldsymbol{\mathcal{M}}^{\boldsymbol{\omega}\mathbf{S}} & . & . \\ \boldsymbol{\mathcal{M}}^{\mathbf{EF}} & \boldsymbol{\mathcal{M}}^{\mathbf{ET}} & \boldsymbol{\mathcal{M}}^{\mathbf{ES}} & . & . \\ . & . & . & . & . \\ . & . & . & . & . \end{pmatrix} \begin{pmatrix} \mathbf{F} \\ \mathbf{T} \\ \mathbf{S} \\ . \\ . \end{pmatrix} \tag{10.11}$$

The equations can be truncated at the Force-Torque (F-T) level or can include more terms (which are faster-decaying in space) for more accurate results. Durlofsky et al. (1987) compare the performance (in terms of accuracy and computation time) between an F-T level and F-T-S level truncation for spheres in free space. To improve the accuracy of the near-field beyond the F-T-S level, some authors including Swan and Brady (2007) add a tensor to describe lubrication effects which are important when particles are very close to each other or to the wall. In our simulations, we use the F-T level truncation as we believe this would be sufficient for our purpose. Nevertheless, we explore the effects of including the stresslet through this example. The exact forms of the matrices we have used are provided in the previous Subsection.

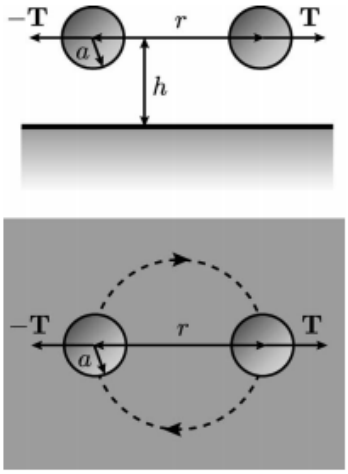

Figure 10.1: Two spheres of equal radius a are separated by a distance r and are at a height h above the wall at $z = 0$. The spheres experience equal and opposite torques of magnitude $\mathbf{T}$ along the line joining their centres. Image reproduced from Swan and Brady (2007) with permission.

Following Swan and Brady (2007) we calculate the rotation rate of the doublet, $\Omega = 2U_y/r$ at varying distances from the wall and for different

particle separation distances. The results obtained by Swan and Brady (2007) using F-T-S equations as well as lubrication tensors (Figure 10.2) show a few qualitative features of interest:

i. The doublet begins to rotate only when the distance between the doublet and the wall is less than the sphere radius ($h/a = 2$), and the separation between the spheres $r/a < 12$;

ii. For smaller sphere separations $r/a \approx 2.3$ and below, as the doublet approaches the wall its rotation velocity first increases and then begins to decrease;

iii. At smaller distances from the wall $h/a \approx 1.3$ and below, as the spheres approach each other (keeping h constant) the doublet's rotation velocity first increases and then begins to decrease.

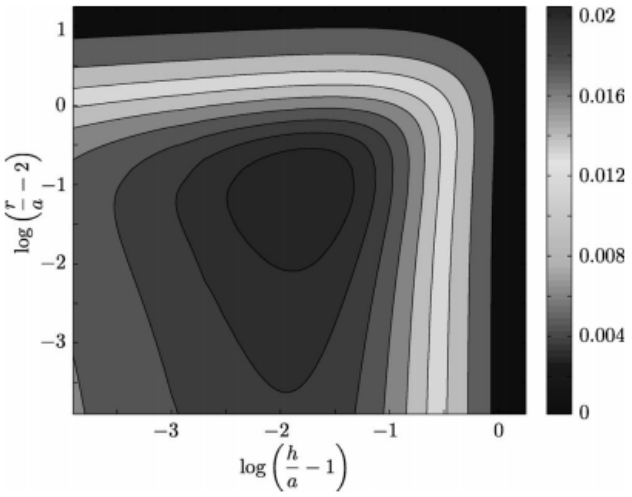

Figure 10.2: Results of Swan and Brady (2007): Normalized rotation rate of the doublet, $8\pi\mu a^3\mathbf{\Omega}/\mathbf{T}$ as a function of distance from the wall, h and particle separation distance r. Figure reproduced with permission.

The first observation (i) is captured approximately in Figure 10.3 for both F-T and F-T-S approximations. The rotation rate values are in general higher than those obtained by Swan and Brady (2007); this is due to the absence of the lubrication tensor, which would provide additional resistance to motion. Although our rotation rates are higher even for large sphere separations r, we note that the distances from the wall are small in all cases - the largest h of interest here is twice the sphere radius, meaning that the gap between the spheres and the wall is less than or equal to the sphere radius. We hence expect that the absence of the lubrication tensor would have some effect on these results.

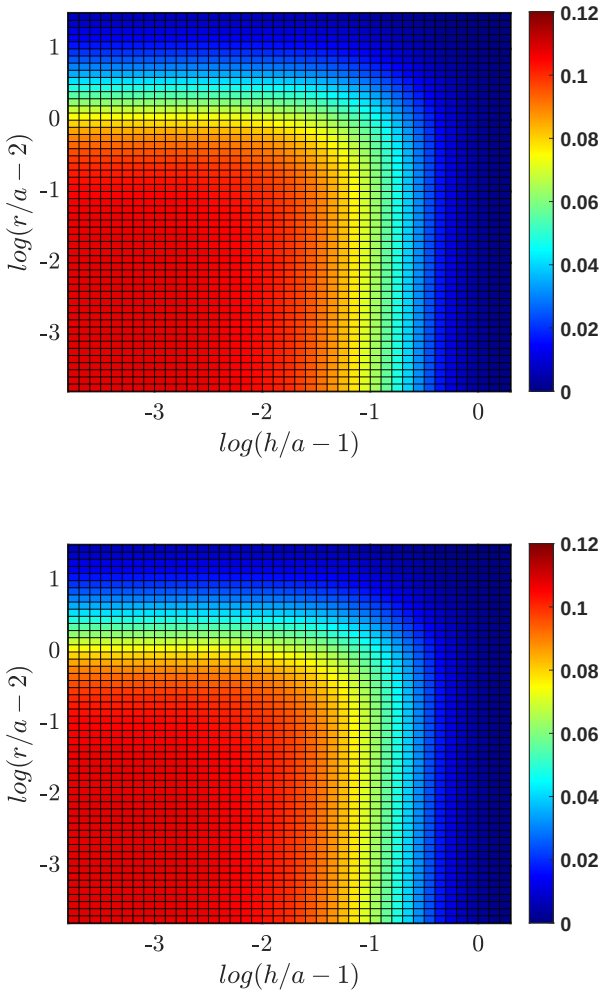

Figure 10.3: Results using F-T (top) and F-T-S (bottom): Normalized rotation rate of the doublet, $8\pi\mu a^3\mathbf{\Omega}/\mathbf{T}$ as a function of distance from the wall, h and particle separation distance r.

Observations (ii) and (iii) are not captured by the F-T or F-T-S approximations, which predict that the doublet would reach a maximum rotation rate of about 0.11 which will then remain constant as the doublet approaches the wall or as the spheres approach each other.

10.2 Quaternions and Lie Algebra

Here we introduce quaternions and Lie algebra in the context of rotations, based on readings from Holm (2011) and Solà et al. (2018).

Quaternions are four-dimensional vectors consisting of one real part q_o and three imaginary parts q_1, q_2 and q_3, and can be expressed as

$$\tilde{\mathbf{q}} = \mathrm{q_o} + \mathrm{q_1}\mathbf{i} + \mathrm{q_2}\mathbf{j} + \mathrm{q_3}\mathbf{k} = (\mathrm{q_o}, \mathbf{q}),$$

where $\mathbf{q}$ is known as vector part of $\tilde{\mathbf{q}}$ and $\mathrm{q_o}$ is the scalar part. A quaternion with zero scalar part is known as a *pure quaternion*. A three dimensional vector $\mathbf{a}$ can be represented as the pure quaternion $(0, \mathbf{a})$. A *unit quaternion* is a quaternion with unit magnitude:

$$||\tilde{\mathbf{q}}|| = \sqrt{q_o^2 + q_1^2 + q_2^2 + q_3^2} = 1.$$

Quaternions are closed under addition and multiplication, and possess additive and multiplicative inverses. The sum of two quaternions $\tilde{\mathbf{p}}$ and $\tilde{\mathbf{q}}$ can be expressed as

$$\tilde{\mathbf{p}} + \tilde{\mathbf{q}} = (\mathrm{p_o} + \mathrm{q_o}) + (\mathrm{p_1} + \mathrm{q_1})\mathbf{i} + (\mathrm{p_2} + \mathrm{q_2})\mathbf{j} + (\mathrm{p_3} + \mathrm{q_3})\mathbf{k},$$

from which we see that the additive inverse is simply $(-q_o, -q_1, -q_2, -q_3)$. Multiplication of quaternions makes use of the special products

$$\begin{aligned} \mathbf{i}^2 = \mathbf{j}^2 = \mathbf{k}^2 = \mathbf{ijk} &= -1, \\ \mathbf{ij} = \mathbf{k} &= -\mathbf{ji}, \\ \mathbf{jk} = \mathbf{i} &= -\mathbf{kj}, \\ \mathbf{ki} = \mathbf{j} &= -\mathbf{ik}, \end{aligned}$$

and can be expressed as

$$\tilde{\mathbf{p}}\tilde{\mathbf{q}} = \mathrm{p_o q_o} - \mathbf{p}\cdot\mathbf{q} + \mathrm{p_o}\mathbf{q} + \mathrm{q_o}\mathbf{p} + \mathbf{p}\times\mathbf{q}.$$

From the above we can verify that the multiplicative identity is $(1, 0, 0, 0)$. An important property of quaternions is that multiplication is associative, but not commutative. The inverse of a quaternion,

$$\tilde{\mathbf{q}}^{-1} = \frac{\tilde{\mathbf{q}}*}{||\tilde{\mathbf{q}}||^2},$$

where

$$\tilde{\mathbf{q}}* = \mathrm{q_o} - \mathrm{q_1}\mathbf{i} - \mathrm{q_2}\mathbf{j} - \mathrm{q_3}\mathbf{k}$$

is its complex conjugate. For a unit quaternion, $\tilde{\mathbf{q}}* = \tilde{\mathbf{q}}^{-1}$.

Unit quaternions are commonly associated with rotations of three-dimensional vectors in space, in an analogous manner to two-dimensional rotations using unit two-dimensional complex numbers. Any unit quaternion can be represented in terms of an angle θ, as

$$\tilde{\mathbf{q}} = \cos\frac{\theta}{2} + \mathbf{v_q}\sin\frac{\theta}{2},$$

where $\mathbf{v_q}$ is a unit vector. Here we can readily observe that the magnitude will always be equal to 1. The above quaternion can be used to rotate a vector $\mathbf{a}$ through $-\theta$ about $\mathbf{v_q}$. This can be expressed as follows, where $\mathbf{a'}$ is the vector $\mathbf{a}$ following rotation:

$$\begin{aligned}(0, \mathbf{a'}) &= \tilde{\mathbf{q}} \cdot (0, \mathbf{a}) \cdot \tilde{\mathbf{q}^*} \\ &= \mathbf{R}[\tilde{\mathbf{q}}(s,t)]\ (0, \mathbf{a}),\end{aligned} \tag{10.12}$$

where $\tilde{\mathbf{q}^*}$ is the quaternion conjugate of $\tilde{\mathbf{q}}$. $\mathbf{R}[\tilde{\mathbf{q}}]$ in the above equation is known as the *quaternion rotation matrix*, whose form can be readily obtained by expanding the quaternion product above:

$$\mathbf{R}[\tilde{\mathbf{q}}(s,t)] = \begin{bmatrix} 2\mathrm{q_o}^2 - 1 + 2\mathrm{q_1}^2 & 2\mathrm{q_1q_2} - 2\mathrm{q_o q_3} & 2\mathrm{q_1 q_3} + 2\mathrm{q_o q_2} \\ 2\mathrm{q_1 q_2} + 2\mathrm{q_o q_3} & 2\mathrm{q_o}^2 - 1 + 2\mathrm{q_2}^2 & 2\mathrm{q_2 q_3} - 2\mathrm{q_o q_1} \\ 2\mathrm{q_1 q_3} - 2\mathrm{q_o q_2} & 2\mathrm{q_2 q_3} + 2\mathrm{q_o q_1} & 2\mathrm{q_o}^2 - 1 + 2\mathrm{q_3}^2 \end{bmatrix}. \tag{10.13}$$

Unit quaternions form a Lie group under quaternion multiplication. A Lie group is a smooth manifold whose elements satisfy group axioms, i.e. closure, associativity and the existence of an identity and inverse, each of which we have discussed above. The group of unit quaternions S^3 can be visualised as a unit three-dimensional sphere in the four-dimensional space of quaternions. The group of unit 2D complex numbers S^1, expressed as $\mathbf{z} = \cos\theta + \mathbf{i}\sin\theta$, is a Lie group under complex multiplication and can be visualised as the unit circle in the 2D plane.

Every Lie group can be associated with a Lie algebra, which is defined as the tangent space to the Lie group at the identity. For example, the tangent space to the unit circle S^1 at the identity element 1 is the line $\mathbf{i}\mathbb{R}$ of imaginary numbers. The familiar expression

$$\mathbf{z} = \mathrm{e}^{\mathbf{i}\theta}$$

maps elements θ of $\mathbb{R}$ to elements of the unit complex numbers S^1, and is known as the exponential map. Similarly for unit quaternions S^3, the tangent space at the identity is the space of pure quaternions, i.e. vectors in $\mathbb{R}^3$. The exponential map

$$\tilde{\mathbf{q}} = \mathrm{e}^{\mathbf{u}\theta/2}$$

maps its elements to S^3. In the context of this work, the exponential map allows us to work with elements of $\mathbb{R}^3$ instead of the unit quaternions

themselves, which are more difficult to numerically update since they need to be normalised.

10.3 Form of the Approximate Jacobian Matrix

This section outlines the form of the approximate Jacobian matrix $\mathbf{J}$ used in our simulations, as mentioned in Chapter 3.

We may express our system of equations (as provided in Chapter 3 Section 3.3)

$$\mathbf{f_1}^{\mathrm{t+1}} = \mathbf{r_1^{t+1}} - \frac{4}{3}\mathbf{r_1^t} + \frac{1}{3}\mathbf{r_1^{t-1}} - \frac{2\Delta t}{3}\mathbf{v_1^{t+1}} = 0; \tag{10.14}$$

$$\mathbf{f_{2,n}}^{\mathrm{t+1}} = \mathbf{u_n^{t+1}} - \frac{1}{3}\mathbf{u_n^t} - \frac{2\Delta t}{3}\mathrm{dexp}^{-1}{}_{u_n^{t+1}}(\boldsymbol{\omega}_\mathbf{n}^{\mathbf{t+1}}) = 0, \qquad 1 \leq \mathrm{n} \leq \mathrm{N}; \tag{10.15}$$

$$\mathbf{f_{3,n}}^{\mathrm{t+1}} = \mathbf{r_1^{t+1}} + \frac{\Delta L}{2}\sum\nolimits_{m=2}^{n}(\mathbf{d_{1,m-1}^{t+1}} + \mathbf{d_{1,m}^{t+1}}) - \frac{4}{3}\mathbf{r_n^t} + \frac{1}{3}\mathbf{r_n^{t-1}} - \frac{2\Delta t}{3}\mathbf{v_n^{t+1}} = 0, \qquad 2 \leq \mathrm{n} \leq \mathrm{N} \tag{10.16}$$

as $\mathbf{f}(\mathbf{X}) = 0$, where $\mathbf{f} = (\mathbf{f_1}, \mathbf{f_2}, \mathbf{f_3})$ and $\mathbf{X} = (\mathbf{r}_1, \mathbf{u}_1 ... \mathbf{u}_\mathrm{N}, \mathbf{F}_{1/2} ... \mathbf{F}_{\mathrm{N}-1/2})$. Here Δt is the time step, ΔL is the distance between adjacent segments, $\mathbf{r}$ represents the position vectors of segments, $\mathbf{d_1}$ is the tangent vector at each segment, $\mathbf{u_n}$ are the Lie algebra elements associated with the material frame at each segment and $\mathbf{v}$ and $\boldsymbol{\omega}$ represent the linear and angular velocities of each segment respectively. Superscripts represent the timestep number (where t+1 is the current time step) and subscripts represent the segment number which has a maximum of N. The Jacobian matrix at the current time step is obtained as

$$\mathbf{J} = \begin{pmatrix} \mathbf{J_{11}} & \mathbf{J_{12}} & \mathbf{J_{13}} \\ \mathbf{J_{21}} & \mathbf{J_{22}} & \mathbf{J_{23}} \\ \mathbf{J_{31}} & \mathbf{J_{32}} & \mathbf{J_{33}} \end{pmatrix} = \begin{pmatrix} \dfrac{\partial \mathbf{f_1}}{\partial \mathbf{X_1}} & \dfrac{\partial \mathbf{f_1}}{\partial \mathbf{X_2}} & \dfrac{\partial \mathbf{f_1}}{\partial \mathbf{X_3}} \\ \dfrac{\partial \mathbf{f_2}}{\partial \mathbf{X_1}} & \dfrac{\partial \mathbf{f_2}}{\partial \mathbf{X_2}} & \dfrac{\partial \mathbf{f_2}}{\partial \mathbf{X_3}} \\ \dfrac{\partial \mathbf{f_3}}{\partial \mathbf{X_1}} & \dfrac{\partial \mathbf{f_3}}{\partial \mathbf{X_2}} & \dfrac{\partial \mathbf{f_3}}{\partial \mathbf{X_3}} \end{pmatrix},$$

where $\mathbf{X_1} = \mathbf{r_1}$, $\mathbf{X_2} = (\mathbf{u}_1 ... \mathbf{u}_\mathrm{N})$ and $\mathbf{X_3} = (\mathbf{F}_{3/2} ... \mathbf{F}_{\mathrm{N}-1/2})$ where $\mathbf{F}$ is the passive internal force. The final form of each block of the matrix is provided below. For details on the derivation of these expressions, the reader is referred to Schoeller et al. (2021). The expressions here mirror those provided in Schoeller et al. (2021) except for terms containing the active moment.

The first block $\mathbf{J_{11}}$ is a 3×3 identity matrix. Block $\mathbf{J_{31}}$ has a size of $(3\mathrm{N} - 3) \times 3$ and is composed of $N - 1$ identity matrices (each of size 3×3). Blocks $\mathbf{J_{12}}$ and $\mathbf{J_{21}}$ are composed of zeros and have sizes of $3 \times 3\mathrm{N}$ and $3\mathrm{N} \times 3$ respectively.

Block $\mathbf{J_{13}}$ has a size of $3 \times (3\mathrm{N} - 3)$ and is expressed as

$$(\mathbf{J_{13}})_{\mathrm{pq}} = \frac{\partial \mathbf{f_{1,p}}}{\partial \mathbf{F_{q-1/2}}} = \frac{-\Delta t}{9\pi\mu a}\delta_{2q}\mathbf{I},$$

where subscripts p and q represent segment numbers with p = 1 and $2 \leq \mathrm{q} \leq \mathrm{N}$, μ is fluid viscosity, a is the radius of the filament, $\mathbf{I}$ is the 3×3 identity matrix and δ is the Kronecker delta.

Block $\mathbf{J_{32}}$ has a size of $(3\mathrm{N}-3) \times 3\mathrm{N}$ and is expressed as

$$(\mathbf{J_{32}})_{\mathrm{pq}} = \frac{\partial \mathbf{f_{3,p}}}{\partial \mathbf{u_q}} = \frac{\Delta L}{2} \sum_{m=2}^{p} (\delta_{(p-1)q} + \delta_{pq}) \, [\times \mathbf{d_{1,q}}],$$

where $[\times \mathbf{d_{1,q}}]$ is defined following the notation in Schoeller et al. (2021):

$$[\times \mathbf{a}] = \begin{bmatrix} 0 & a_3 & -a_2 \\ -a_3 & 0 & a_1 \\ a_2 & -a_1 & 0 \end{bmatrix} = [\mathbf{a} \times]^{\dagger},$$

so that $[\times \mathbf{a}]\mathbf{b} = \mathbf{b} \times \mathbf{a}$ and $[\mathbf{a} \times]\mathbf{b} = \mathbf{a} \times \mathbf{b}$ for two vectors $\mathbf{a}$ and $\mathbf{b}$.

Block $\mathbf{J_{33}}$ has a size of $(3\mathrm{N}-3) \times (3\mathrm{N}-3)$ and is expressed as

$$(\mathbf{J_{33}})_{\mathrm{pq}} = \frac{\partial \mathbf{f_{3,p}}}{\partial \mathbf{F_{q-1/2}}} = \frac{-\Delta t}{9\pi\mu a} (\delta_{(p+1)q} - \delta_{pq}) \mathbf{I}.$$

Block $\mathbf{J_{22}}$ has a size of $3\mathrm{N} \times 3\mathrm{N}$ and is expressed as

$$\begin{aligned}(\mathbf{J_{22}})_{\mathrm{pq}} = \frac{\partial \mathbf{f_{2,p}}}{\partial \mathbf{u_q}} = \delta_{pq}\mathbf{I} - \frac{\Delta t}{12\pi\mu a^3} \Big[& \frac{\partial \mathbf{T_p}}{\partial \mathbf{u_q}} - \frac{1}{2}\delta_{pq}\mathbf{I} \times \mathbf{T_p} - \frac{1}{2}\mathbf{u_p} \times \frac{\partial \mathbf{T_p}}{\partial \mathbf{u_q}} \\ & + \frac{1}{12}\left(\delta_{pq}\mathbf{I} \times (\mathbf{u_p} \times \mathbf{T_p})\right) + \frac{1}{12}\mathbf{u_p} \times \left(\delta_{pq}\mathbf{I} \times \mathbf{T_p} + \mathbf{u_p} \times \frac{\partial \mathbf{T_p}}{\partial \mathbf{u_q}}\right) \Big],\end{aligned}$$

where the torque $\mathbf{T}$ is expressed as

$$\mathbf{T_p} = \mathbf{M_{p+1/2}} - \mathbf{M_{p-1/2}} + \frac{\Delta L}{2}\mathbf{d_{1,p}} \times (\mathbf{F_{p+1/2}} + \mathbf{F_{p-1/2}}) + \mathbf{M^a_{p+1/2}} - \mathbf{M^a_{p-1/2}}.$$

Here $\mathbf{M}$ represents the passive internal moment and $\mathbf{M^a} = M_1^a \mathbf{d_1} + M_2^a \mathbf{d_2} + M_3^a \mathbf{d_3}$ represents the active moment. The term $\partial \mathbf{T_p}/\partial \mathbf{u_q}$ is expressed as:

$$\frac{\partial \mathbf{T_p}}{\partial \mathbf{u_q}} = \frac{\partial(\mathbf{M_{p+1/2}} + \mathbf{M^a_{p+1/2}}}{\partial \mathbf{u_q})} - \frac{\partial(\mathbf{M_{p-1/2}} + \mathbf{M^a_{p-1/2}})}{\partial \mathbf{u_q}} + \frac{\Delta L}{2}\delta_{pq}([\times \mathbf{F_{p+1/2}}] + [\times \mathbf{F_{p-1/2}}])[\times \mathbf{d_{1,p}}],$$

with

$$\begin{aligned}\frac{\partial(\mathbf{M_{p+1/2}} + \mathbf{M^a_{p+1/2}})}{\partial \mathbf{u_q}} = \delta_{(p+1)q} \Big[& \frac{K_T}{2}\Big(K_0[\times \mathbf{d_{1,p+1}}] + \frac{(\mathbf{d_{1,p+1}} + \mathbf{d_{1,p}})}{2\Delta L}\Big([\times \mathbf{d_{2,p+1}}]\mathbf{d_{3,p}} - [\times \mathbf{d_{3,p+1}}]\mathbf{d_{2,p}}\Big)\Big) \\ & + \frac{K_B}{2}\Big(\frac{2}{\Delta L}[\mathbf{d_{1,p}} \times][\times \mathbf{d_{1,p+1}}] + \frac{M_2^a}{K_B}[\times \mathbf{d_{2,p+1}}] + \frac{M_3^a}{K_B}[\times \mathbf{d_{3,p+1}}]\Big)\Big] \\ & + \delta_{pq}\Big[\frac{K_T}{2}\Big(K_0[\times \mathbf{d_{1,p}}] + \frac{(\mathbf{d_{1,p+1}} + \mathbf{d_{1,p}})}{2\Delta L}\Big(\mathbf{d_{2,p+1}}[\times \mathbf{d_{3,p}}] - \mathbf{d_{3,p+1}}[\times \mathbf{d_{2,p}}]\Big)\Big) \\ & + \frac{K_B}{2}\Big(\frac{2}{\Delta L}[\times \mathbf{d_{1,p}}][\times \mathbf{d_{1,p+1}}] + \frac{M_2^a}{K_B}[\times \mathbf{d_{2,p}}] + \frac{M_3^a}{K_B}[\times \mathbf{d_{3,p}}]\Big)\Big],\end{aligned}$$

where K_B and K_T are the bending and twisting stiffnesses, respectively and $K_0 = (\mathbf{d_{2,p+1}} \cdot \mathbf{d_{3,p}} - \mathbf{d_{3,p+1}} \cdot \mathbf{d_{2,p}})/2\Delta L - M_1^a/K_T$.

Finally, $\mathbf{J_{23}}$ has a size of $3\mathrm{N} \times (3\mathrm{N} - 3)$ and is expressed as

$$(\mathbf{J_{23}})_{\mathrm{pq}} = \frac{\partial \mathbf{f_{2,p}}}{\partial \mathbf{F_{q-1/2}}} = -\frac{\Delta t}{12\pi\mu a^3}\left[\frac{\partial \mathbf{T_p}}{\partial \mathbf{F_{q-1/2}}} - \frac{1}{2}[\mathbf{u_p}\times]\frac{\partial \mathbf{T_p}}{\partial \mathbf{F_{q-1/2}}} + \frac{1}{12}[\mathbf{u_p}\times][\mathbf{u_p}\times]\frac{\partial \mathbf{T_p}}{\partial \mathbf{F_{q-1/2}}}\right],$$

with

$$\frac{\partial \mathbf{T_p}}{\partial \mathbf{F_{q-1/2}}} = \frac{\Delta L}{2}[\mathbf{d_{1,p}}\times](\delta_{(p+1)q} + \delta_{pq}).$$

11
Bibliography

Ainley, J., Durkin, S., Embid, R., Boindala, P., and Cortez, R. (2008). The method of images for regularized Stokeslets. *Journal of Computational Physics*, 227(9):4600–4616.

Antman, S. S. (1973). The theory of rods. In Truesdell, C., editor, *Linear theories of elasticity and thermoelasticity*. Springer, Berlin, Heidelberg.

Badano, J. L., Mitsuma, N., Beales, P. L., and Katsanis, N. (2006). The ciliopathies: An emerging class of human genetic disorders. *Annual Review of Genomics and Human Genetics*, 7(1):125–148. PMID: 16722803.

Bayly, P. V. and Wilson, K. S. (2014). Equations of interdoublet separation during flagella motion reveal mechanisms of wave propagation and instability. *Biophysical Journal*, 107(7):1756–1772.

Blake, J. (1971). A note on the image system for a Stokeslet in a no-slip boundary. In *Mathematical Proceedings of the Cambridge Philosophical Society*, volume 70, pages 303–310. Cambridge University Press.

Bossis, G., Meunier, A., and Sherwood, J. (1991). Stokesian dynamics simulations of particle trajectories near a plane. *Physics of Fluids A: Fluid Dynamics*, 3(8):1853–1858.

Bower, R., Tritschler, D., VanderWaal, K., Perrone, C. A., Mueller, J., Fox, L., Sale, W. S., and Porter, M. (2013). The N-DRC forms a conserved biochemical complex that maintains outer doublet alignment and limits microtubule sliding in motile axonemes. *Molecular Biology of the Cell*, 24(8):1134–1152.

Boyle, M. (2017). The integration of angular velocity. *Advances in Applied Clifford Algebras*, 27(3):2345–2374.

Brokaw, C. J. (1972). Computer simulation of flagellar movement: I. Demonstration of stable bend propagation and bend initiation by the sliding filament model. *Biophysical Journal*, 12(5):564–586.

Brokaw, C. J. (2006). Flagellar propulsion. *Journal of Experimental Biology*, 209(6):985–986.

Brumley, D. R., Polin, M., Pedley, T. J., and Goldstein, R. E. (2012). Hydrodynamic synchronization and metachronal waves on the surface of the colonial alga Volvox carteri. *Physical Review Letters*, 109(26):268102.

Camalet, S. and Jülicher, F. (2000). Generic aspects of axonemal beating. *New Journal of Physics*, 2(1):24.

Carichino, L. and Olson, S. D. (2019). Emergent three-dimensional sperm motility: coupling calcium dynamics and preferred curvature in a kirchhoff rod model. *Mathematical Medicine and Biology: A Journal of the IMA*, 36(4):439–469.

Chakrabarti, B., Liu, Y., LaGrone, J., Cortez, R., Fauci, L., Du Roure, O., Saintillan, D., and Lindner, A. (2020). Flexible filaments buckle into helicoidal shapes in strong compressional flows. *Nature Physics*, 16(6):689–694.

Chakrabarti, B. and Saintillan, D. (2019a). Hydrodynamic synchronization of spontaneously beating filaments. *Physical Review Letters*, 123(20):208101.

Chakrabarti, B. and Saintillan, D. (2019b). Spontaneous oscillations, beating patterns, and hydrodynamics of active microfilaments. *Physical Review Fluids*, 4:043102.

Coleman, B. D., Dill, E. H., Lembo, M., Lu, Z., and Tobias, I. (1993). On the dynamics of rods in the theory of kirchhoff and clebsch. *Archive for Rational Mechanics and Analysis*, 121(4):339–359.

Cortez, R. (2001). The method of regularized Stokeslets. *SIAM Journal on Scientific Computing*, 23(4):1204–1225.

Cortez, R. (2018). Regularized Stokeslet segments. *Journal of Computational Physics*, 375(8):783–796.

Cortez, R., Fauci, L., and Medovikov, A. (2005). The method of regularized Stokeslets in three dimensions: analysis, validation, and application to helical swimming. *Physics of Fluids*, 17(3):031504.

De Canio, G., Lauga, E., and Goldstein, R. E. (2017). Spontaneous oscillations of elastic filaments induced by molecular motors. *Journal of the Royal Society Interface*, 14(136):20170491.

Delmotte, B., Climent, E., and Plouraboué, F. (2015). A general formulation of bead models applied to flexible fibers and active filaments at low reynolds number. *Journal of Computational Physics*, 286:14–37.

Dill, E. H. (1992). Kirchhoff's theory of rods. *Archive for History of Exact Sciences*, 44:1–23.

Durlofsky, L., Brady, J. F., and Bossis, G. (1987). Dynamic simulation of hydrodynamically interacting particles. *Journal of Fluid Mechanics*, 180:21–49.

Elgeti, J., Kaupp, U. B., and Gompper, G. (2010). Hydrodynamics of sperm cells near surfaces. *Biophysical Journal*, 99(4):1018–1026.

Elgeti, J., Kaupp, U. B., and Gompper, G. (2011). Response to comment on article: hydrodynamics of sperm cells near surfaces. *Biophysical Journal*, 100(11):2321–2324.

Elgeti, J., Winkler, R. G., and Gompper, G. (2015). Physics of microswimmersâĂŤsingle particle motion and collective behavior: a review. *Reports on Progress in Physics*, 78(5):056601.

Fily, Y., Subramanian, P., Schneider, T. M., Chelakkot, R., and Gopinath, A. (2020). Buckling instabilities and spatio-temporal dynamics of active elastic filaments. *Journal of the Royal Society Interface*, 17(165):20190794.

Friedrich, B. M., Riedel-Kruse, I. H .and Howard, J., and Jülicher, F. (2010). High-precision tracking of sperm swimming fine structure provides strong test of resistive force theory. *Journal of Experimental Biology*, 213(Pt 8):1226–34.

Gadêlha, H., Gaffney, E., Smith, D. J., and Kirkman-Brown, J. C. (2010). Nonlinear instability in flagellar dynamics: a novel modulation mechanism in sperm migration? *Journal of the Royal Society Interface*, 7:1689–1697.

Gadêlha, H. and Gaffney, E. A. (2019). Flagellar ultrastructure suppresses buckling instabilities and enables mammalian sperm navigation in high-viscosity media. *Journal of the Royal Society Interface*, 16(152):20180668.

Gaffney, E. A., Gadêlha, H., Smith, D. J., Blake, J. R., and Kirkman-Brown, J. C. (2011). Mammalian sperm motility: observation and theory. *Annual Review of Fluid Mechanics*, 43:501–528.

Gallagher, M. T., Cupples, G., Ooi, E. H., Kirkman-Brown, J., and Smith, D. (2019). Rapid sperm capture: high-throughput flagellar waveform analysis. *Human Reproduction*, 34(7):1173–1185.

Gazzola, M., Dudte, L., McCormick, A., and Mahadevan, L. (2018). Forward and inverse problems in the mechanics of soft filaments. *Royal Society Open Science*, 5(6):171628.

Gong, A., Rode, S., Gompper, G., Kaupp, U. B., Elgeti, J., Friedrich, B., and Alvarez, L. (2021). Reconstruction of the three-dimensional beat pattern underlying swimming behaviors of sperm. *The European Physical Journal E*, 44(7):1–12.

Gray, J. (1955). The movement of sea-urchin spermatozoa. *Journal of Experimental Biology*, 32(4):775–801.

Gray, J. and Hancock, G. (1955). The propulsion of sea-urchin spermatozoa. *Journal of Experimental Biology*, 32:802–814.

Gu, N.-H., Zhao, W.-L., Wang, G.-S., and Sun, F. (2019). Comparative analysis of mammalian sperm ultrastructure reveals relationships between sperm morphology, mitochondrial functions and motility. *Reproductive Biology and Endocrinology*, 17(1):1–12.

Guasto, J. S., Estrada, J. B., Menolascina, F., Burton, L. J., Patel, M., Franck, C., Hosoi, A., Zimmer, R. K., and Stocker, R. (2020). Flagellar kinematics reveals the role of environment in shaping sperm motility. *Journal of the Royal Society Interface*, 17(170):20200525.

Guerrero, A., Carneiro, J., Pimentel, A., Wood, C. D., Corkidi, G., and Darszon, A. (2011). Strategies for locating the female gamete: the importance of measuring sperm trajectories in three spatial dimensions. *MHR: Basic Science of Reproductive Medicine*, 17(8):511–523.

Hall-McNair, A. L., Montenegro-Johnson, T. D., Gadêlha, H., Smith, D. J., and Gallagher, M. T. (2019). Efficient implementation of elastohydrodynamics via integral operators. *Physical Review Fluids*, 4:113101.

Hancock, G. (1953). The self-propulsion of microscopic organisms through liquids. In *Proceedings of the Royal Society of London. Series A. Mathematical, Physical and Engineering Sciences*, volume 217, pages 96–121. The Royal Society.

Hilfinger, A. (2006). *Dynamics of cilia and flagella*. PhD thesis, TU Dresden.

Hilfinger, A. and Jülicher, F. (2008). The chirality of ciliary beats. *Physical Biology*, 5(1):016003.

Hines, M. and Blum, J. (1978). Bend propagation in flagella. i. derivation of equations of motion and their simulation. *Biophysical Journal*, 23(1):41–57.

Holm, D. D. (2011). *Geometric Mechanics-Part II: Rotating, Translating and Rolling*. Imperial College Press, London.

Huang, J., Carichino, L., and Olson, S. D. (2018). Hydrodynamic interactions of actuated elastic filaments near a planar wall with applications to sperm motility. *Journal of Coupled Systems and Multiscale Dynamics*, 6(3):163–175.

Hyakutake, T., Suzuki, H., and Yamamoto, S. (2015a). Effect of non-newtonian fluid properties on bovine sperm motility. *Journal of Biomechanics*, 48(12):2941–2947.

Hyakutake, T., Suzuki, H., and Yamamoto, S. (2015b). Effect of viscosity on motion characteristics of bovine sperm. *Journal of Aero Aqua Bio-mechanisms*, 4(1):63–70.

Ishimoto, K., Gadêlha, H., Gaffney, E. A., Smith, D. J., and Kirkman-Brown, J. (2018). Human sperm swimming in a high viscosity mucus analogue. *Journal of Theoretical Biology*, 446:1–10.

Ishimoto, K. and Gaffney, E. A. (2014). A study of spermatozoan swimming stability near a surface. *Journal of Theoretical Biology*, 360:187–199.

Ishimoto, K. and Gaffney, E. A. (2015). Fluid flow and sperm guidance: a simulation study of hydrodynamic sperm rheotaxis. *Journal of The Royal Society Interface*, 12(106):20150172.

Ishimoto, K. and Gaffney, E. A. (2018). An elastohydrodynamical simulation study of filament and spermatozoan swimming driven by internal couples. *IMA Journal of Applied Mathematics*, 83(4):655–679.

Ivic, A., Onyeaka, H., Girling, A., Brewis, I. A., Ola, B., Hammadieh, N., Papaioannou, S., and Barratt, C. L. (2002). Critical evaluation of methylcellulose as an alternative medium in sperm migration tests. *Human Reproduction*, 17(1):143–149.

Izawa, Y. and Shingyoji, C. (2020). Mechanical induction of oscillatory movement in demembranated, immotile flagella of sea urchin sperm at very low atp concentrations. *Journal of Experimental Biology*, 223(20):jeb225797.

Jung, S., Mareck, K., Fauci, L., and Shelley, M. J. (2007). Rotational dynamics of a superhelix towed in a stokes fluid. *Physics of Fluids*, 19(10):103105.

Katz, D. F., Blake, J. R., and Paveri-Fontana, S. L. (1975). On the movement of slender bodies near plane boundaries at low Reynolds number. *Journal of Fluid Mechanics*, 72(3):529–540.

Kim, S. and Karrila, S. J. (2005). *Microhydrodynamics: Principles and Selected Applications.* Dover Publications, Mineola, New York.

King, S. M. (2012). Integrated control of axonemal dynein aaa+ motors. *Journal of Structural Biology*, 179(2):222–228.

Konno, A., Setou, M., and Ikegami, K. (2012). Ciliary and flagellar structure and functionâĂŤtheir regulations by posttranslational modifications of axonemal tubulin. *International Review of Cell and Molecular Biology*, 294:133–170.

Lauga, E. (2016). Bacterial hydrodynamics. *Annual Review of Fluid Mechanics*, 48:105–130.

Lauga, E. and Powers, T. R. (2009). The hydrodynamics of swimming microorganisms. *Reports on Progress in Physics*, 72(9):096601.

Lighthill, J. (1976). Flagellar hydrodynamics. *SIAM Review*, 18:161–230.

Lim, S. (2010). Dynamics of an open elastic rod with intrinsic curvature and twist in a viscous fluid. *Physics of Fluids*, 22(2):024104.

Lin, J. and Nicastro, D. (2018). Asymmetric distribution and spatial switching of dynein activity generates ciliary motility. *Science*, 360:eaar1968.

Lindemann, C. B. (1994). A model of flagellar and ciliary functioning which uses the forces transverse to the axoneme as the regulator of dynein activation. *Cell Motility and the Cytoskeleton*, 29(2):141–154.

Lindemann, C. B. and Lesich, K. A. (2010). Flagellar and ciliary beating: the proven and the possible. *Journal of Cell Science*, 123(Pt 4):519–28.

Lindemann, C. B. and Lesich, K. A. (2016). Functional anatomy of the mammalian sperm flagellum. *Cytoskeleton*, 73(11):652–669.

Lindemann, C. B. and Lesich, K. A. (2021). The many modes of flagellar and ciliary beating: Insights from a physical analysis. *Cytoskeleton*, 78(2):36–51.

Lindemann, C. B., Rudd, W. G., and Rikmenspoel, R. (1973). The stiffness of the flagella of impaled bull sperm. *Biophysical Journal*, 13(5):437–448.

Ling, F., Guo, H., and Kanso, E. (2018). Instability-driven oscillations of elastic microfilaments. *Journal of The Royal Society Interface*, 15(149):20180594.

Liu, Q.-Y., Tang, X.-Y., Chen, D.-D., Xu, Y.-Q., and Tian, F.-B. (2020). Hydrodynamic study of sperm swimming near a wall based on the immersed boundary-lattice boltzmann method. *Engineering Applications of Computational Fluid Mechanics*, 14(1):853–870.

Lomholt, S. and Maxey, M. R. (2003). Force-coupling method for particulate two-phase flow: Stokes flow. *Journal of Computational Physics*, 184(2):381–405.

Lubliner, J. and Blum, J. (1977). Analysis of bend initiation in cilia according to a sliding filament model. *Journal of Theoretical Biology*, 69(1):87–99.

Machin, K. (1958). Wave propagation along flagella. *Journal of Experimental Biology*, 35(4):796–806.

Martindale, J., Jabbarzadeh, M., and Fu, H. C. (2016). Choice of computational method for swimming and pumping with nonslender helical filaments at low reynolds number. *Physics of Fluids*, 28(2):021901.

Mojiri, S., Isbaner, S., Mühle, S., Jang, H., Bae, A. J., Gregor, I., Gholami, A., and Enderlein, J. (2021). Rapid multi-plane phase-contrast microscopy reveals torsional dynamics in flagellar motion. *Biomedical Optics Express*, 12(6):3169–3180.

Mondal, D., Adhikari, R., and Sharma, P. (2020). Internal friction controls active ciliary oscillations near the instability threshold. *Science Advances*, 6(33):eabb0503.

Montenegro-Johnson, T., Gadelha, H., and Smith, D. J. (2015). Spermatozoa scattering by a microchannel feature: an elastohydrodynamic model. *Royal Society Open Science*, 2(3):140475.

Moreau, C., Giraldi, L., and Gadêlha, H. (2018). The asymptotic coarse-graining formulation of slender-rods, bio-filaments and flagella. *Journal of the Royal Society Interface*, 15(144):20180235.

Nandagiri, A., Gaikwad, A. S., Potter, D. L., Nosrati, R., Soria, J., O'Bryan, M. K., Jadhav, S., and Prabhakar, R. (2021). Flagellar energetics from high-resolution imaging of beating patterns in tethered mouse sperm. *eLife*, 10:e62524.

Nazockdast, E., Rahimian, A., Zorin, D., and Shelley, M. (2017). A fast platform for simulating semi-flexible fiber suspensions applied to cell mechanics. *Journal of Computational Physics*, 329:173–209.

Nosrati, R., Driouchi, A., Yip, C. M., and Sinton, D. (2015). Two-dimensional slither swimming of sperm within a micrometre of a surface. *Nature Communications*, 6:1–9.

Okuno, M. and Hiramoto, Y. (1979). Direct measurements of the stiffness of echinoderm sperm flagella. *Journal of Experimental Biology*, 79(1):235–243.

Olson, S. D., Lim, S., and Cortez, R. (2013). Modeling the dynamics of an elastic rod with intrinsic curvature and twist using a regularized stokes formulation. *Journal of Computational Physics*, 238:169–187.

Olson, S. D., Suarez, S. S., and Fauci, L. J. (2011). Coupling biochemistry and hydrodynamics captures hyperactivated sperm motility in a simple flagellar model. *Journal of Theoretical Biology*, 283(1):203–216.

Oriola, D., Gadêlha, H., and Casademunt, J. (2017). Nonlinear amplitude dynamics in flagellar beating. *Royal Society Open Science*, 4(3):160698.

Pate, E. and Brokaw, C. (1980). Movement of spermatozoa in viscous environments. *Journal of Experimental Biology*, 88:395–397.

Pereira, R., Sá, R., Barros, A., and Sousa, M. (2017). Major regulatory mechanisms involved in sperm motility. *Asian Journal of Andrology*, 19(1):5.

Peskin, C. S. (2002). The immersed boundary method. *Acta Numerica*, 11:479–517.

Powar, S., Parast, F. Y., Nandagiri, A., Gaikwad, A. S., Potter, D. L., O'Bryan, M. K., Prabhakar, R., Soria, J., and Nosrati, R. (2022). Unraveling the kinematics of sperm motion by reconstructing the flagellar wave motion in 3d. *Small Methods*, 6(3):2101089.

Pozrikidis, C. (1992). *Boundary integral and singularity methods for linearized viscous flow*. Cambridge University Press.

Purcell, E. M. (1977). Life at low reynolds number. *American Journal of Physics*, 45(1):3–11.

Rallabandi, B., Wang, Q., and Potomkin, M. (2022). Self-sustained three-dimensional beating of a model eukaryotic flagellum. *Soft Matter*, 18(28):5312–5322.

Ramia, M., Tullock, D., and Phan-Thien, N. (1993). The role of hydrodynamic interaction in the locomotion of microorganisms. *Biophysical Journal*, 65(2):755–778.

Riedel-Kruse, I. H., Hilfinger, A., Howard, J., and Jülicher, F. (2007). How molecular motors shape the flagellar beat. *HFSP journal*, 1(3):192–208.

Rostami, M. W. and Olson, S. D. (2016). Kernel-independent fast multipole method within the framework of regularized Stokeslets. *Journal of Fluids and Structures*, 67:60–84.

Sangani, A. S. and Gopinath, A. (2020). Elastohydrodynamical instabilities of active filaments, arrays, and carpets analyzed using slender-body theory. *Physical Review Fluids*, 5(8):083101.

Sartori, P., Geyer, V. F., Howard, J., and Jülicher, F. (2016a). Curvature regulation of the ciliary beat through axonemal twist. *Physical Review E*, 94(4):042426.

Sartori, P., Geyer, V. F., Scholich, A., Jülicher, F., and Howard, J. (2016b). Dynamic curvature regulation accounts for the symmetric and asymmetric beats of Chlamydomonas flagella. *eLife*, 5:e13258.

Satir, P. (1968). Studies on cilia. *Journal of Cell Biology*, 39(1):77–94.

Satir, P., Heuser, T., and Sale, W. S. (2014). A structural basis for how motile cilia beat. *Bioscience*, 64(12):1073–1083.

Schoeller, S. F., Townsend, A. K., Westwood, T. A., and Keaveny, E. E. (2021). Methods for suspensions of passive and active filaments. *Journal of Computational Physics*, 424:109846.

Simons, J., Fauci, L., and Cortez, R. (2015). A fully three-dimensional model of the interaction of driven elastic filaments in a Stokes flow with applications to sperm motility. *Journal of Biomechanics*, 48(9):1639–1651.

Simons, J., Olson, S., Cortez, R., and Fauci, L. (2014). The dynamics of sperm detachment from epithelium in a coupled fluid-biochemical model of hyperactivated motility. *Journal of Theoretical Biology*, 354:81–94.

Smith, D., Gaffney, E., Blake, J., and Kirkman-Brown, J. (2009a). Human sperm accumulation near surfaces: a simulation study. *Journal of Fluid Mechanics*, 621:289–320.

Smith, D., Gaffney, E., Gadêlha, H., Kapur, N., and Kirkman-Brown, J. (2009b). Bend propagation in the flagella of migrating human sperm, and its modulation by viscosity. *Cell Motility and the Cytoskeleton*, 66(4):220–236.

Smith, D., Gaffney, E., Shum, H., Gadêlha, H., and Kirkman-Brown, J. (2011). Comment on the article by J. Elgeti, U. B. Kaupp, and G. Gompper: hydrodynamics of sperm cells near surfaces. *Biophysical Journal*, 100(9):2318–2320.

Solà, J., Deray, J., and Atchuthan, D. (2018). A micro lie theory for state estimation in robotics. *arXiv preprint arXiv:1812.01537*.

Suarez, S. S. (2016). Mammalian sperm interactions with the female reproductive tract. *Cell and Tissue Research*, 363(1):185–194.

Swan, J. W. and Brady, J. F. (2007). Simulation of hydrodynamically interacting particles near a no-slip boundary. *Physics of Fluids*, 19(11):113306.

Taylor, G. I. (1951). Analysis of the swimming of microscopic organisms. *Proceedings of the Royal Society of London. Series A. Mathematical and Physical Sciences*, 209:447–461.

Veeraragavan, S. (2023). Internally-driven Kirchhoff Rod. Software. https://doi.org/10.26180/21204512.v1.

Veeraragavan, S. and Prabhakar, R. (2020). Is hydrodynamic interaction important in beating patterns in internally-driven microfilaments? In *Proceedings of the 22nd Australasian Fluid Mechanics Conference AFMC2020*, Brisbane, Australia. The University of Queensland.

Vernon, G. G. and Woolley, D. M. (1999). Three-dimensional motion of avian spermatozoa. *Cell Motility and the Cytoskeleton*, 42(2):149–161.

Wajnryb, E., Mizerski, K. A., Zuk, P. J., and Szymczak, P. (2013). Generalization of the rotne-prager-yamakawa mobility and shear disturbance tensors. *Journal of Fluid Mechanics*, 731:R3.

Walker, B. J., Ishimoto, K., Gadêlha, H., and Gaffney, E. A. (2019). Filament mechanics in a half-space via regularised Stokeslet segments. *Journal of Fluid Mechanics*, 879:808–833.

Walker, B. J., Ishimoto, K., and Gaffney, E. A. (2020a). Efficient simulation of filament elastohydrodynamics in three dimensions. *Physical Review Fluids*, 5(12):123103.

Walker, B. J., Phuyal, S., Ishimoto, K., Tung, C.-K., and Gaffney, E. A. (2020b). Computer-assisted beat-pattern analysis and the flagellar waveforms of bovine spermatozoa. *Royal Society Open Science*, 7(6):200769.

Weiss, J. (2019). A tutorial on the proper orthogonal decomposition. In *AIAA Aviation 2019 Forum*, page 3333.

Werner, S., Rink, J. C., Riedel-Kruse, I. H., and Friedrich, B. M. (2014). Shape mode analysis exposes movement patterns in biology: Flagella and flatworms as case studies. *PLoS One*, 9:e113083.

Winet, H., Bernstein, G., and Head, J. (1984). Observations on the response of human spermatozoa to gravity, boundaries and fluid shear. *Reproduction*, 70(2):511–523.

Wirschell, M., Yamamoto, R., Alford, L., Gokhale, A., Gaillard, A., and Sale, W. S. (2011). Regulation of ciliary motility: conserved protein kinases and phosphatases are targeted and anchored in the ciliary axoneme. *Archives of Biochemistry and Biophysics*, 510(2):93–100.

Woolley, D. (2003). Motility of spermatozoa at surfaces. *Reproduction*, 126(2):259–270.

Woolley, D. and Vernon, G. (2001). A study of helical and planar waves on sea urchin sperm flagella, with a theory of how they are generated. *Journal of Experimental Biology*, 204(7):1333–1345.

Woolley, D. M. (2010). Flagellar oscillation: a commentary on proposed mechanisms. *Biological Reviews*, 85(3):453–470.

Xu, Y.-Q., Wang, M.-Y., Liu, Q.-Y., Tang, X.-Y., and Tian, F.-B. (2018). External force-induced focus pattern of a flexible filament in a viscous fluid. *Applied Mathematical Modelling*, 53:369–383.

Yang, Y., Elgeti, J., and Gompper, G. (2008). Cooperation of sperm in two dimensions: synchronization, attraction, and aggregation through hydrodynamic interactions. *Physical Review E*, 78(6):061903.

Zaferani, M., Javi, F., Mokhtare, A., Li, P., and Abbaspourrad, A. (2021). Rolling controls sperm navigation in response to the dynamic rheological properties of the environment. *eLife*, 10:e68693.

Zhang, T. and Goldman, D. I. (2014). The effectiveness of resistive force theory in granular locomotion. *Physics of Fluids*, 26(10):101308.

Zhao, B., Lauga, E., and Koens, L. (2019). Method of regularized stokeslets: Flow analysis and improvement of convergence. *Physical Review Fluids*, 4(8):084104.